figures from

Multidimensional Signal, Image, and Video Processing and Coding, 2nd Ed.

John W. Woods,

May 2011

Contents

Figures

This document contains all the figures and images from the book *Multidimensional Signal, Image, and Video, Processing and Coding*, 2nd Ed. But be warned that the figure numbers are unfortunately not the same. They do have the correct chapter and section numbers though. However within each chapter, the figures are numbered consecutively here.

John W. Woods, Rensselaer Polytechnic Institute

Chapter 1

Two-Dimensional Signals and Systems

1.1 TWO-DIMENSIONAL SIGNALS

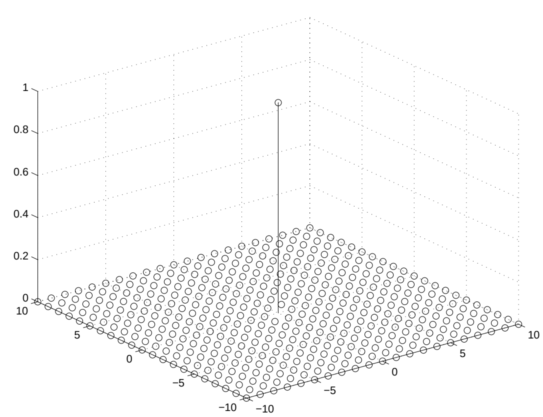

Figure 1.1–1. MATLAB plot of 2-D spatial impulse bi-sequence $\delta(n_1, n_2)$.

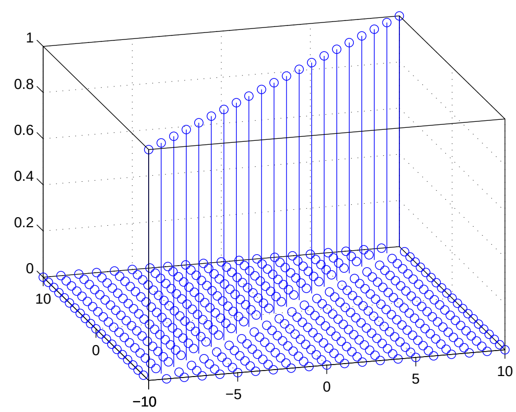

Figure 1.1–2. a section of the unit impulse line $\delta(n_1 - n_2)$ at 45°.

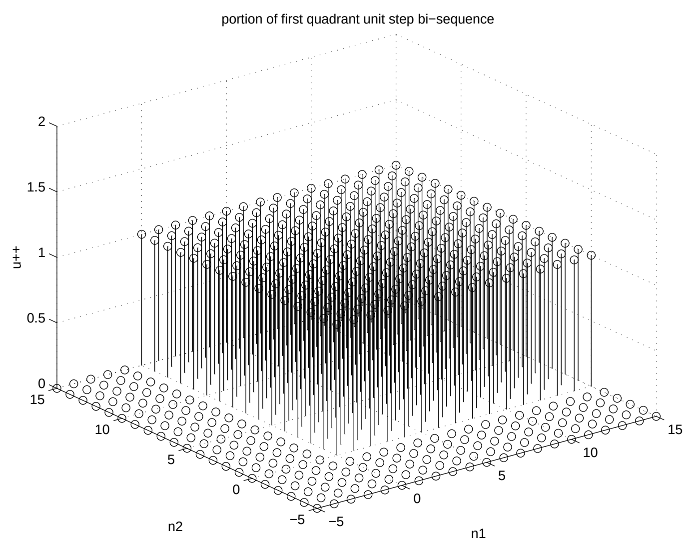

Figure 1.1–3. portion of unit step bi-sequence $u(n_1, n_2)$.

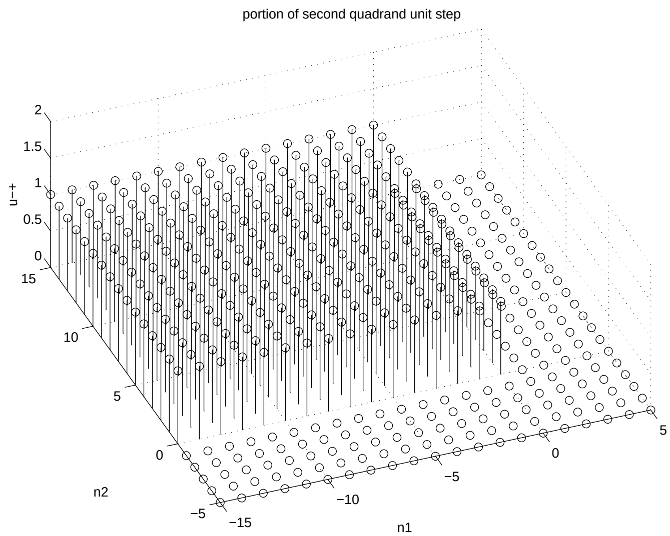

Figure 1.1–4. a portion of second quadrant unit step bi-sequence $u_{-+}(n_1, n_2)$.

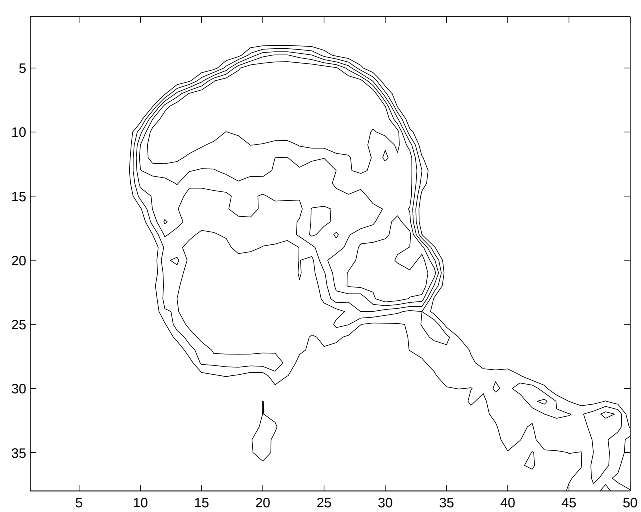

Figure 1.1–5. contour plot of *Eric*

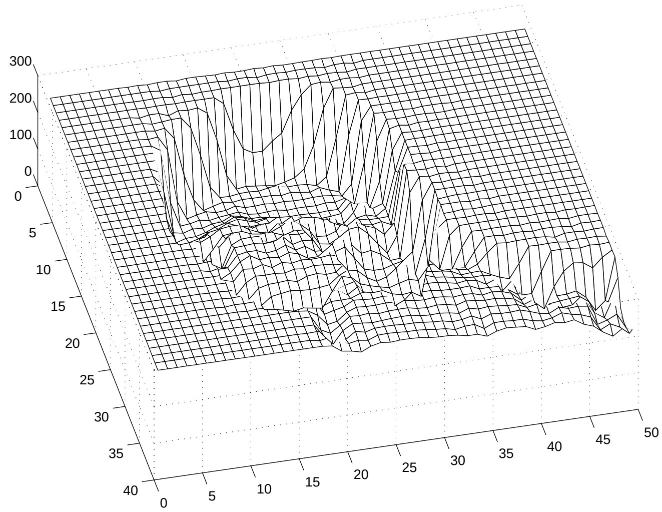

Figure 1.1–6. a mesh plot of *Eric*

Figure 1.1–7. an *image* or intensity plot of *Eric*

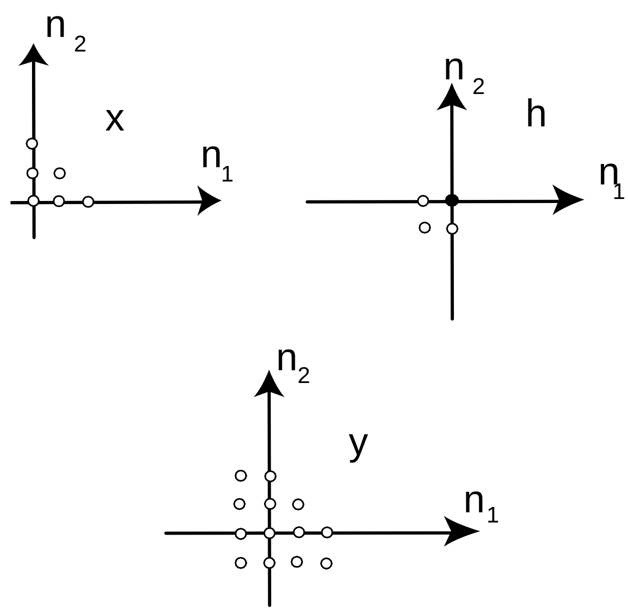

Figure 1.1–8. An example of 2-D or spatial convolution.

1.2 2-D DISCRETE-SPACE FOURIER TRANSFORM

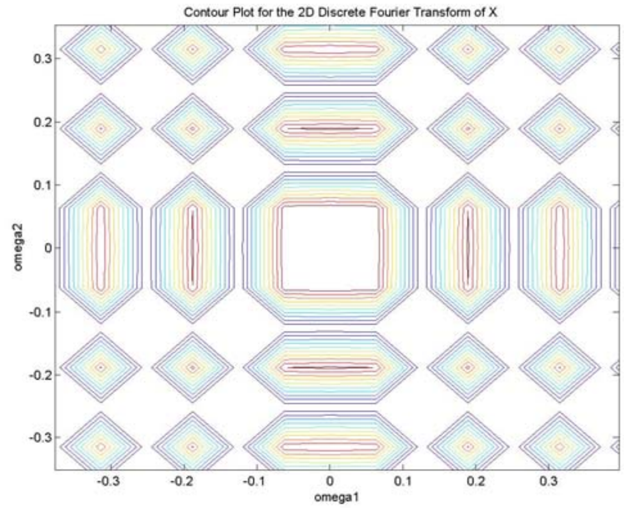

Figure 1.2–9. zoomed-in contour plot of log magnitude of 2-D rectangular sinc function with $N_1 = N_2 = 50$.

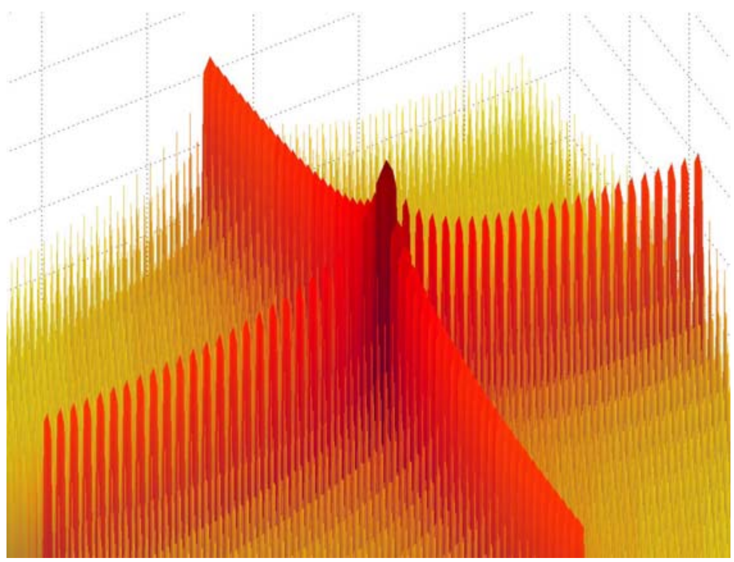

Figure 1.2–10. 3-D perspective plot of log magnitude of 2-D rectangular sinc function.

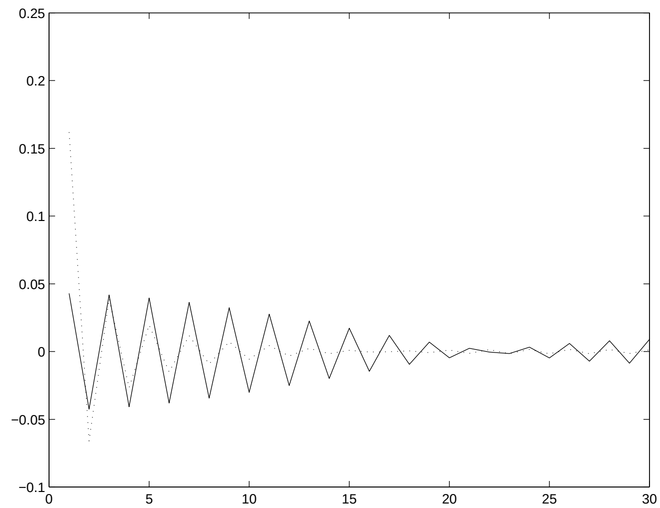

Figure 1.2–11. Two impulse responses of 2-D ideal lowpass filters. Solid curve is 'rectangular' and dotted curve is 'circular.'

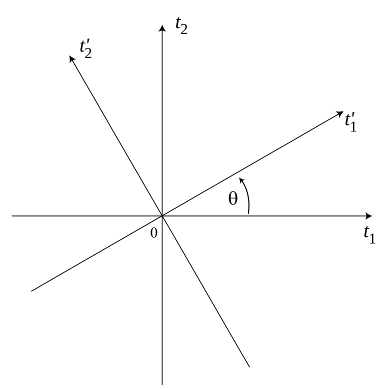

Figure 1.2–12. coordinate system $\mathbf{t}'$ is rotated from coordinate system $\mathbf{t}$ by rotation angle $+\theta$.

1.3 CONCLUSIONS

1.4 PROBLEMS

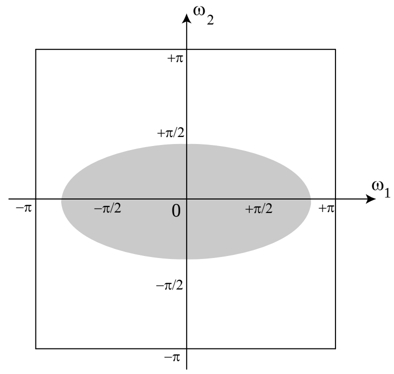

Figure 1.4–13. Ideal lowpass filter with elliptical support in the frequency domain, with cutoff frequencies ω_{c1} and ω_{c2}.

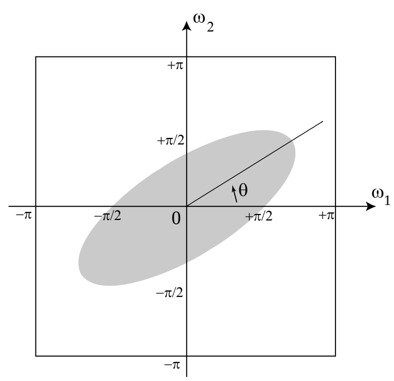

Figure 1.4–14. Ideal filter of Fig. 1 with passband rotated positively with angle θ as indicated.

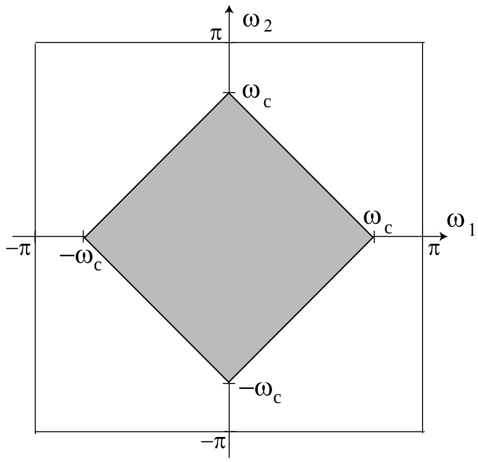
ω 2
π
ω c
ω c
ω 1
−π
−ω c
π
−ω c
−π

Chapter 2

Sampling in Two Dimensions

2.1 SAMPLING THEOREM - RECTANGULAR CASE

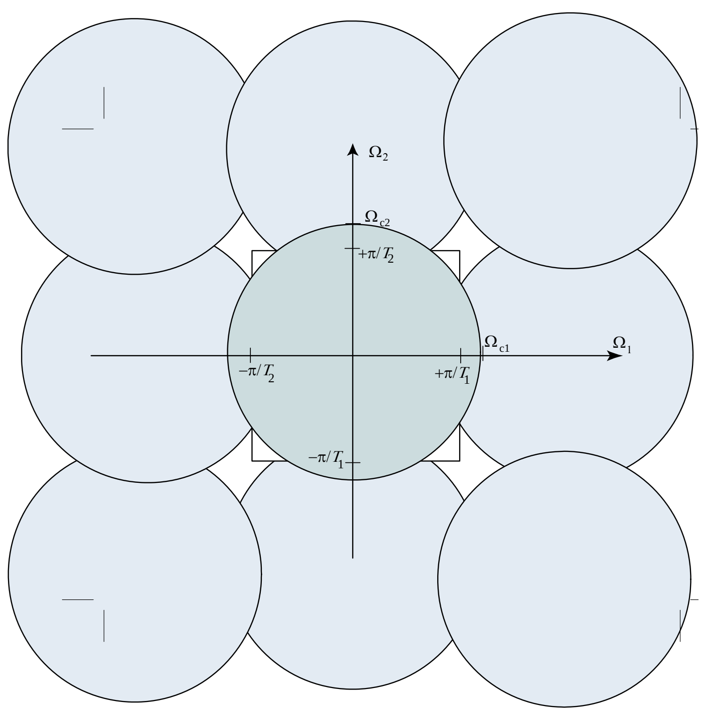

Figure 2.1–1. illustrating effect of nearest neighbor aliases for circular symmetric case.

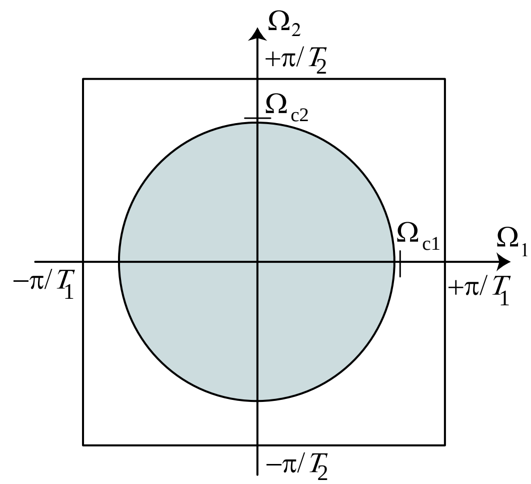

Figure 2.1–2. A continuous Fourier transform that will not alias when sampled at multiples of (T_1, T_2) and $\Omega_{c1} = \Omega_{c2}$ and $T_1 = T_2$.

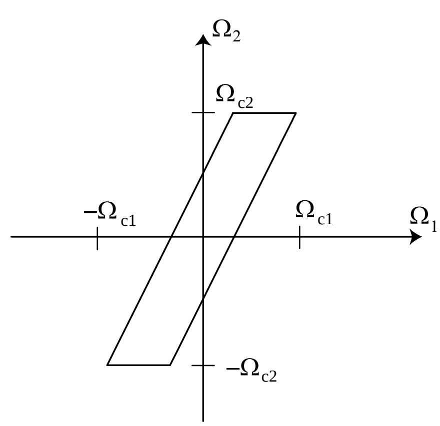

Figure 2.1–3. A continuous-space Fourier transform with 'diagonal' support.

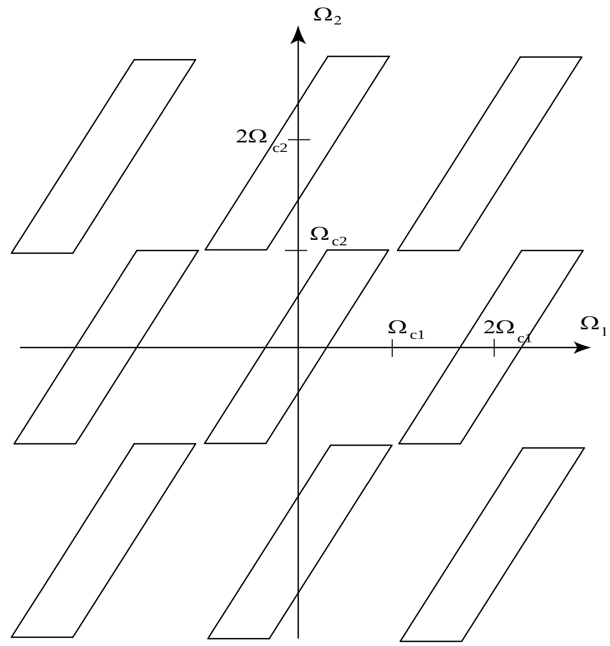

Figure 2.1–4. effect of rectangular sampling at rectangular Nyquist rate.

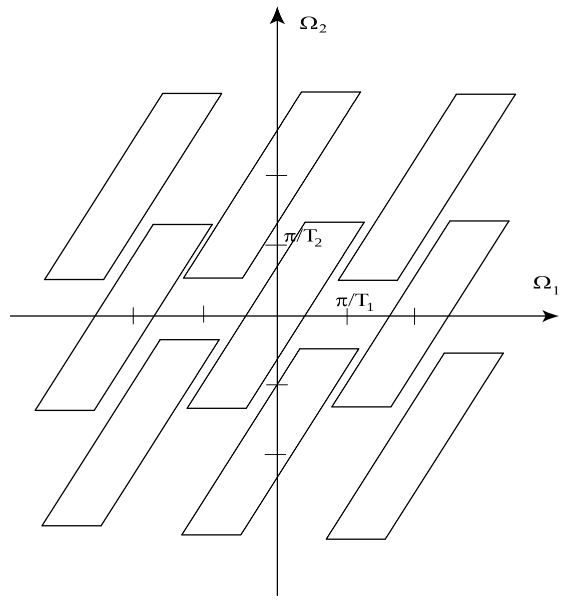

Figure 2.1–5. after lowering vertical sampling rate below the rectangular Nyquist rate

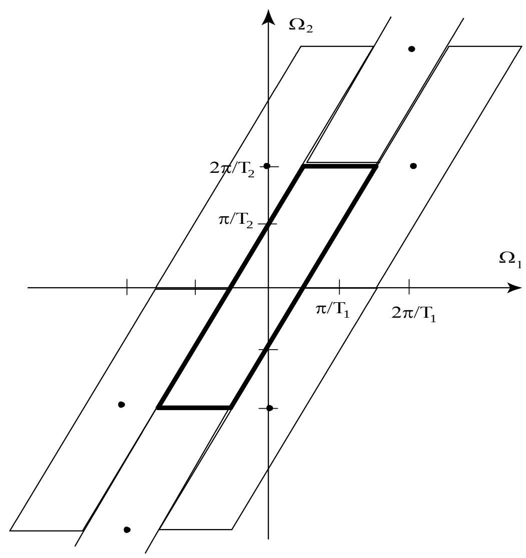

Figure 2.1–6. A basic cell, indicated by heavy lines, for diagonal analog Fourier transform support

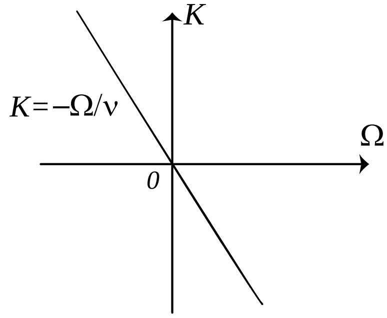

Figure 2.1–7. FT of ideal plane wave at velocity $v > 0$.

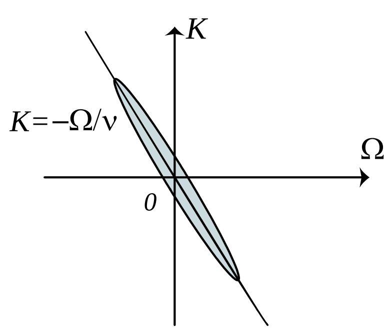

Figure 2.1–8. Fourier transform illustration of approximate plane wave at velocity v.

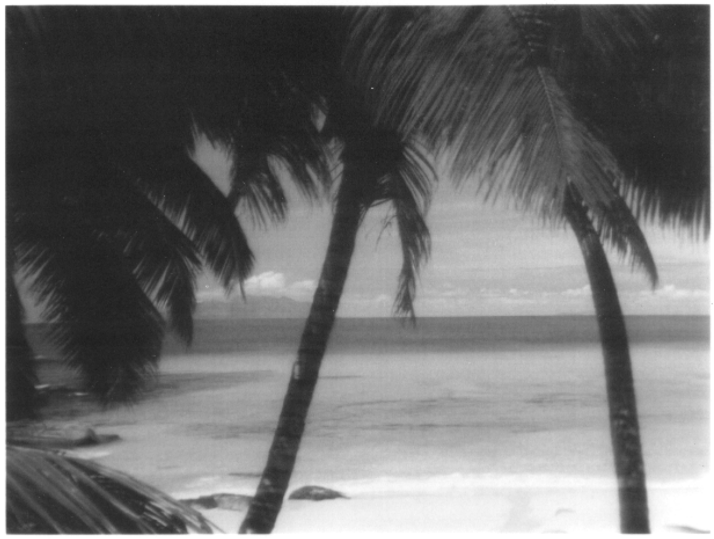

Figure 2.1–9. 2000×1000 pixel image with aliasing.

Figure 2.1–10. Zoomed-in section of aliased image.

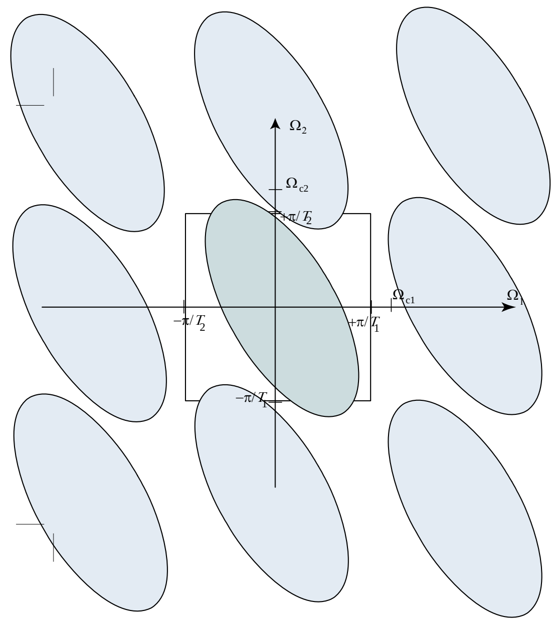

Figure 2.1–11. illustration of how alias (or 'imaging') error can arise in more directional case.

2.2 SAMPLING THEOREM - GENERAL REGULAR CASE

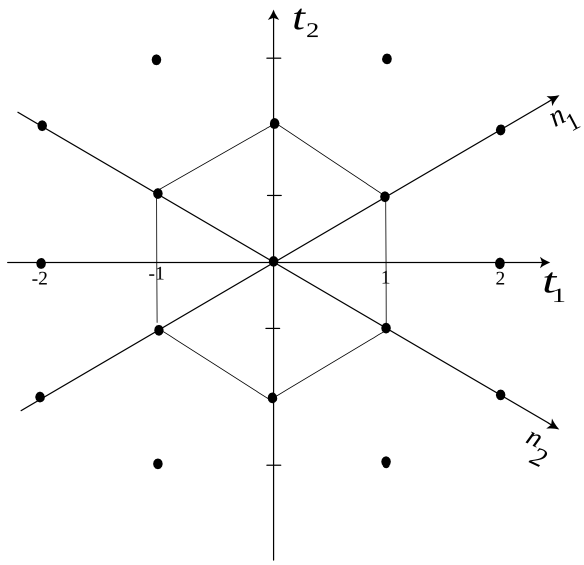

Figure 2.2–12. Hexagonal sampling grid in space.

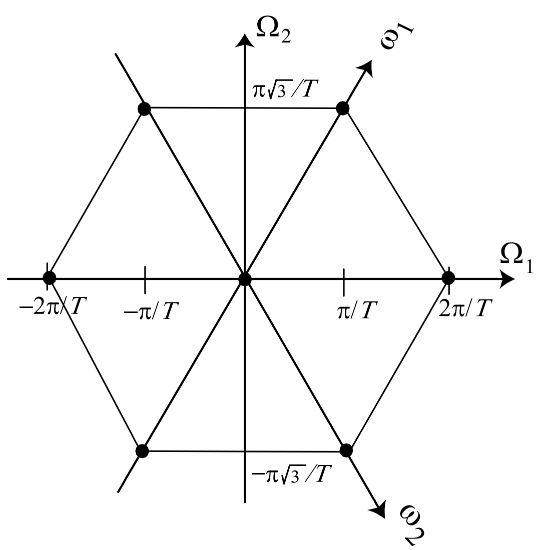

Figure 2.2–13. Hexagonal alias repeat grid in analog frequency domain.

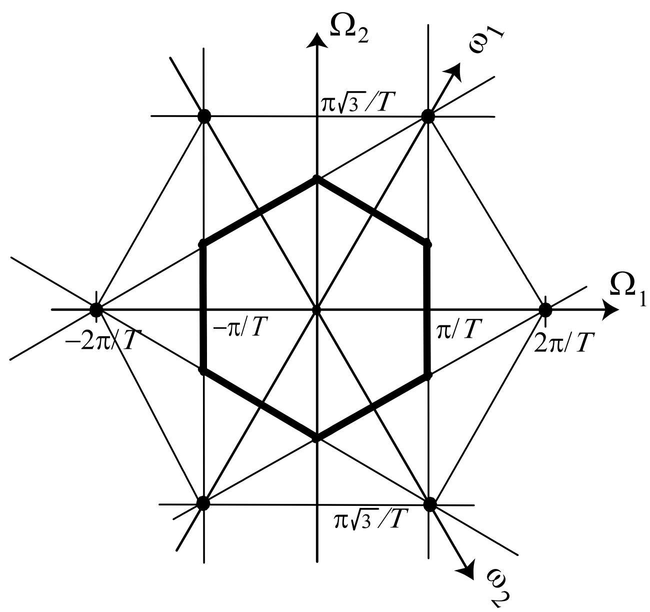

Figure 2.2–14. Hexagonal basic cell in analog frequency domain (heavy line).

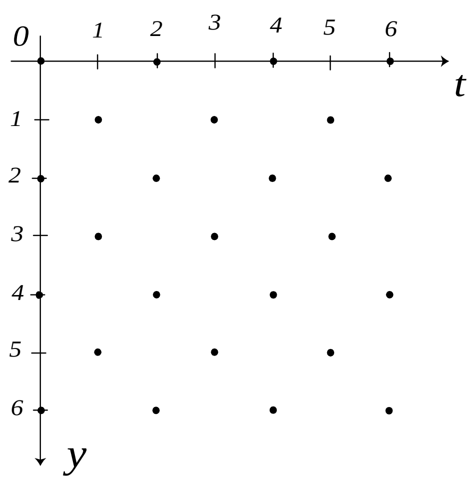

Figure 2.2–15. An illustration of interlaced sampling in 2-D vertical-temporal domain.

2.3 CHANGE OF SAMPLE RATE

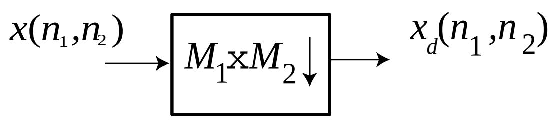

Figure 2.3–16. Downsample system element.

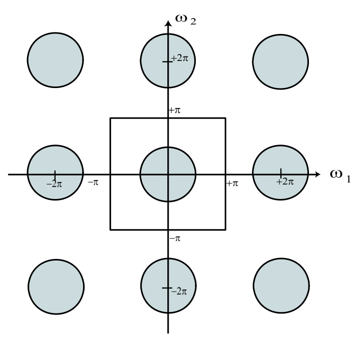

Figure 2.3–17. Illustration of lowpass X, plotted out beyond 2π in each variable.

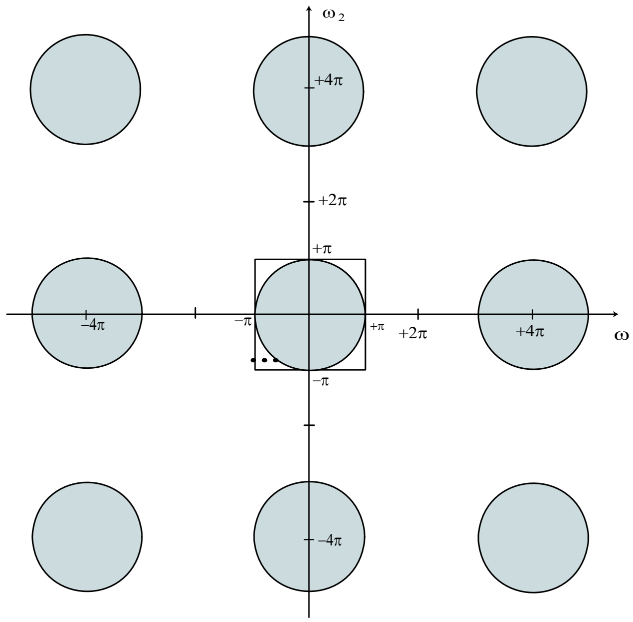

Figure 2.3–18.

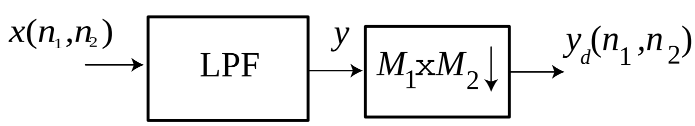

Figure 2.3–19. System diagam for ideal decimation which avoids aliasing error in the decimated signal.

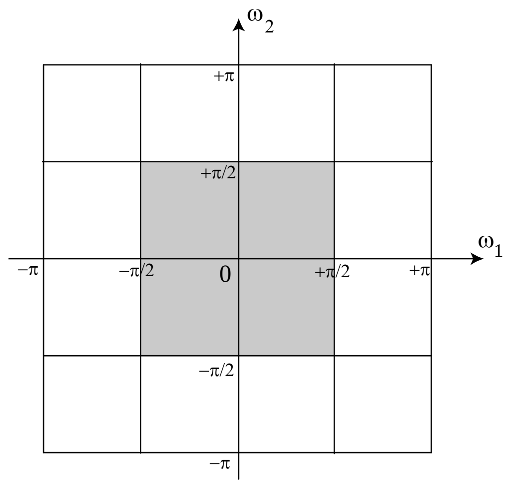

Figure 2.3–20. Grey area is the LL subband preserved under 2×2 ideal decimation.

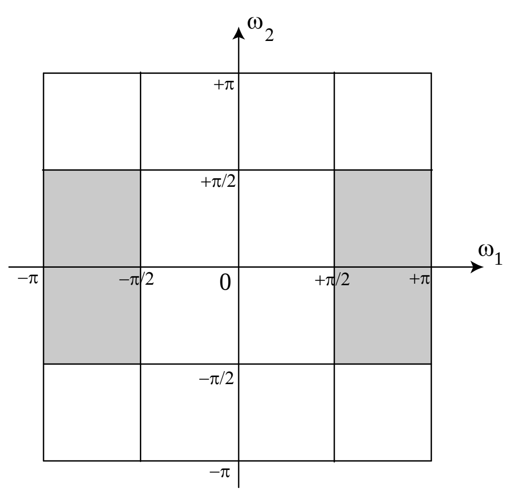

Figure 2.3–21. Frequency domain support of the HL subband.

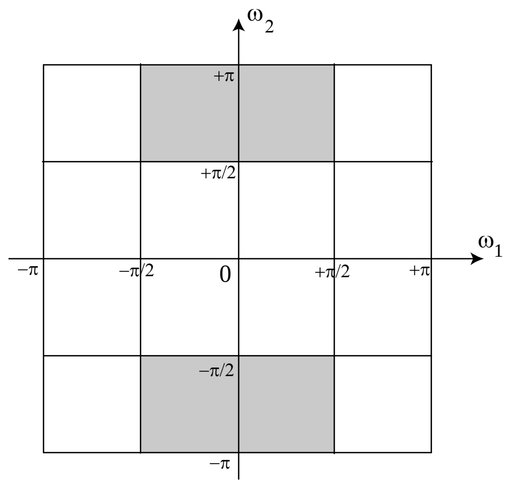

Figure 2.3–22. Frequency domain support of the LH subband.

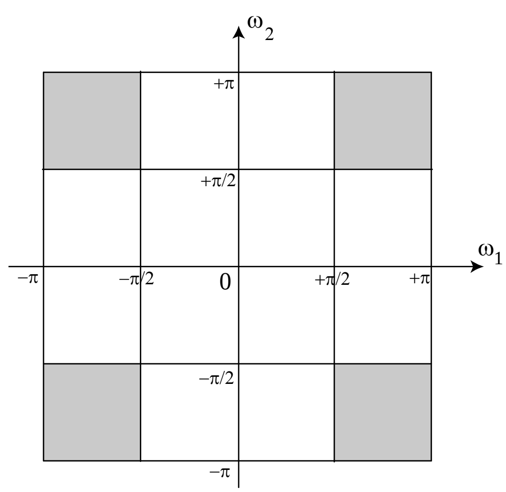

Figure 2.3–23. Frequency domain support of the HH subband.

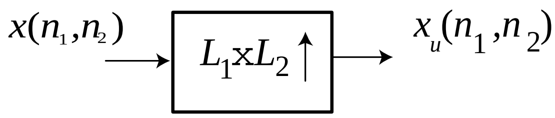

Figure 2.3–24. Up sample system element.

.

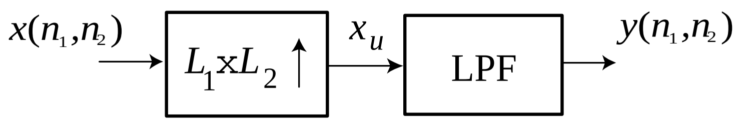

Figure 2.3–25. System diagram for ideal interpolation by integer factor $L_1 \times L_2$.

2.4 SAMPLE RATE CHANGE - GENERAL CASE

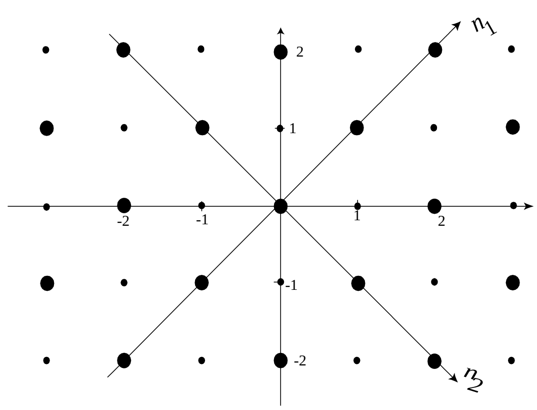

Figure 2.4–26. Illustration of portion of sub-lattice generated by diamond sub-sampling. Large filled-in circles are sub-lattice. Large and small filled-in circles are original lattice.

2.5 CONCLUSIONS

2.6 PROBLEMS

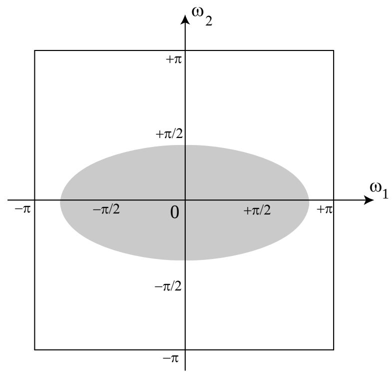

Figure 2.6–27. Ideal lowpass filter with elliptical support in the frequency domain, with cutoff frequencies ω_{c1} and ω_{c2}.

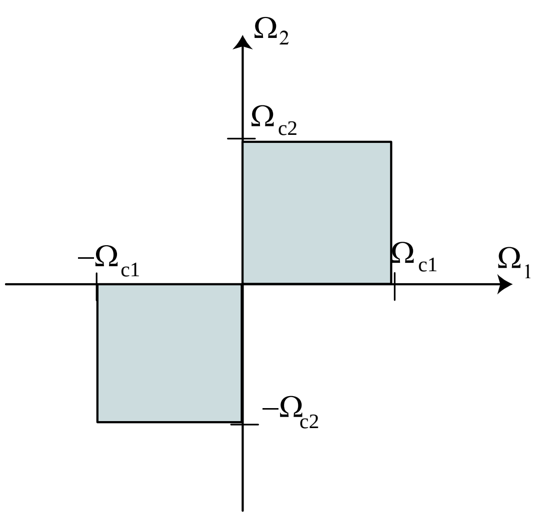

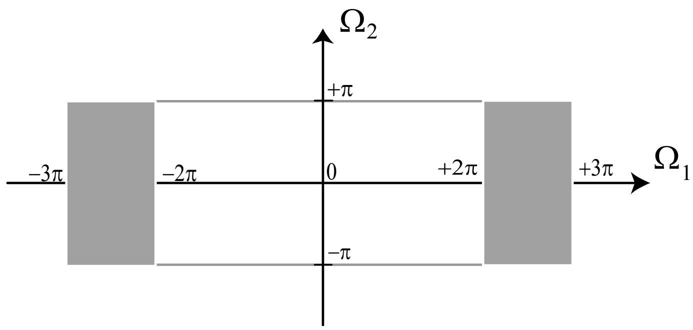

Figure 2.6–28. Bandpass Fourier Transform support of $X_c(\Omega_1, \Omega_2)$ indicated by dark gray areas.

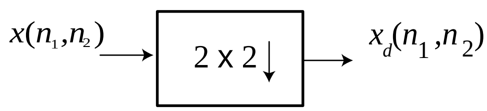

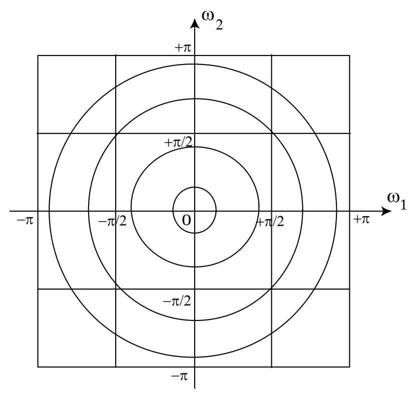

Figure 2.6–29. Contour plot sketch of a full band signal.

Chapter 3

Two-Dimensional Systems and Z-transforms

3.1 Linear Spatial or 2-D Systems

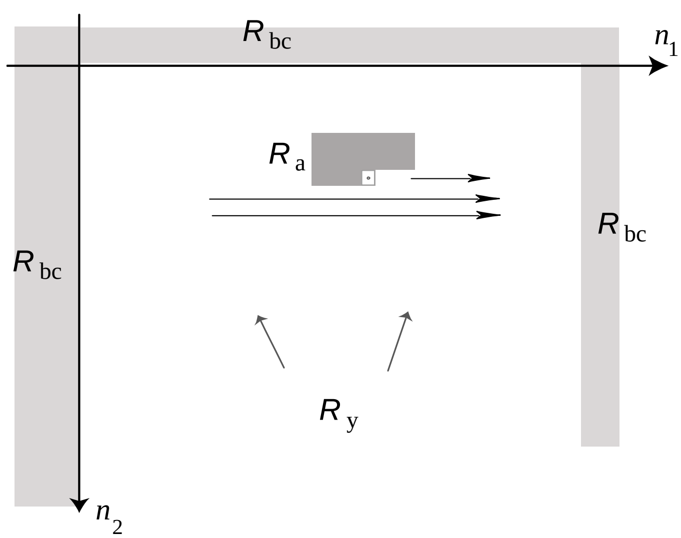

Figure 3.1–1. An example of a spatial difference equation solution region using an NSHP $\mathcal{R}_a$ coefficient support.

3.2 Z-TRANSFORMS

3.3 REGIONS OF CONVERGENCE

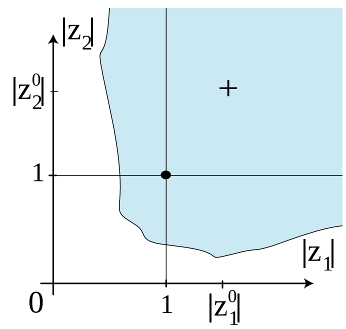

Figure 3.3–2. The 2-D complex magnitude plane. Here · denotes the unit bi-circle, and + denotes an arbitrary point at (z_1^0, z_2^0).

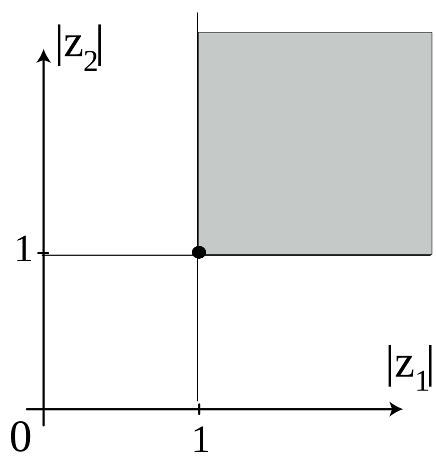

Figure 3.3–3. The gray area illustrates the ROC for the Z-transform of the first quadrant unit step function $u(n_1, n_2) = u_{++}(n_1, n_2)$.

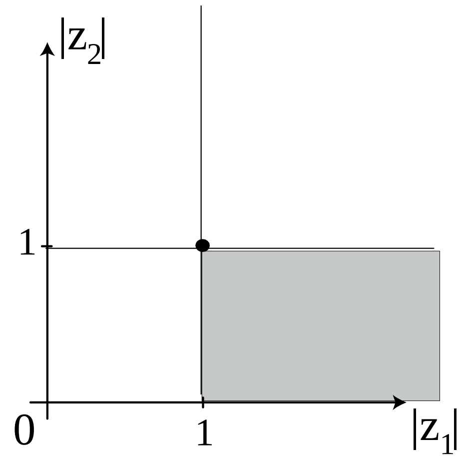

Figure 3.3–4. The ROC (grey area) for the 4th quadrant unit step function $u_{+-}(n_1, n_2)$.

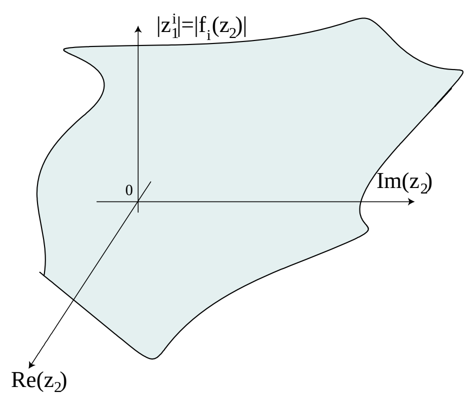

Figure 3.3–5. Sketch of pole magnitude $|z_1^i|$ as function of point in z_2 complex plane.

3.4 SOME Z-TRANSFORM PROPERTIES

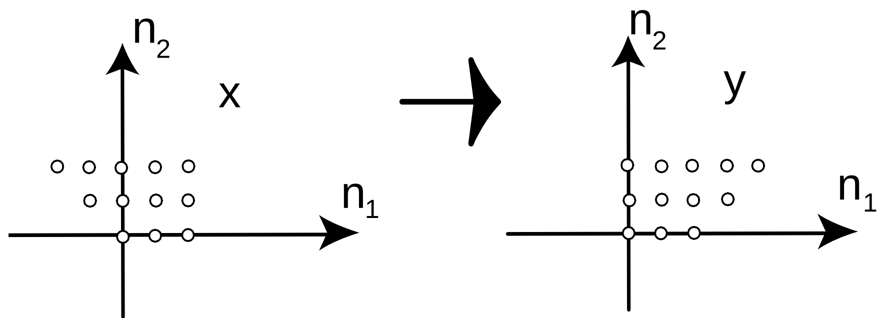

Figure 3.4–6. Example of linear mapping of variables

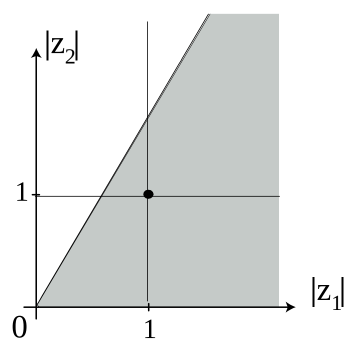

Figure 3.4–7. illustration of ROC (shaded area) of example Z transform

3.5 2-D FILTER STABILITY

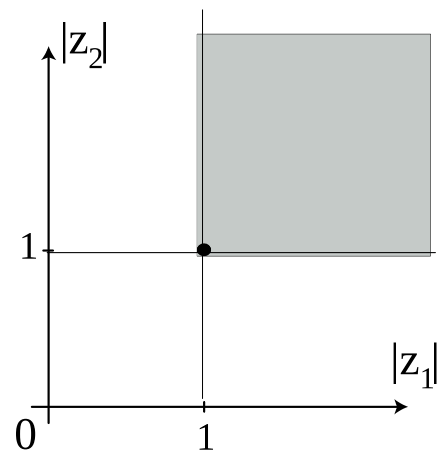

Figure 3.5–8. Region that must be included in the ROC of a stable 1st quadrant support filter.

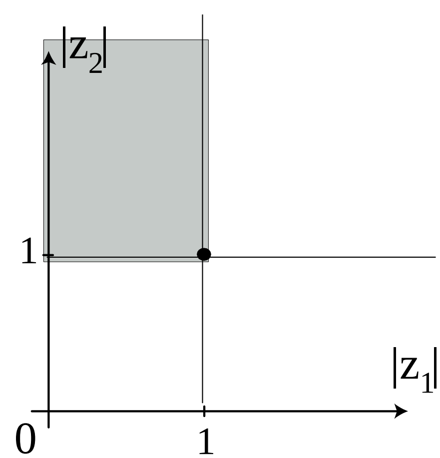

Figure 3.5–9. Illustration of region that a convergence region of a 2nd quadrant support stable filter must include.

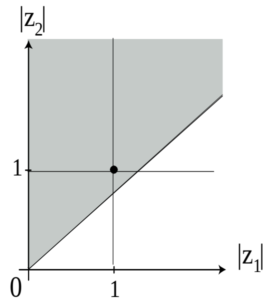

Figure 3.5–10. sketch of ROC (gray area) of example Z-transform

.

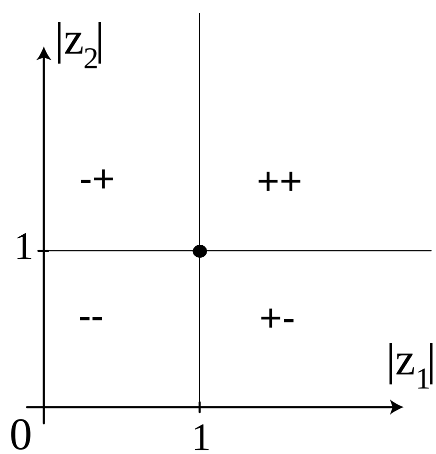

Figure 3.5–11. Illustration of necessary convergence regions for all four quarterplane support filters.

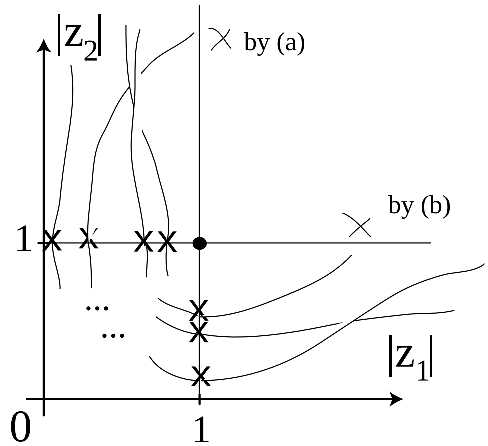

Figure 3.5–12. Figure used in proof of Theorem .

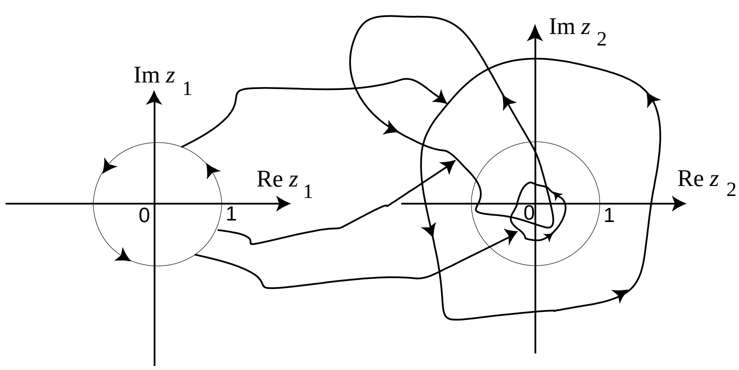

Figure 3.5–13. Illustration of root map of condition (a) of the previous Theorem.

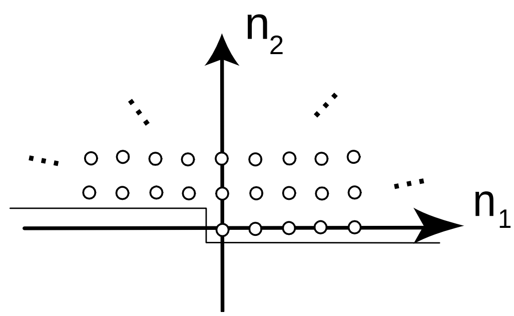

Figure 3.5–14. An illustration of NSHP coefficient array support.

3.6 CONCLUSIONS

3.7 PROBLEMS

Chapter 4

2-D Discrete-Space Transforms

4.1 DISCRETE FOURIER SERIES

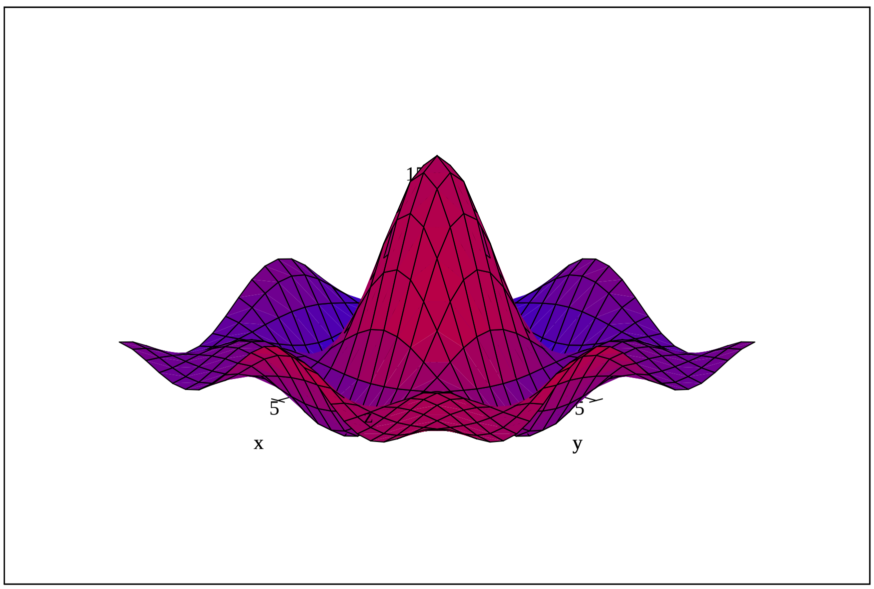

Figure 4.1–1. Plot of amplitude part of the DFS in Example 4.1-1.

4.2 DISCRETE FOURIER TRANSFORM

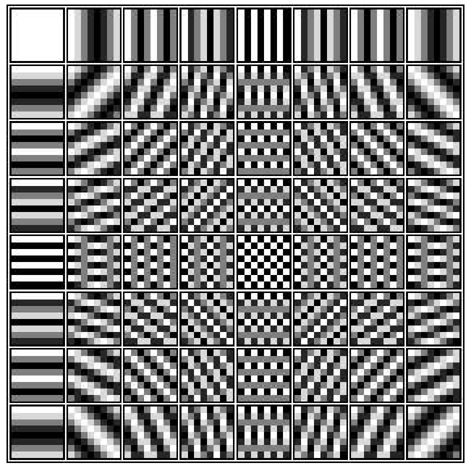

Figure 4.2–2. An image of the real part of 8×8 DFT basis functions.

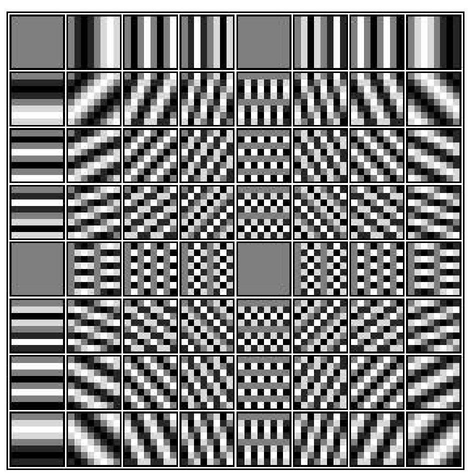

Figure 4.2–3. An image of the imaginary part of 8×8 DFT basis functions.

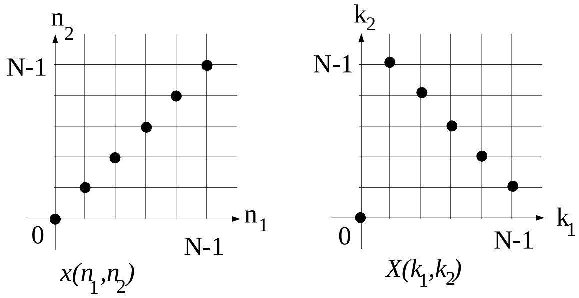

Figure 4.2–4. DFT of *1's on diagonal of square.*

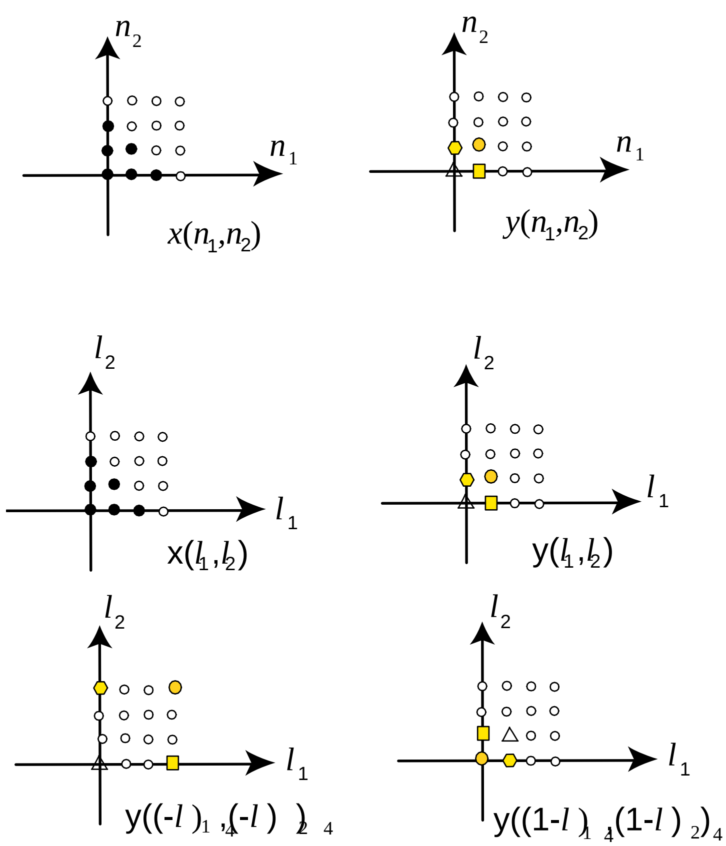

Figure 4.2–5. Example of 2-D circular convolution of small triangle support x and small square support y, both considered as $N_1 \times N_2 = 4 \times 4$ support.

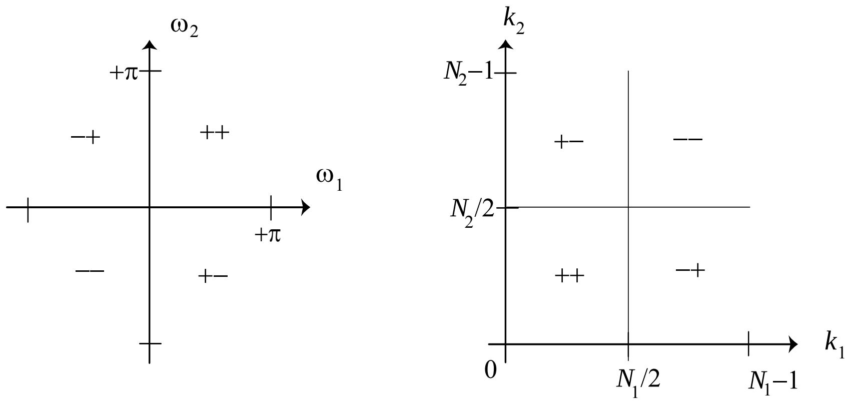

Figure 4.2–6. mapping of FT samples to DFT locations.

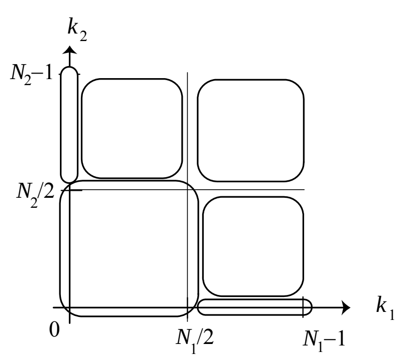

Figure 4.2–7. an illustration of the conjugate symmetry in DFT storage, for real valued image case.

4.3 2-D DISCRETE COSINE TRANSFORM

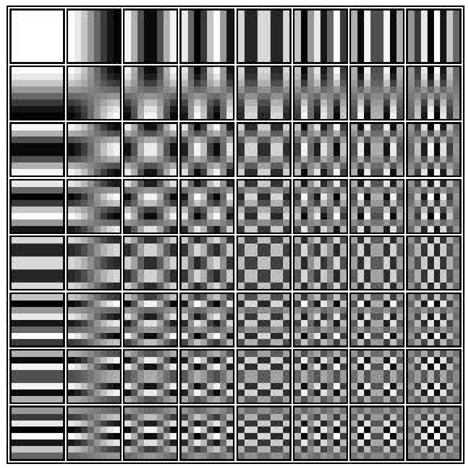

Figure 4.3–8. Image of the basis functions of the 8×8 DCT with $(0, 0)$ in the upper left corner and the k_2 axis pointing downwards.

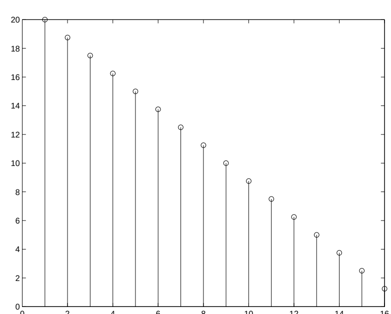

Figure 4.3–9. MATLAB plot of $x(n)$ over its support.

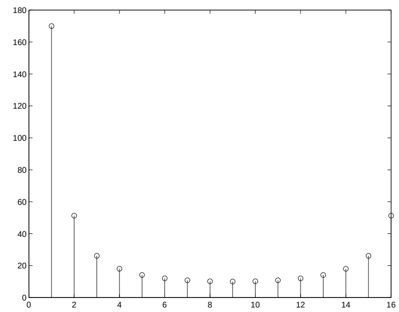

Figure 4.3–10. MATLAB plot of DFT magnitude $|X(k)|$

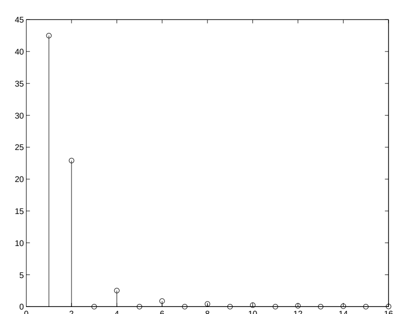

Figure 4.3–11. MATLAB plot of DCT $X_C(k)$.

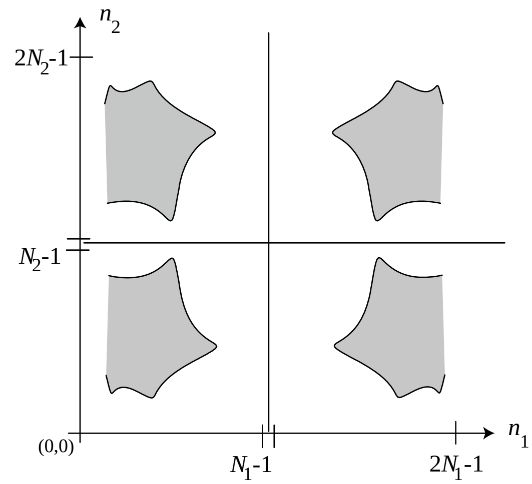

Figure 4.3–12. an illustration of 2-D symmetric extension used in the DCT

4.4 SUBBAND/WAVELET TRANSFORM (SWT)

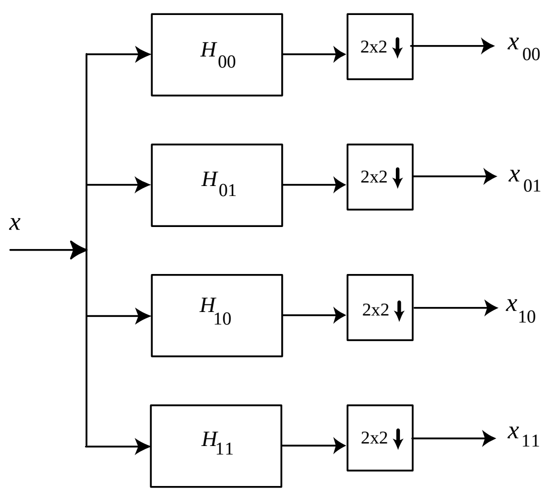

Figure 4.4–13. an illustration of 2×2 rectangular subband/wavelet transform.

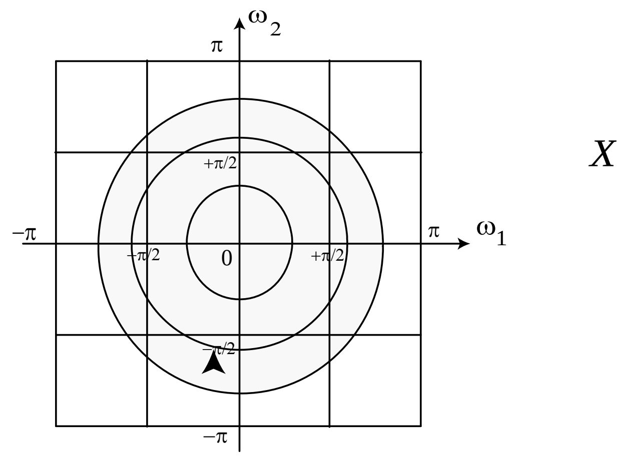

Figure 4.4–14. Fourier transform X of isotropic signal.

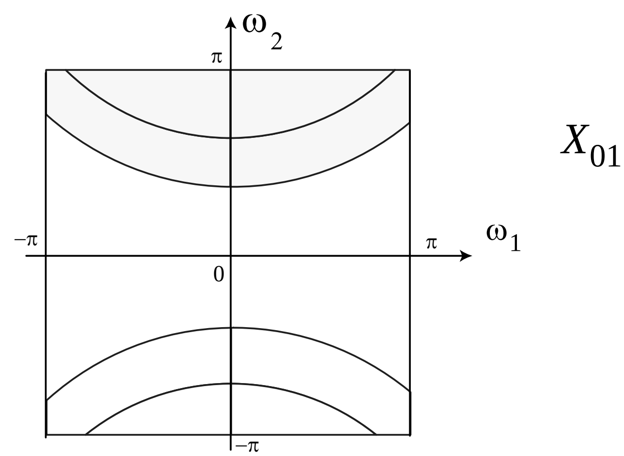

Figure 4.4–15. Fourier transform X_{01} of LH subband of isotropic signal.

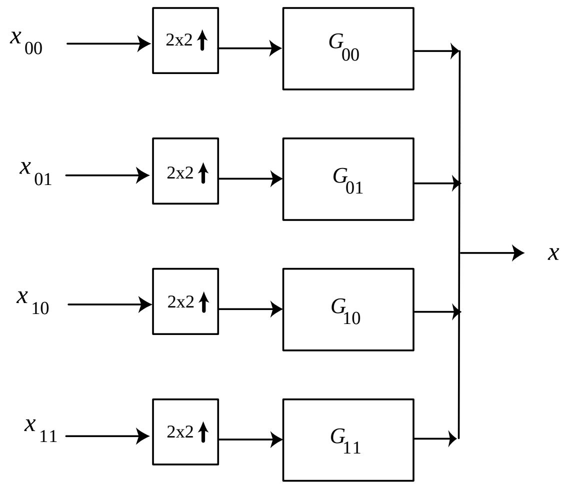

Figure 4.4–16. an illustration of 2 × 2 rectangular subband/wavelet inverse transform

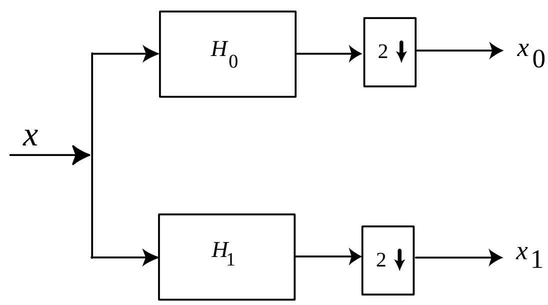

Figure 4.4–17. system diagram for two-channel 1-D SWT

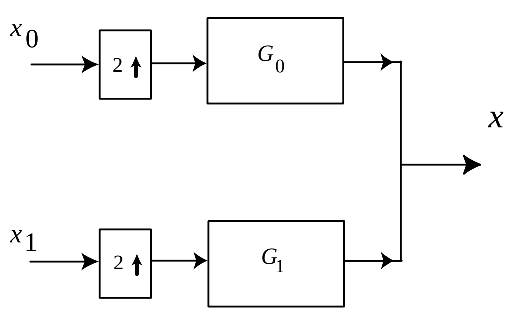

Figure 4.4–18. An illustration of the 1-D ISWT

4.5 FAST DFT ALGORITHM

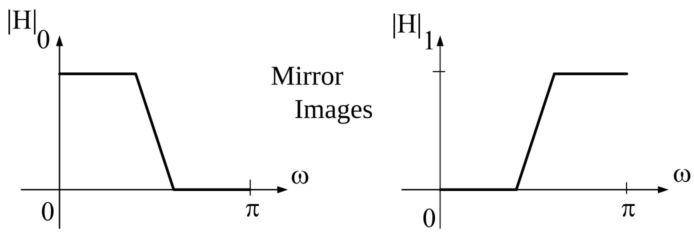

Figure 4.5–19. Illustration of magnitude responses of a quadrature magnitude filter (QMF) pair.

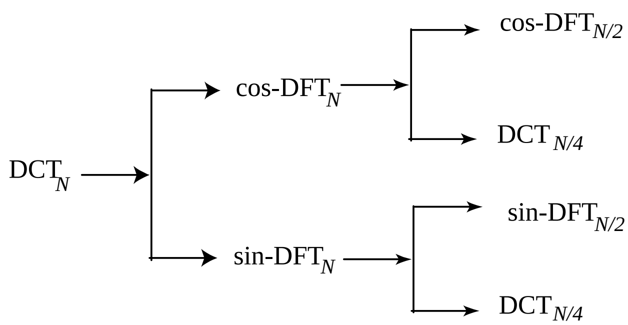

Figure 4.5–20. Tree diagram of fast DCT of [**??**].

4.6 SECTIONED CONVOLUTION METHODS

4.7 CONCLUSIONS

4.8 PROBLEMS

Chapter 5

Two-Dimensional Filter Design

5.1 FIR FILTER DESIGN

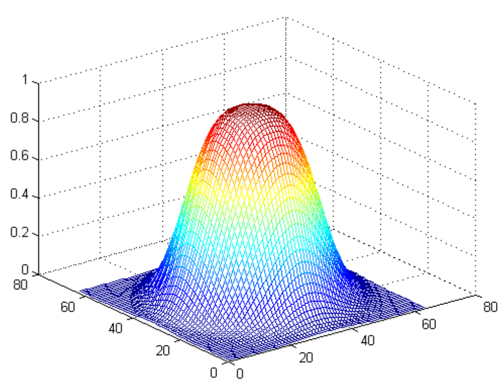

Figure 5.1–1. Magnitude response of Kaiser window FIR filter design with $\beta = 8$.

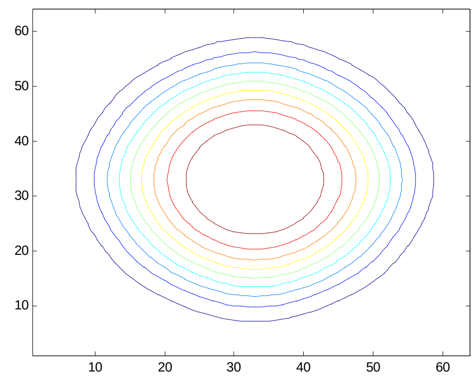

Figure 5.1–2. Contour plot of separable Kaiser window designed filter $\beta = 8$.

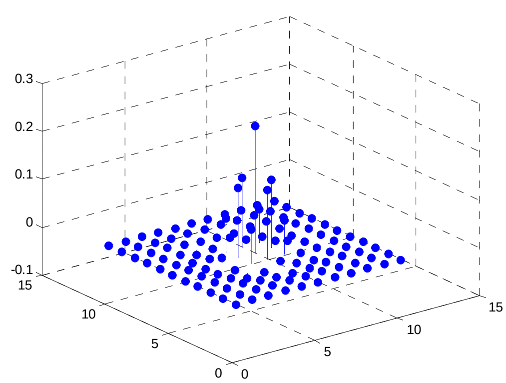

Figure 5.1–3. Plot of 11x11 impulse response.

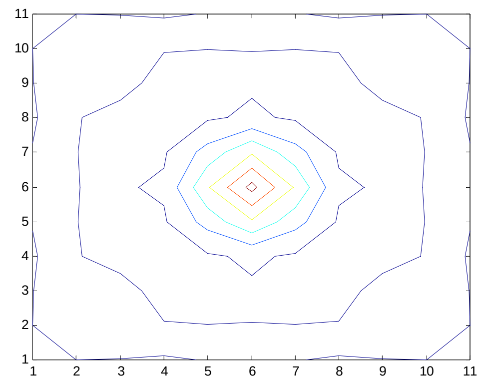

Figure 5.1–4. Contour plot of impulse response.

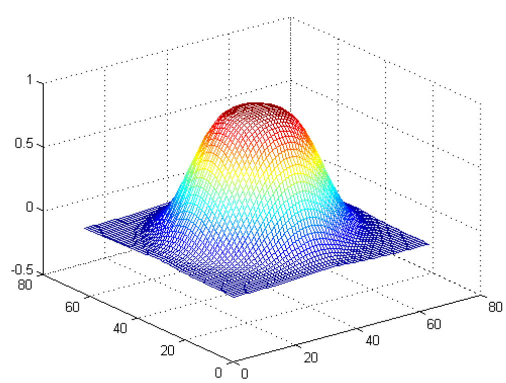

Figure 5.1–5. $\beta = 8$, but with circular Kaiser window.

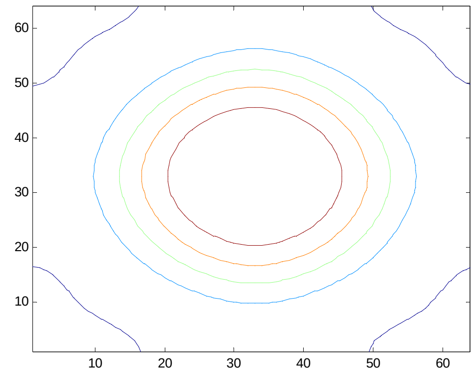

Figure 5.1–6. Contour plot of magnitude response.

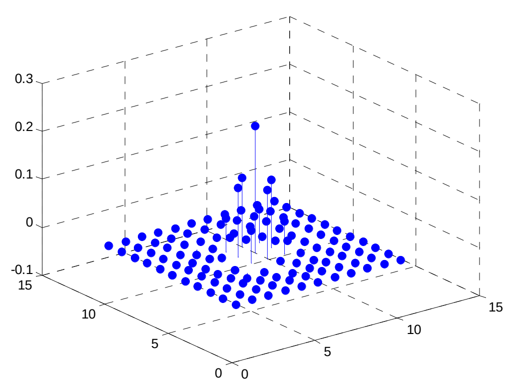

Figure 5.1–7. 11×11 impulse response of Kaiser circular window designed filter.

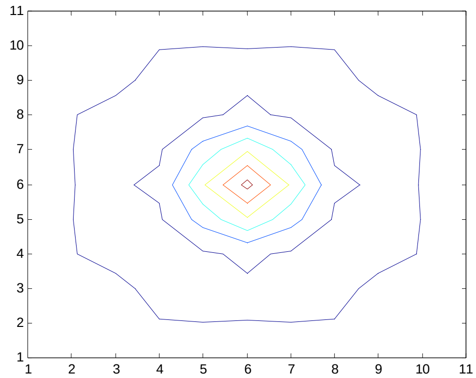

Figure 5.1–8. contour plot of impulse response

Figure 5.1–9. lowpass filtering of Eric image of Chapter 1

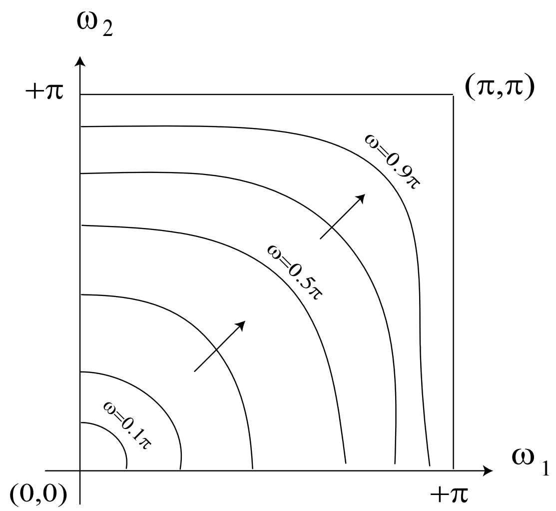

Figure 5.1–10. Illustration of 1×1 order McClellan transformation for near circular symmetric contours.

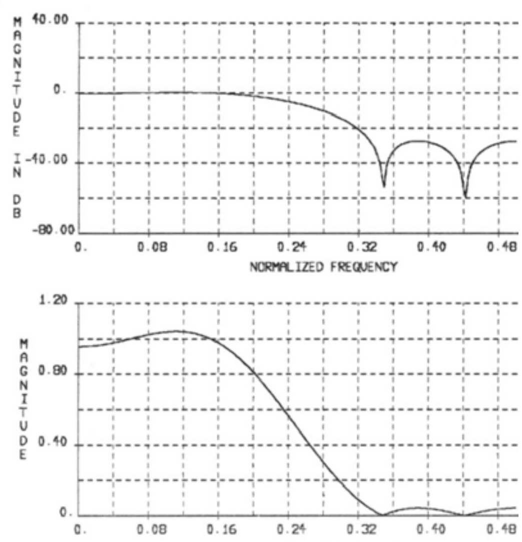

Figure 5.1–11. Magnitude response of 9 tap FIR type I filter of example.

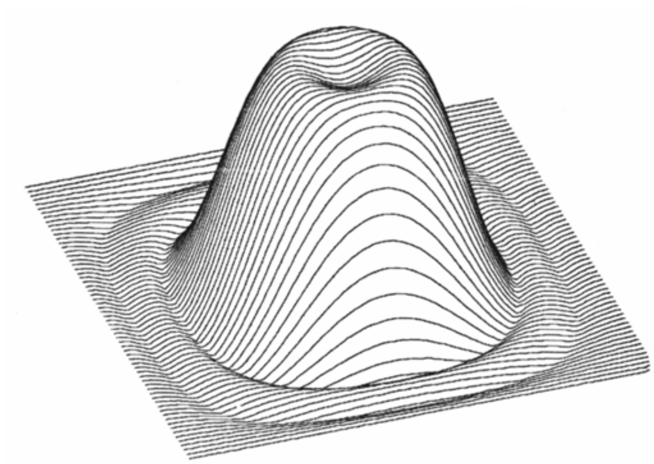

Figure 5.1–12. Plot of 9x9 FIR filter designed as a 2-D transform of a 9 tap lowpass filter.

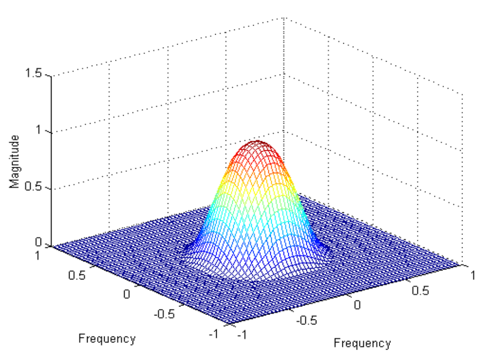

Figure 5.1–13. a lowpass filter for image filtering

Figure 5.1–14.

Figure 5.1–15. output of lowpass filter

Figure 5.1–16. corresponding differenc image (biased for display by +128)

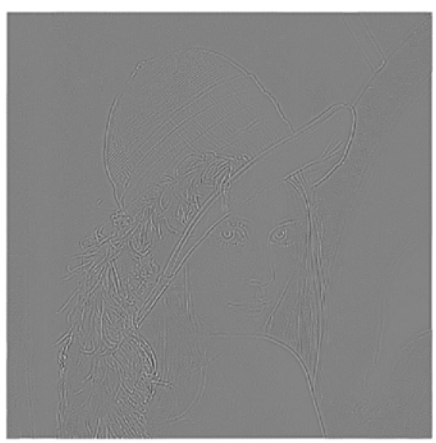

Figure 5.1–17. output of McClellan transformed near circular high pass filter

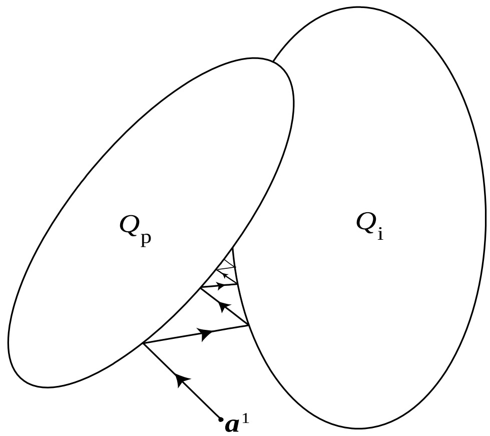

Figure 5.1–18. An illustration of the convergence based on orthogonal projection onto convex sets.

5.2 IIR FILTER DESIGN

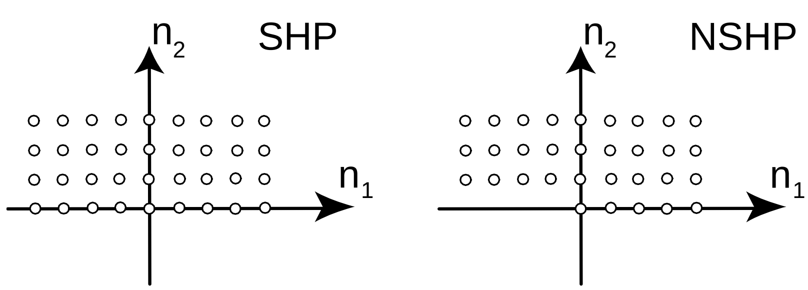

Figure 5.2–19. Illustration of FRF support options. Note that FRF impulse response support extends to the complete SHP or NSHP region.

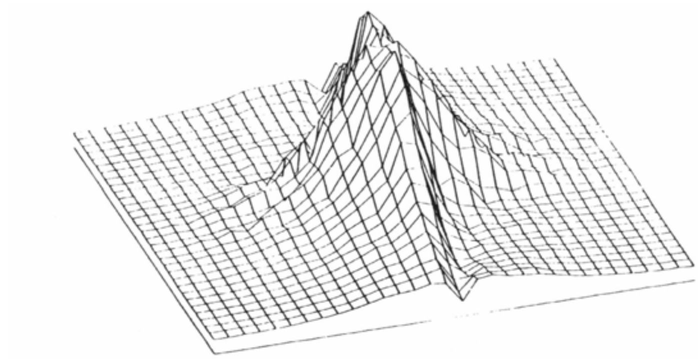

Figure 5.2–20. Ideal SHP Wiener filter magnitude

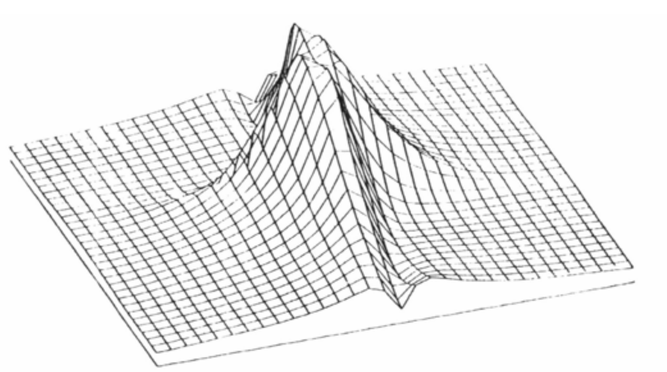

Figure 5.2–21. SHP FRF designed magnitude

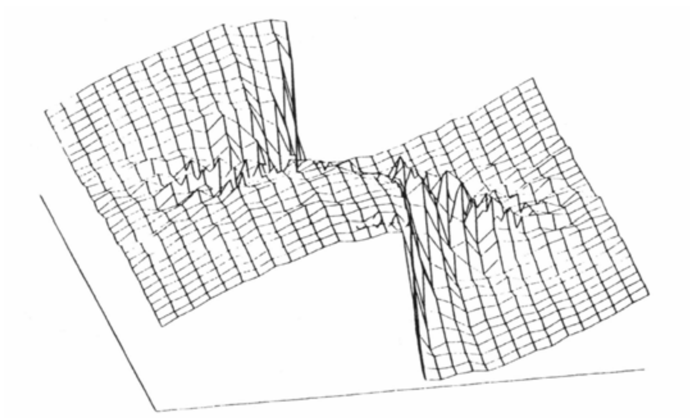

Figure 5.2–22. Ideal SHP Wiener phase response

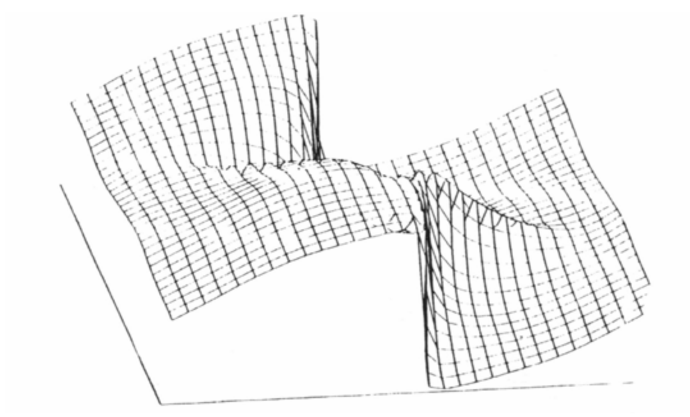

Figure 5.2–23. SHP FRF Wiener designed phase response

5.3 SUBBAND/WAVELET FILTER DESIGN

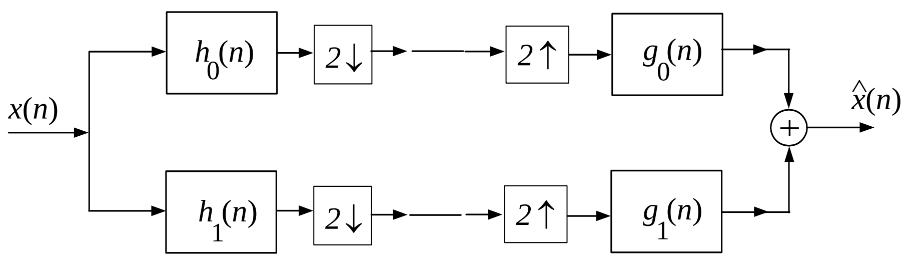

Figure 5.3–24. 1-D diagram of analysis/synthesis SWT/ISWT system

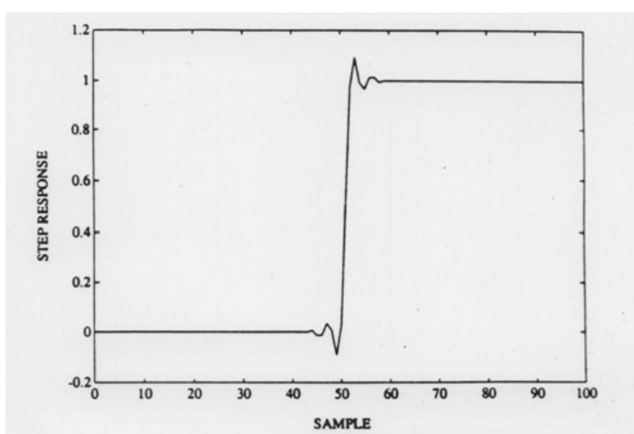

Figure 5.3–25. step response of Johnston 16C linear phase QMF filter.

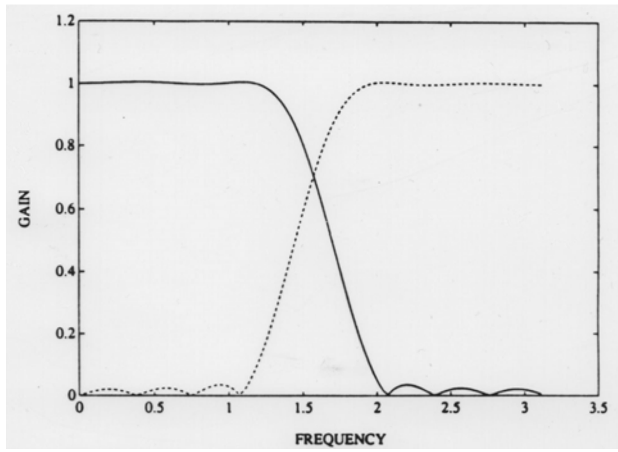

Figure 5.3–26. step response of Johnston 16C filter.

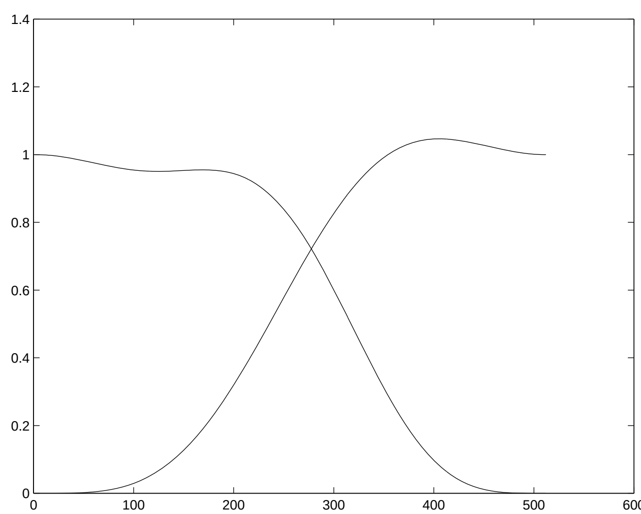

Figure 5.3–27. frequency response of CDF 9/7 analysis filters

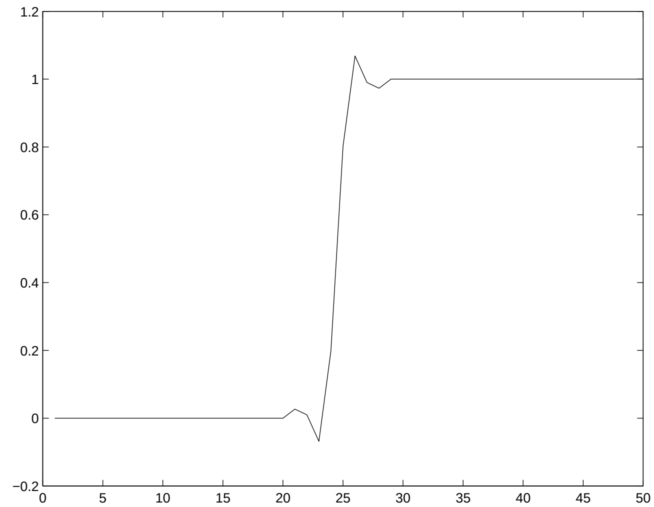

Figure 5.3–28. step response of CDF 9/7 analysis filter

Figure 5.3–29. an illustration of using two different anit-alias filters for downsampling.

5.4 CONCLUSIONS

5.5 PROBLEMS

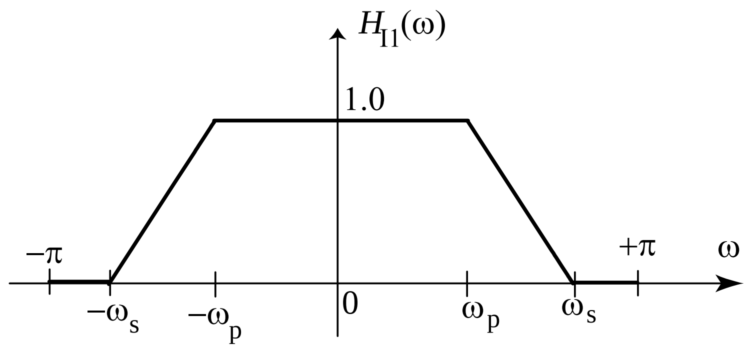

Figure 5.5–30. Alternative ideal filter response.

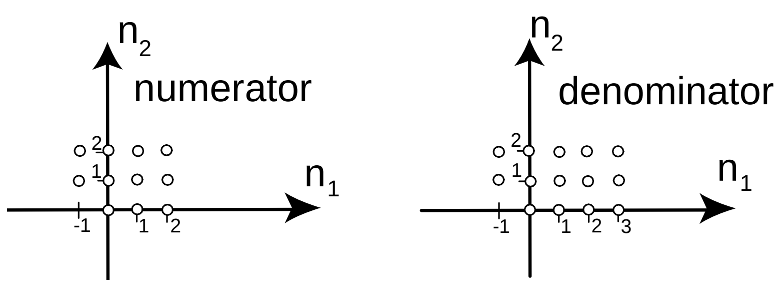

Figure 5.5–31. Numerator and denominator coefficient support region indicated by open circles.

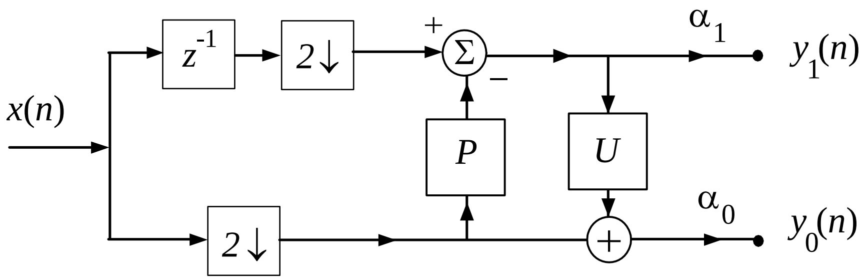

Figure 5.5–32. an illustration of the lifted SWT

Chapter 6

Image Perception and Sensing

6.1 LIGHT AND LUMINANCE

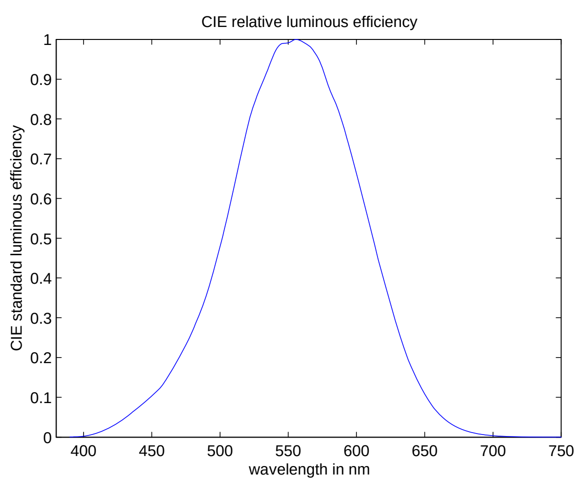

Figure 6.1–1. CIE 1929 relative luminous efficiency (standard observer)

6.2 STILL IMAGE VISUAL PROPERTIES

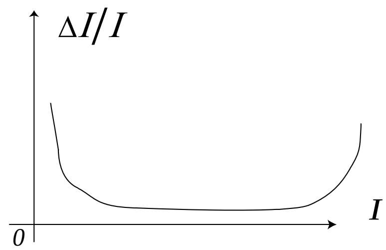

Figure 6.2–2. Average just resolvable intensity difference versus background intensity

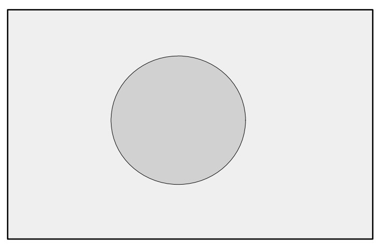

Figure 6.2–3. a stimula that can be used to Test Weber's law

Figure 6.2–4. equal increments at three different brightness values: 50, 100, 200, on range [0,255]

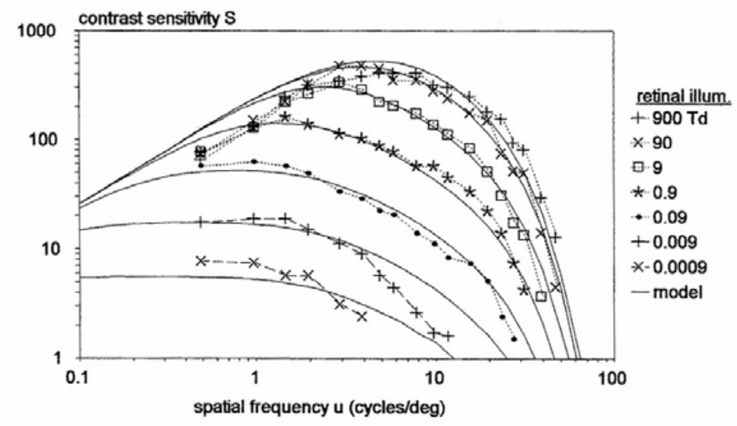

Figure 6.2–5. contrast sensitivity measurements of van Ness and Bouman (JOSA, 1967) [??]

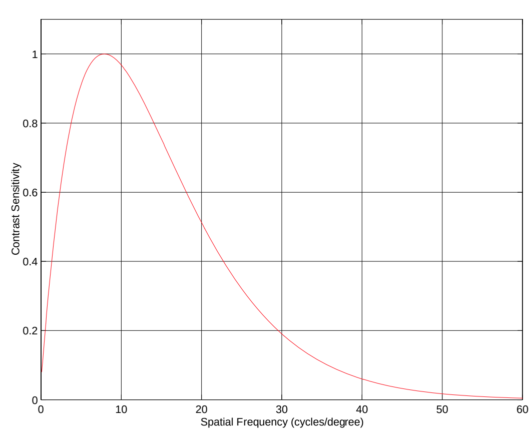

Figure 6.2–6. plot of Mannos and Sakrison function

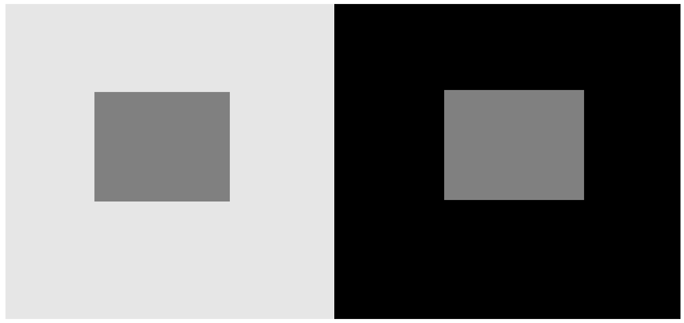

Figure 6.2–7. an illustration of local adaptation property of the human visual system

Figure 6.2–8. illustration of dependence of JND on local background brightness

6.3 TIME-VARIANT HUMAN VISUAL SYSTEM PROPERTIES

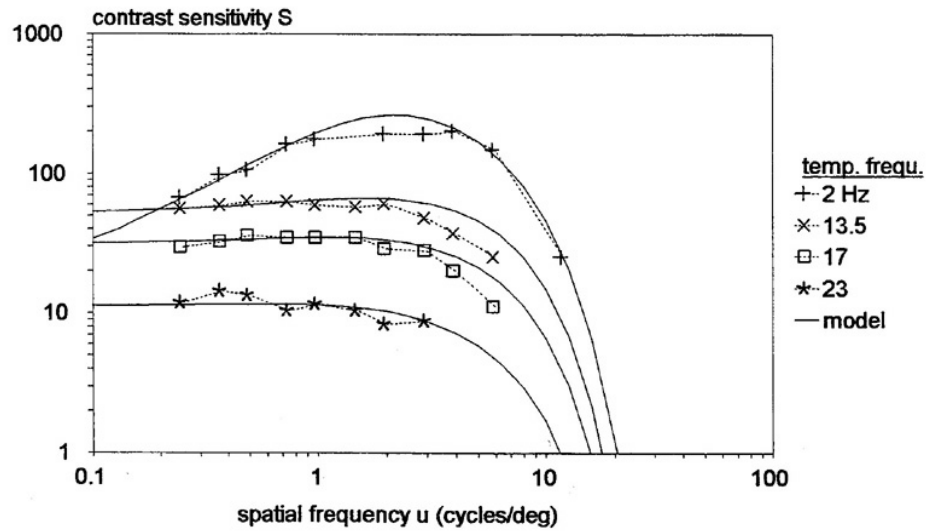

Figure 6.3–9. spatiotemporal CSF from Kelly (JOSA, 1979) [**??**]

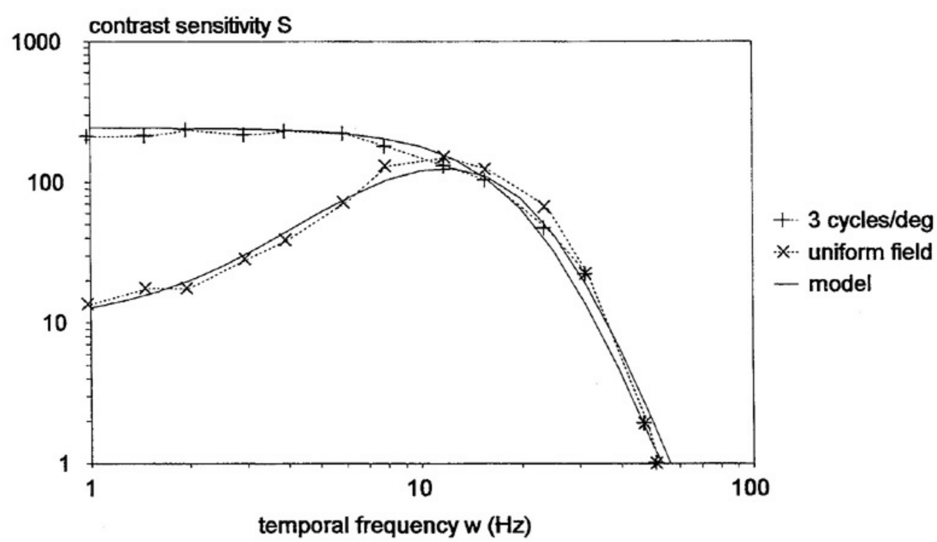

Figure 6.3–10. temporal CSF with spatial parameter from Kelly(JOSA, 1971) [**??**]

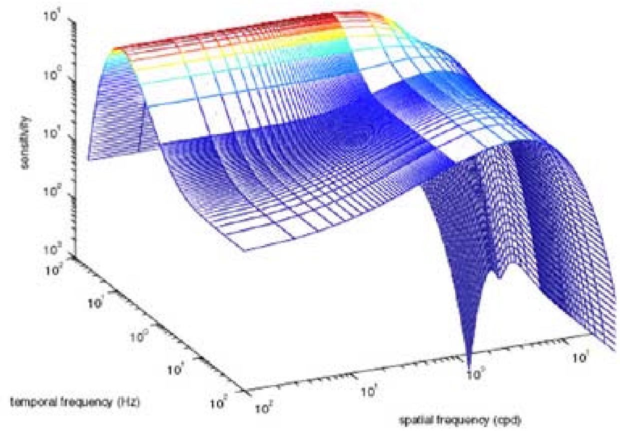

Figure 6.3–11. a perspective plot of a spatiotemporal CSF from Lambrecht and Kunt (*Image Communication* 1998) [**??**] (normalized to 10)

6.4 COLOR

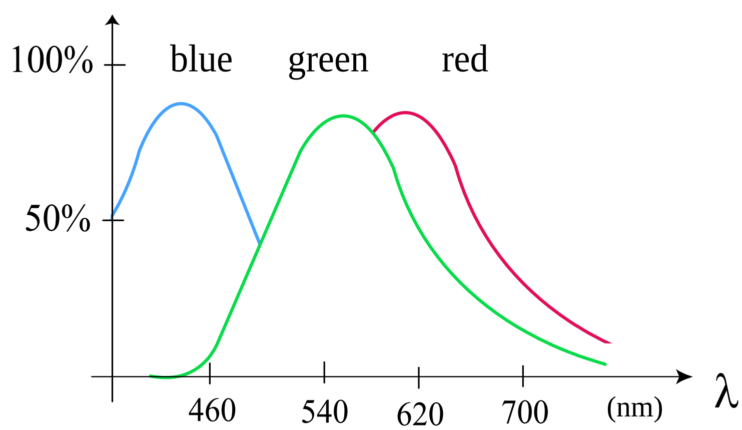

Figure 6.4–12. sketch of average sensitivity functions of three types of color receptors (cones) in human eye

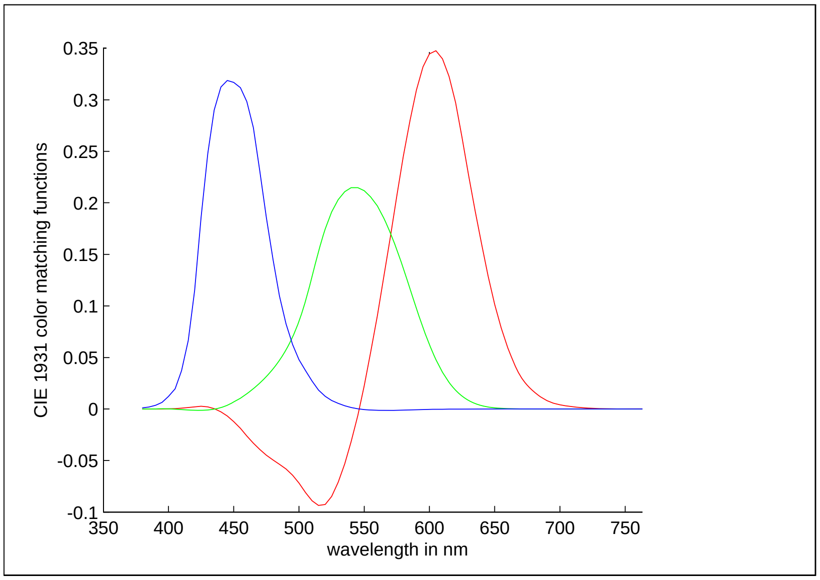

Figure 6.4–13. CIE *RGB* color matching functions (1931)

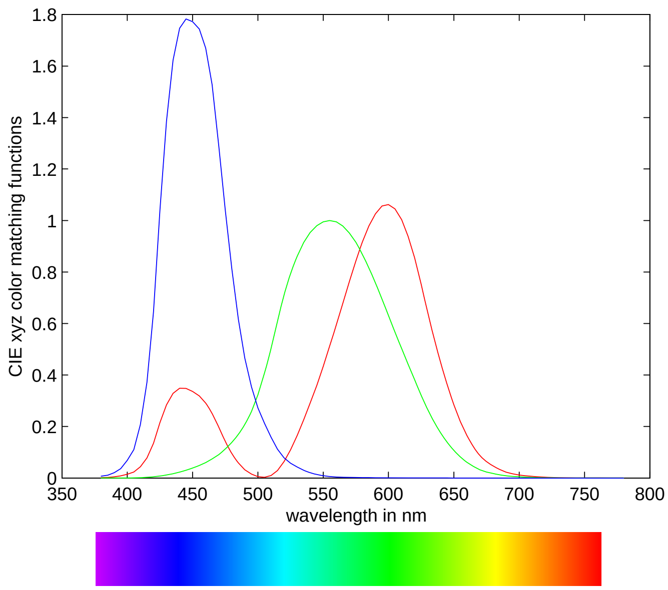

Figure 6.4–14. CIE 1931 X, Y, Z color matching functions (tristimulus values), also called $\bar{x}, \bar{y}, \bar{z}$ functions

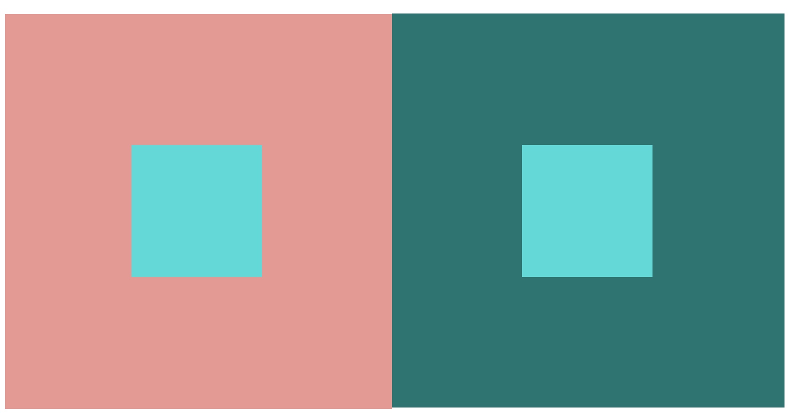

Figure 6.4–15. The small block has the same color in both sides of the figure.

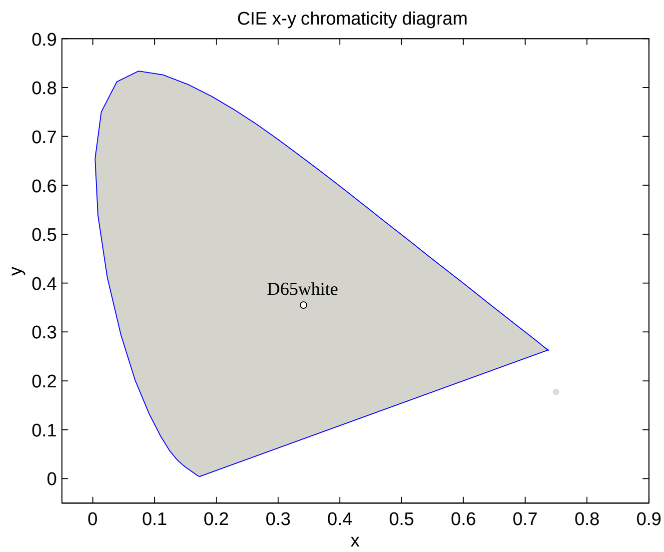

Figure 6.4–16. CIE 1931 chromaticity diagram of standard observer

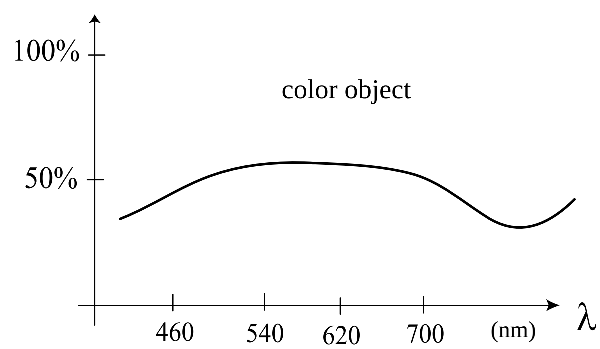

Figure 6.4–17. wavelength spectrum of a color object

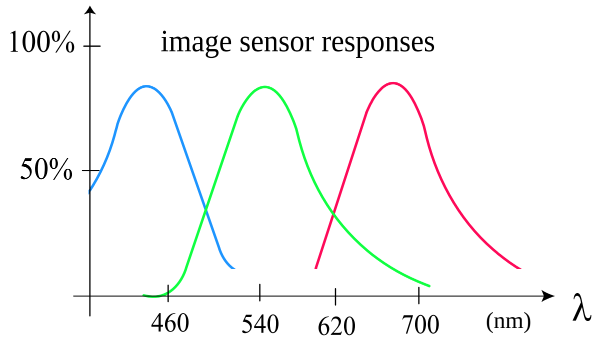

Figure 6.4–18. possible color sensor response functions

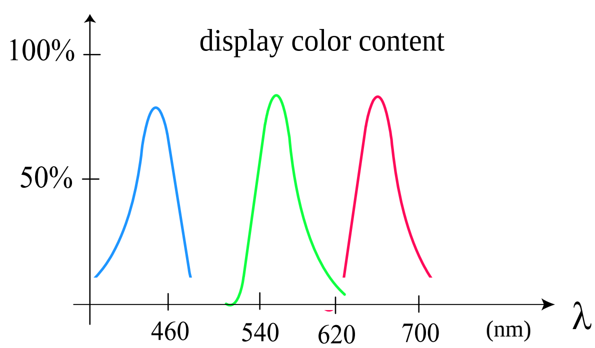

Figure 6.4–19. sketch of possible display color primaries

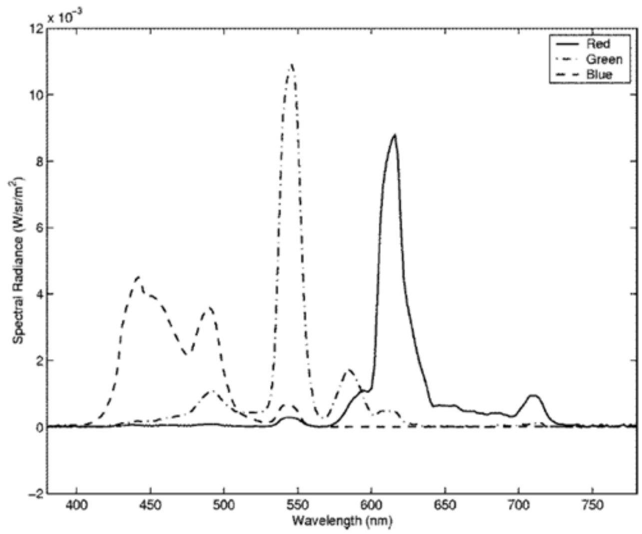

Figure 6.4–20. spectral radiance functions from the R, G, and B channels of an LCD panel (from [**??**] © 2002 IEEE)

6.5 COLOR SPACES

6.6 IMAGES SENSORS AND DISPLAYS

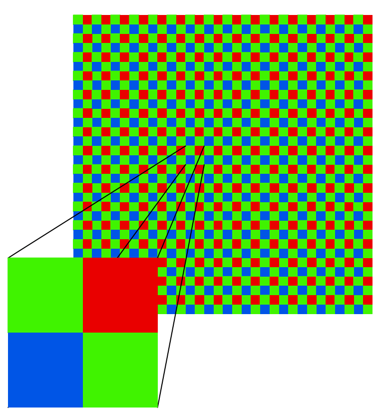

Figure 6.6–21. 2×2 pixel cell in Bayer CFA

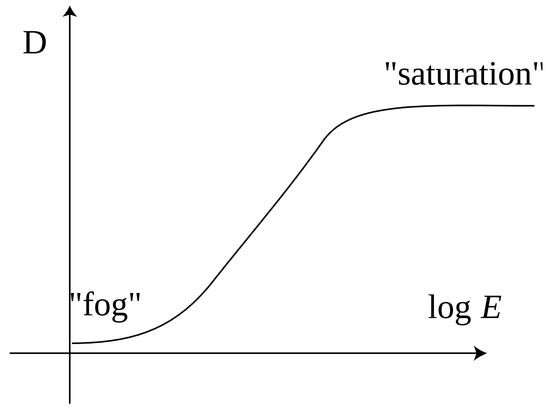

Figure 6.6–22. sketch of D-log E curve of film

6.7 CONCLUSIONS

6.8 PROBLEMS

Chapter 7

Image Enhancement and Analysis

7.1 SIMPLE IMAGE PROCESSING FILTERS

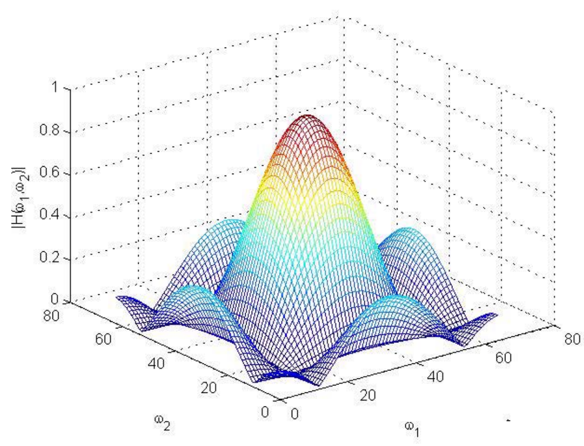

Figure 7.1–1. magnitude frequency response of box filter obtained with 64×64 DFT in MATLAB

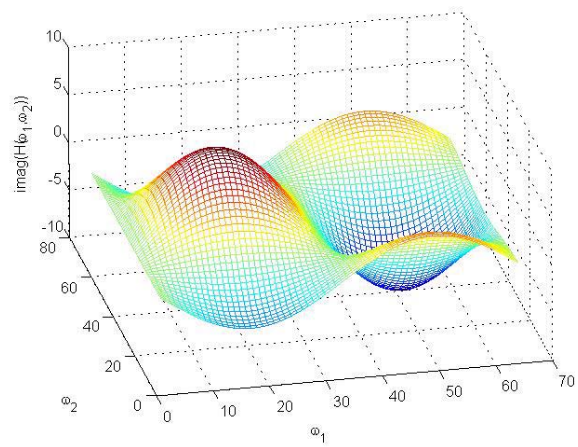

Figure 7.1–2. imaginary part of horizontal Sobel operator frequency response, obtained with 64×64 DFT

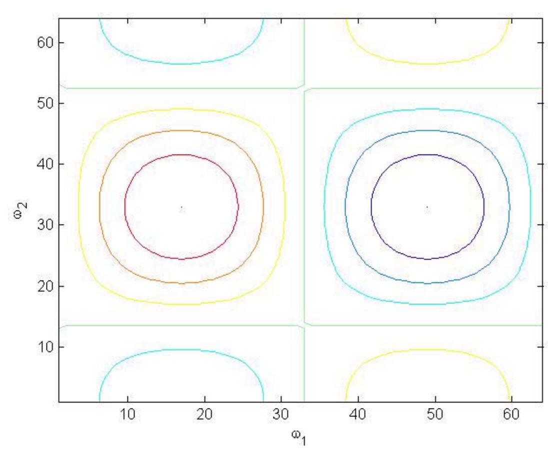

Figure 7.1–3. contour plot of imaginary part of horizontal Sobel operator, obtained with 64×64 DFT

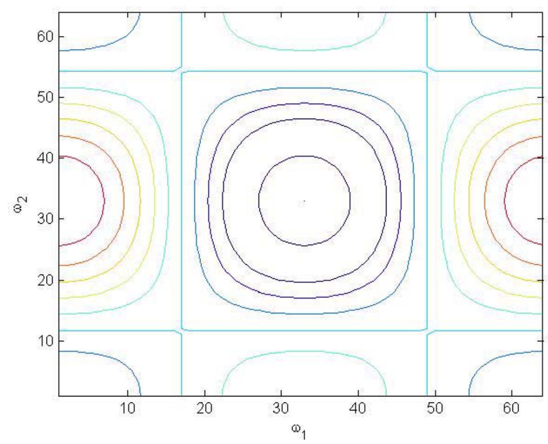

Figure 7.1–4. contour plot of magnitude frequency response of Laplace filter

7.2 IMAGE ENHANCEMENT

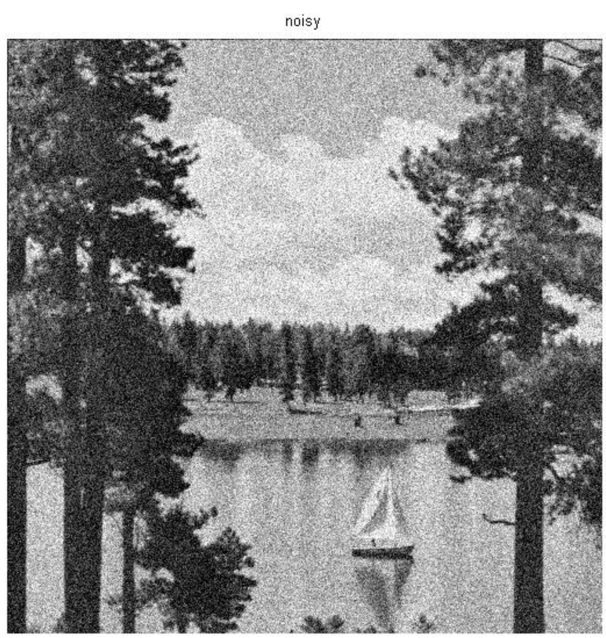

Figure 7.2–5. noisy image with noise variance 1024

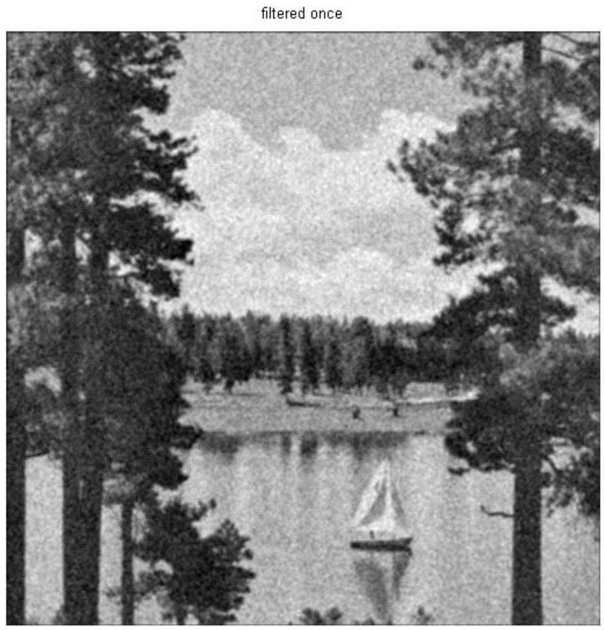

Figure 7.2–6. output after 3×3 box filtering

Figure 7.2–7. output after two passes of 3×3 box filter

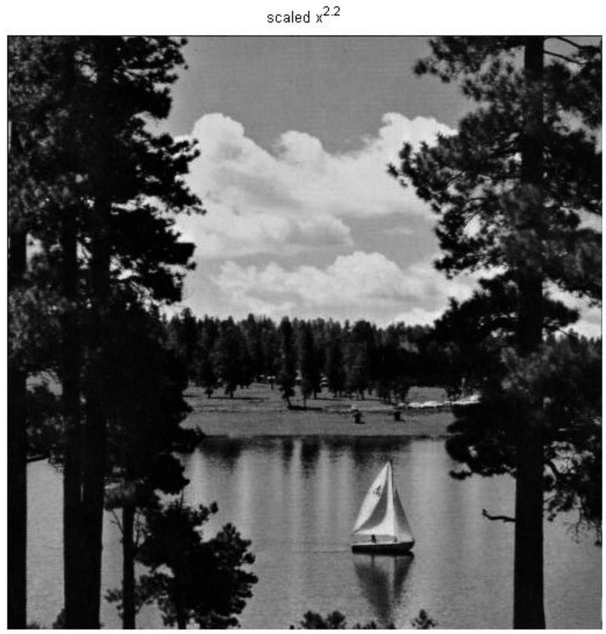

Figure 7.2–8. intensity domain image scaled for display

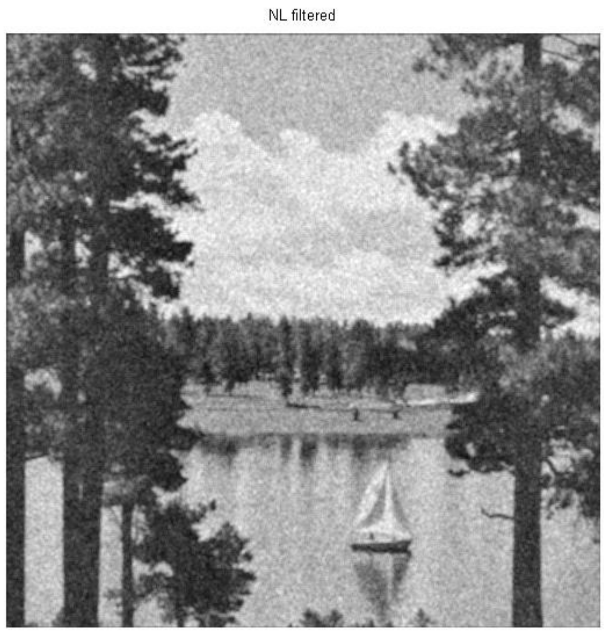

Figure 7.2–9. result of 3×3 box filtering in intensity domain

Figure 7.2–10. result of two passes through box filter in intensity domain

Figure 7.2–11. output of 3×3 median filter applied once

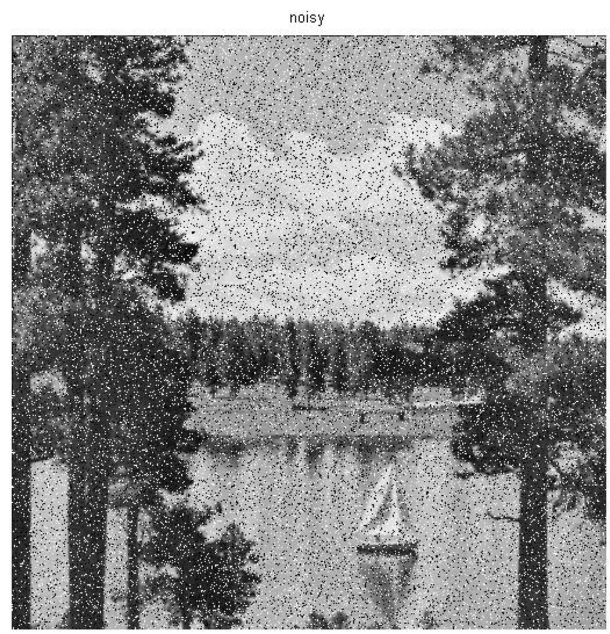

Figure 7.2–12. *Sailboat* with 'salt and pepper' noise with $p = 0.15$

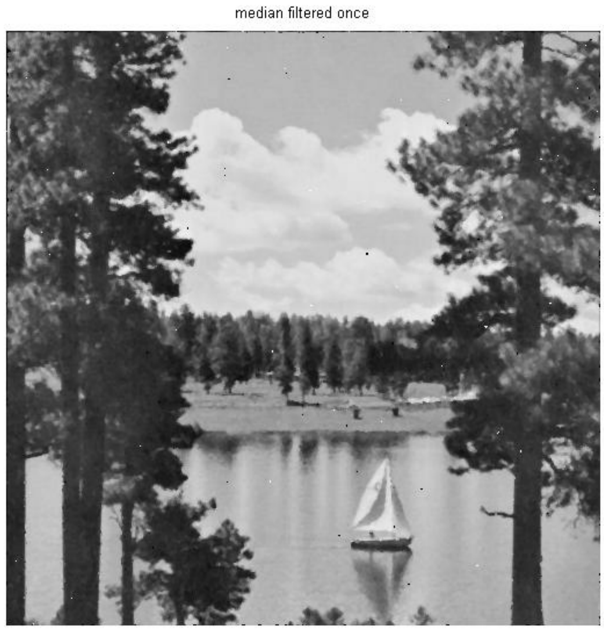

Figure 7.2–13. output of 3×3 median filter of 'salt and pepper' noisy original

7.3 IMAGE ANALYSIS

Figure 7.3–14. 256×256 gray-level version of *House* image

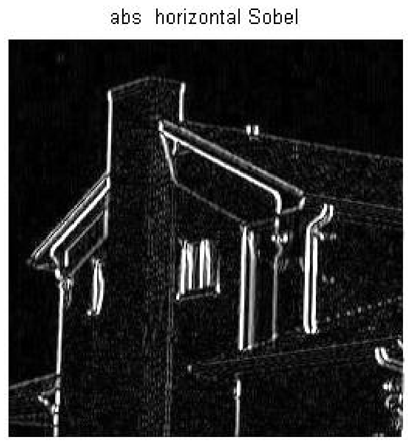

Figure 7.3–15. absolute value of output of horizontal Sobel filter

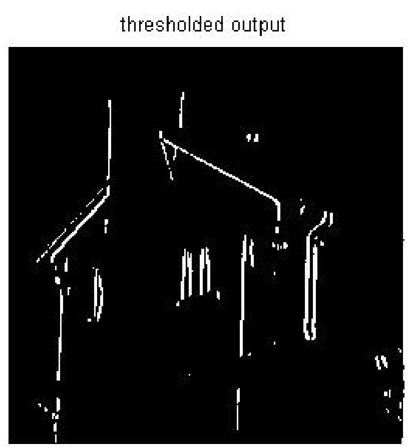

Figure 7.3–16. thresholded horizontal Sobel filter output at $\gamma = 200$

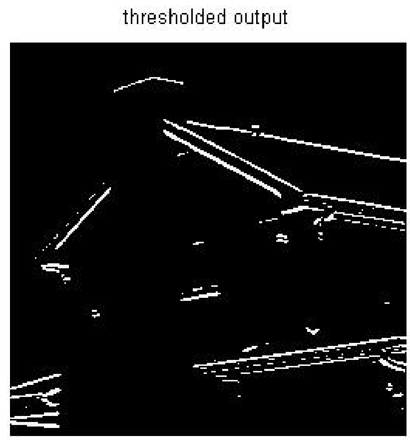

Figure 7.3–17. thresholded output of vertical Sobel filter with $\gamma = 200$

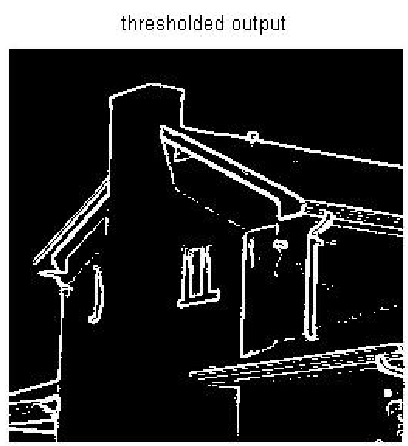

Figure 7.3–18. output of threshold on sum of absolute values of horizontal and vertical Sobel filters

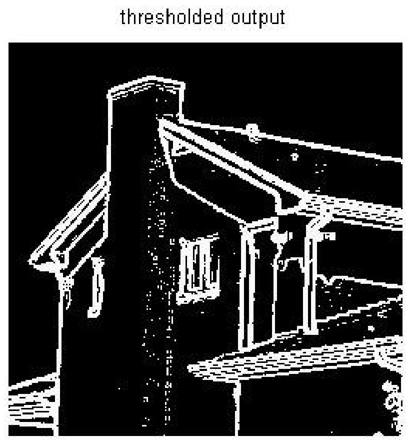

Figure 7.3–19. Sobel output with threshold $\gamma = 100$ for noise-free image

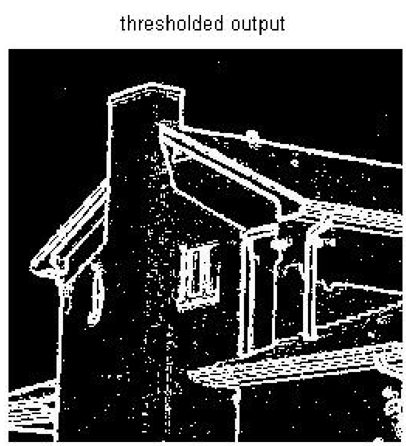

Figure 7.3–20. threshold of 100 on Sobel output with noisy image

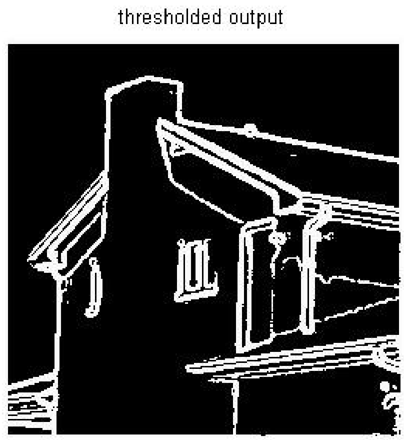

Figure 7.3–21. result of Sobel edge detection on smoothed noisy image $\gamma = 100$

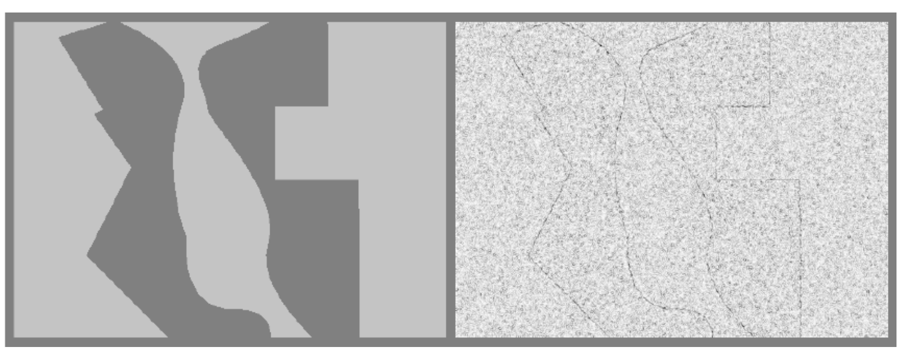

Figure 7.3–22. (a) original 334×432 gray level image, (b) noisy gradient image (from Cook and Delp [**??**] © 1995 IEEE)

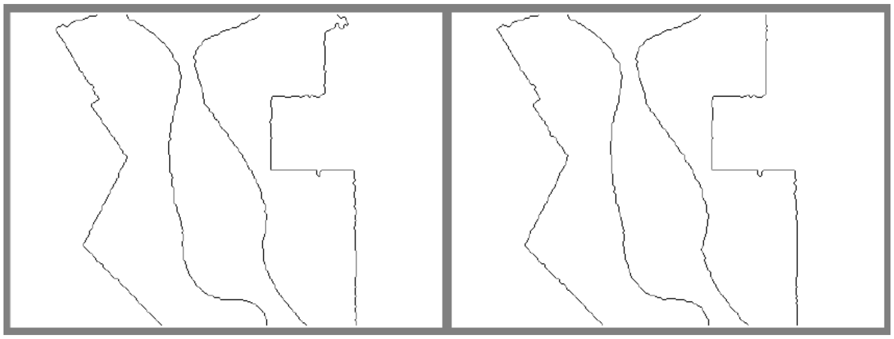

Figure 7.3–23. (a) SEL output from 2-level pyramid, (b) 3-level multiresolution SEL output. (from Cook and Delp [??] © 1995 IEEE)

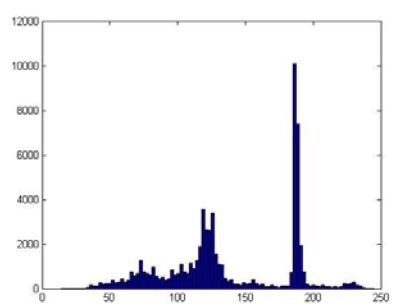

Figure 7.3–24. histogram of gray-level *House* image

Figure 7.3–25. result of manually thresholding gray-level house image at two most prominent minima of histogram

Figure 7.3–26. original 256×256 *Cameraman* image

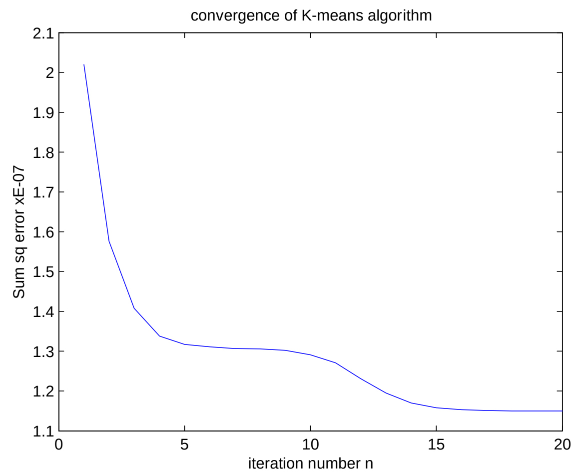

Figure 7.3–27. plot of convergence of sum squares of K-means algorithm

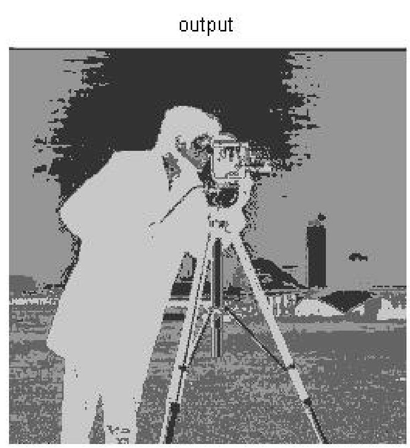

Figure 7.3–28. image showing the 4 class indices resulting from K-means algorithm

Figure 7.3–29. image showing the class means, i.e. the representative values in each class

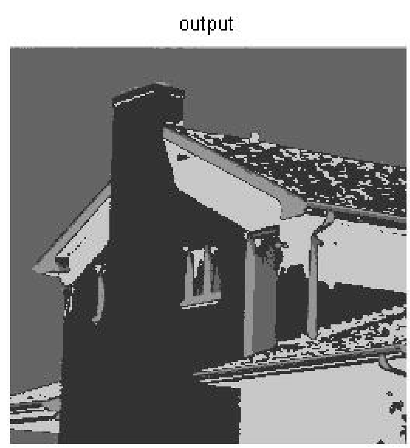

Figure 7.3–30. the index image of K-means result for color image *House*

Figure 7.3–31. greylevel 512×480 *Flower* image

Figure 7.3–32. region grown from seed location $(328, 341)$ with threshold 0.08

Figure 7.3–33. region grown from seed location $(328, 341)$ with threshold 0.2

7.4 OBJECT DETECTION

Figure 7.4–34. a frame from *Miss America* test clip

Figure 7.4–35. a four region segmentation of color image frame *Miss America*

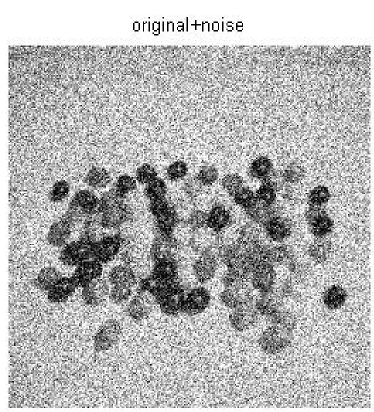

Figure 7.4–36. noisy jelly beans image

Figure 7.4–37. original jelly beans image

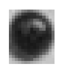

Figure 7.4–38. black jelly bean template

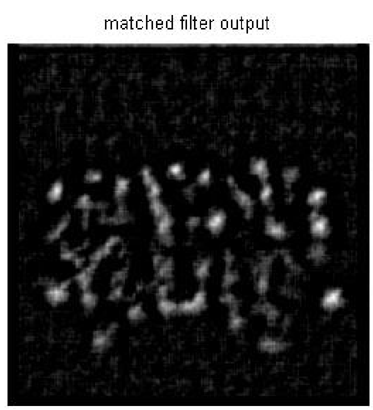

Figure 7.4–39. matched filter output image

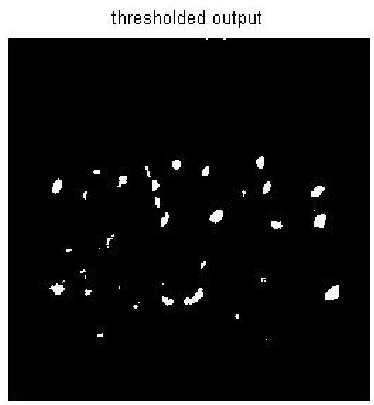

Figure 7.4–40. threshold output image, where white (250) indicates black jelly bean, and black (0) indicates its absence

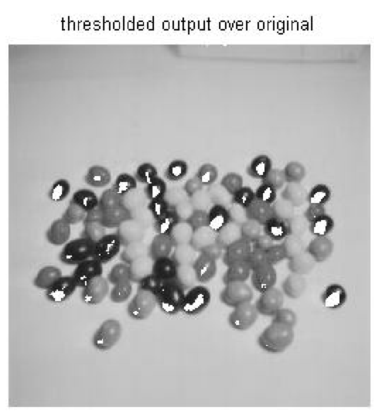

Figure 7.4–41. detector output superposed over original jelly bean image

7.5 CONCLUSIONS

7.6 PROBLEMS

Chapter 8

Image Estimation and Restoration

8.1 2-D RANDOM FIELDS

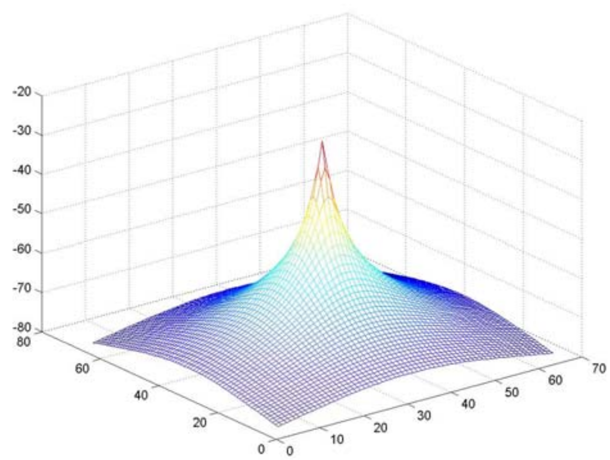

Figure 8.1–1. log or dB plot of example spectra

8.2 ESTIMATION FOR RANDOM FIELDS

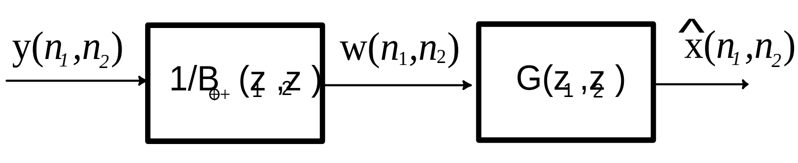

Figure 8.2–2. Whitening filter realization of Wiener filter.

8.3 2-D RECURSIVE ESTIMATION

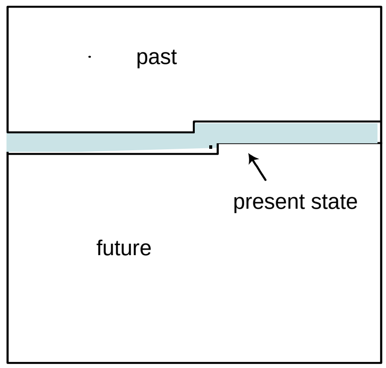

Figure 8.3–3. Illustration of the global state vector of a spatial Kalman filter

Figure 8.3–4. (a) 256×256 *Lena* - Original, (b) Lena + noise @ 10 dB input SNR

Figure 8.3–5. RUKF estimate of *Lena* from 10 dB noisy data

Figure 8.3–6. cameraman blurred by horizontal FIR blur of length 10. BSNR=40 dB

Figure 8.3–7. inhomogeneous Gaussian using 3-gains and residual model.

Figure 8.3–8. RUKF restoration using circulant blur model from area blur.

Figure 8.3–9. RUKF restoration from linear area blur model

8.4 INHOMOGENEOUS GAUSSIAN ESTIMATION

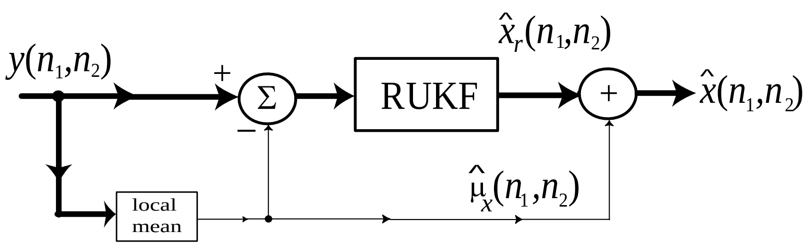

Figure 8.4–10. system diagram for inhomogeneous Gaussian estimation with RUKF

Figure 8.4–11. various inhomogeneous Gaussian estimates: $\begin{bmatrix} a & b \\ c & d \end{bmatrix}$, a- LSI, b- Wallis filter, c- residual RUKF, and d- normalized RUKF.

8.5 ESTIMATION IN THE SUBBAND/WAVELET DOMAIN

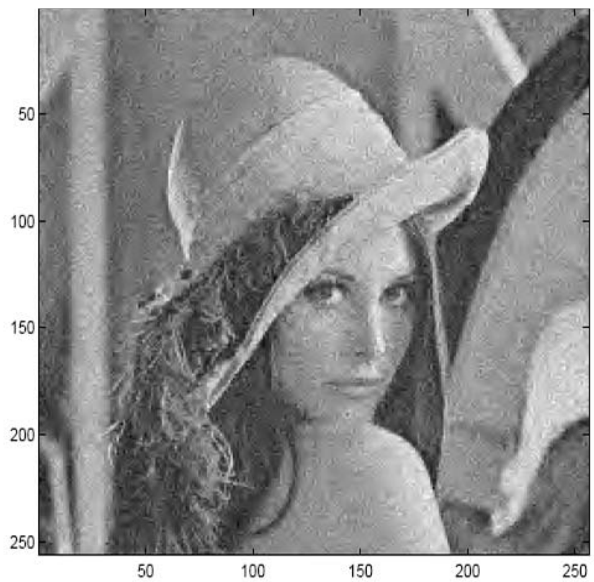

Figure 8.5–12. estimate using hard threhsold in SWT domain.

Figure 8.5–13. estimate using soft threshold in the SWT domain.

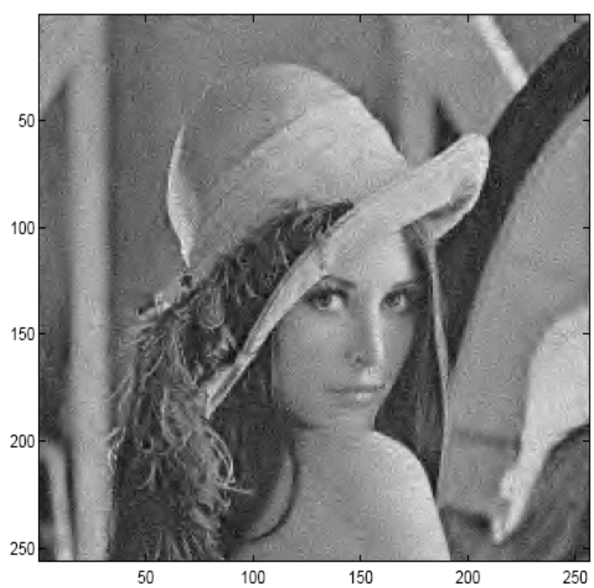

Figure 8.5–14. hard threshold $t = 40$ in OCSWT domain.

Figure 8.5–15. estimate using soft threshold in OCSWT domain.

8.6 BAYESIAN AND MAP ESTIMATION

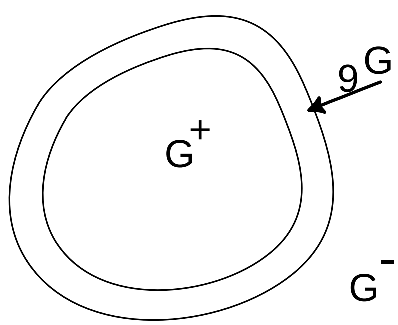

Figure 8.6–16. illustration of dependancy regions for noncaucal Markov field

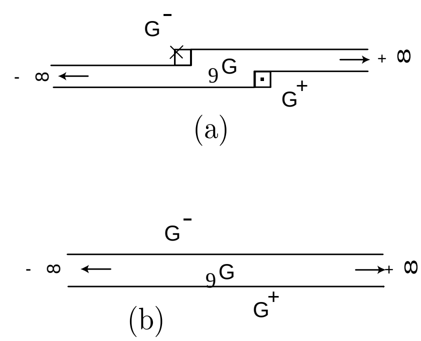

Figure 8.6–17. an illustration of two causal Markov concepts

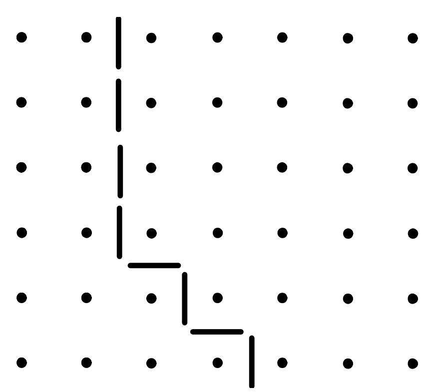

Figure 8.6–18. example of line field modeling edge in portion of fictitious image

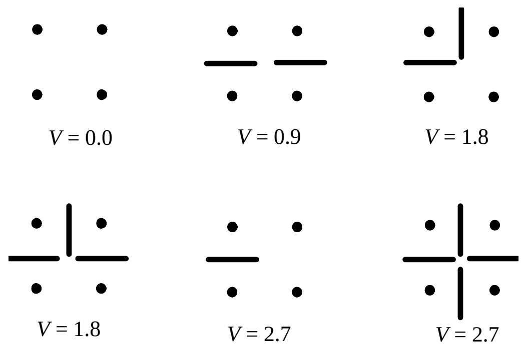

Figure 8.6–19. line field potential V values for indicated nearest neighbors (black line indicates bond broken)

Figure 8.6–20. example of Wiener filtering for Gauss Markov model at input SNR=10 dB

Figure 8.6–21. simulated annealing estimate for CGM model at input SNR=10 dB

Figure 8.6–22. input blurred image as BSNR=40 dB

Figure 8.6–23. blur restoration via Wiener filter

Figure 8.6–24. blur restoration via simulated annealing

Figure 8.6–25. Parallel SA restoration results: (a)-left MAP estimate, (b)-right MMSE estimate

8.7 IMAGE IDENTIFICATION AND RESTORATION

Figure 8.7–26. subband EM restoration of *cameraman* at BSNR = 40 dB, $\begin{bmatrix} a & b & c \\ d & e & f \end{bmatrix}$ *a*- original, *b*- blurred, *c*, fullband restored, *d*- LL subband restored, *e*- subband (LSI), *f*- subband (LSV) (from [**??**] © 1994 IEEE)

Figure 8.7–27. Lena image with additive Gaussian noise added to yield input SNR=10 dB.

Figure 8.7–28. output image with ISNR = 7.9 dB

Figure 8.7–29. from Left: Noisy, Right: Nonlocal means. (from Fig. 5 [**??**] © 2005 IEEE)

Figure 8.7–30. collaborative filtering on 256×256 House image. Left: noisy original, Right: estimate. (from Dabov et al [**??**] © 2007 IEEE)

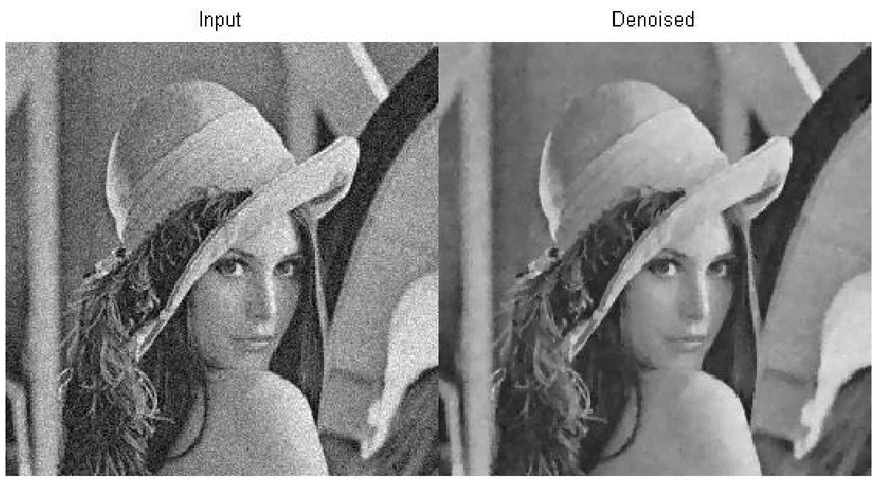

Figure 8.7–31. the 256×256 Lena 10 dB noisy image on the left produced the TV denoised output image on the right ISNR=6.1 dB

8.8 IMAGE SUPERRESOLUTION

Figure 8.8–32. Fig. 3 from Elad and Hel-Or [**??**]

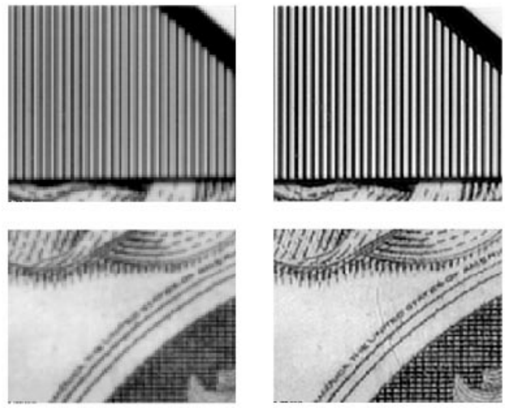

Figure 8.8–33. closeup of Fig. 8.8–32

8.9 COLOR IMAGE PROCESSING

8.10 CONCLUSIONS

8.11 PROBLEMS

Chapter 9

Digital Image Compression

9.1 INTRODUCTION

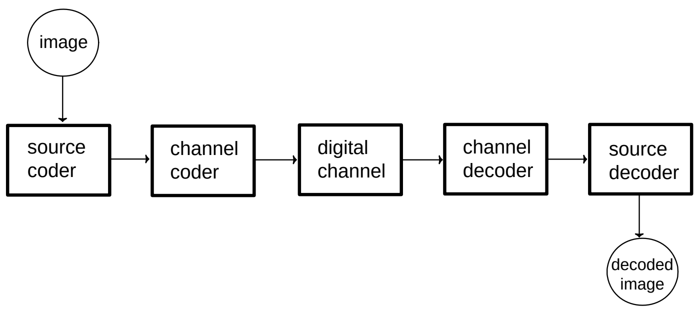

Figure 9.1–1. generic digital image communication system

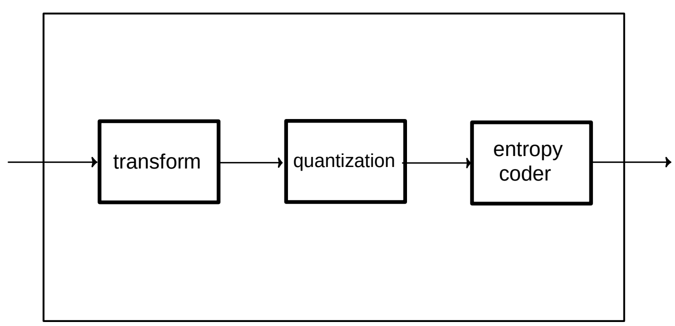

Figure 9.1–2. Generic source coding system diagram.

9.2 TRANSFORMATION

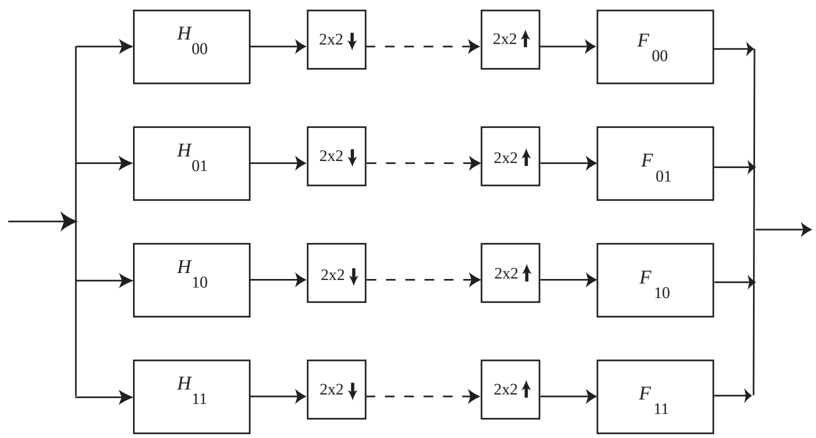

Figure 9.2–3. a general 2-D SWT/ISWT analysis/synthesis bank

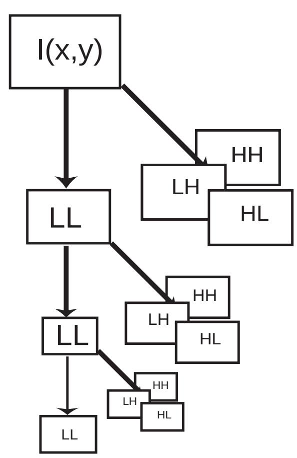

Figure 9.2–4. Illustration of dyadic (octave, wavelet) subband decomposition to three levels.

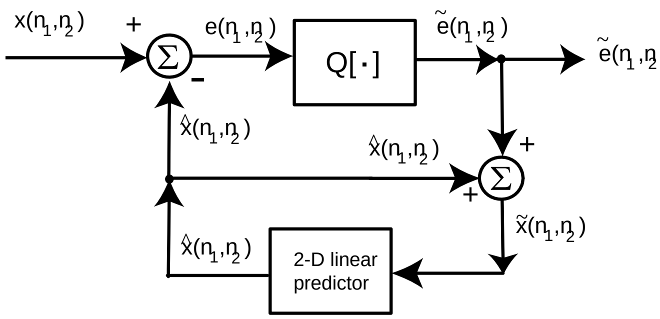

Figure 9.2–5. Diagram of a 2-D DPCM coder.

9.3 QUANTIZATION

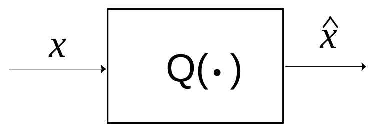

Figure 9.3–6. A scalar quantizer.

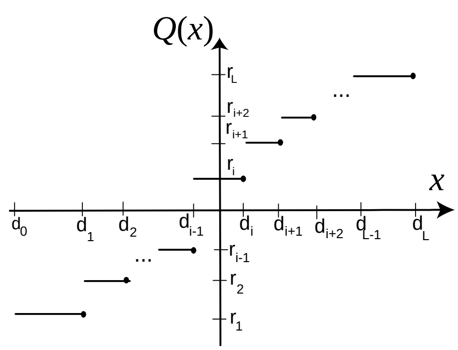

Figure 9.3–7. A quantizer characteristic that 'rounds to the left.'

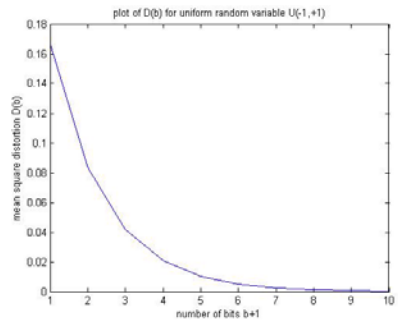

Figure 9.3–8. plot of MSE of uniform quantization of uniform random variable $U[-1,+1]$ versus number of bits b.

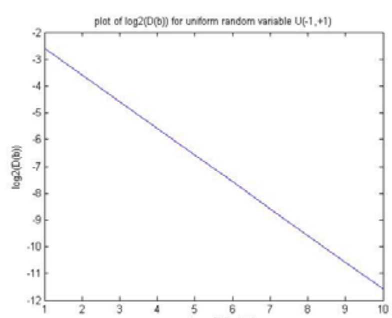

Figure 9.3–9. plot of $\log_2 D(b)$ versus b for uniform quantization of uniform random variable $U[-1,+1]$.

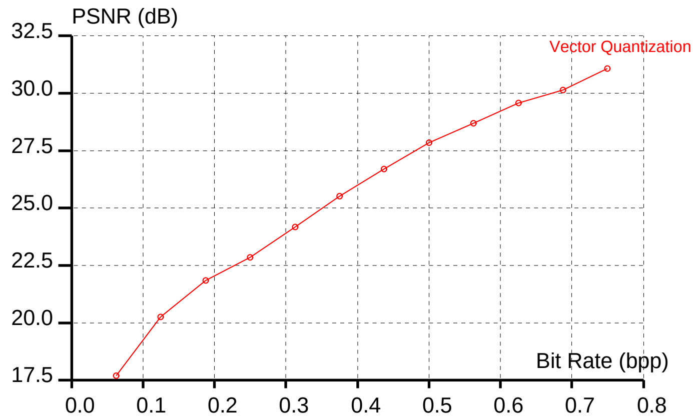

Figure 9.3–10. plot of PSNR versus bits for 4×4 VQ on cameraman image.

Figure 9.3–11. LBG VQ 4×4 result on cameraman: (a) 4 bits/vector, (b) 8 bits/vector

9.4 ENTROPY CODING

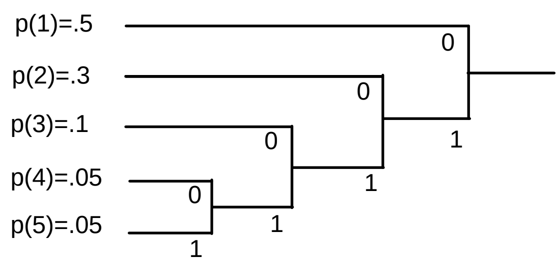

Figure 9.4–12. example of Huffman coding tree

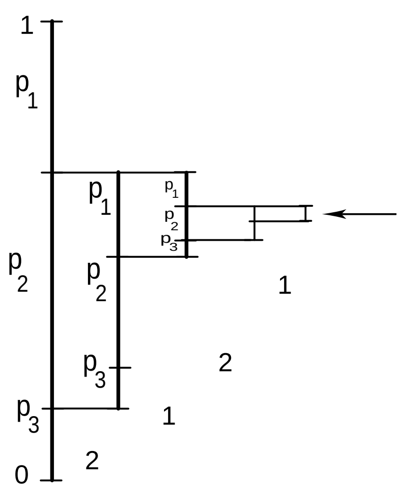

Figure 9.4–13. Illustration of an essential aspect of Arithmetic Coding

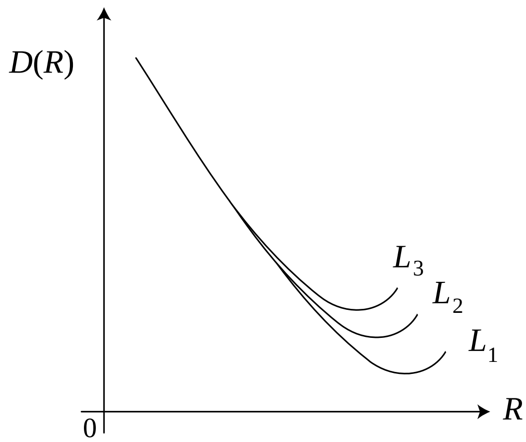

Figure 9.4–14. illustration of ECSQ joint quantizer and entropy encoder

9.5 DCT CODER

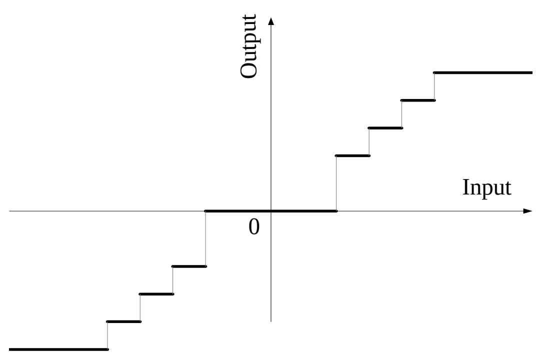

Figure 9.5–15. illustration of UTQ. Note its central deadzone.

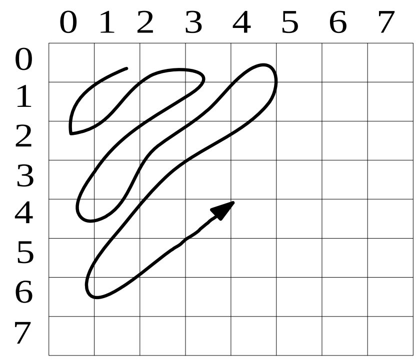

Figure 9.5–16. Illustration of zig-zag or serpentine scan of AC coefficients of 8×8 DCT.

Figure 9.5–17. original 252×256 Cameraman image

Figure 9.5–18. DCT coded image at 0.90 bpp.

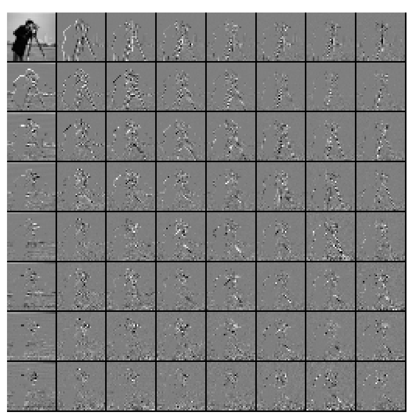

Figure 9.5–19. DCT coefficients of Cameraman image

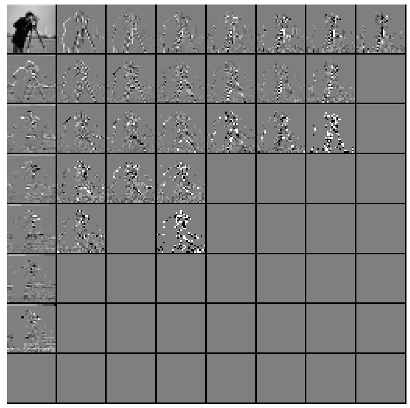

Figure 9.5–20. quantized DCT coefficients of Cameraman

9.6 SWT CODER

Figure 9.6–21. Original 512 × 125 Lena - 8 bits

Figure 9.6–22. 512×512 *Lena* coded by SBC at 1 bpp.

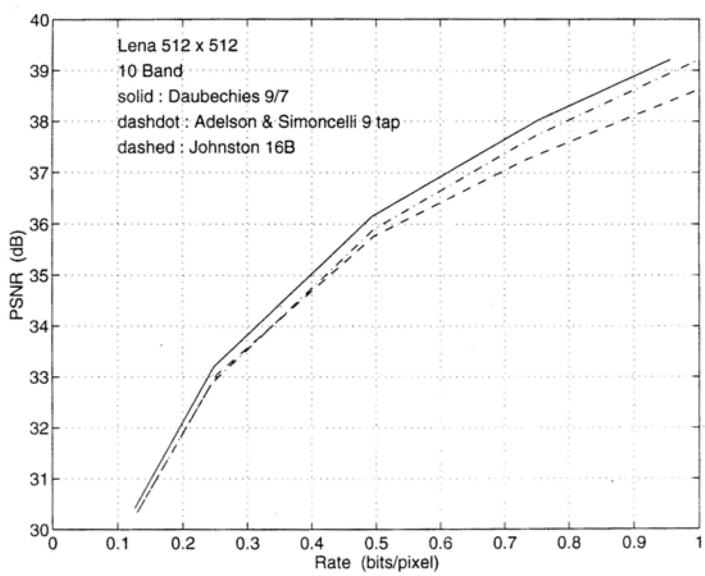

Figure 9.6–23. camparison of three subband/wavelet filters on *Lena* image

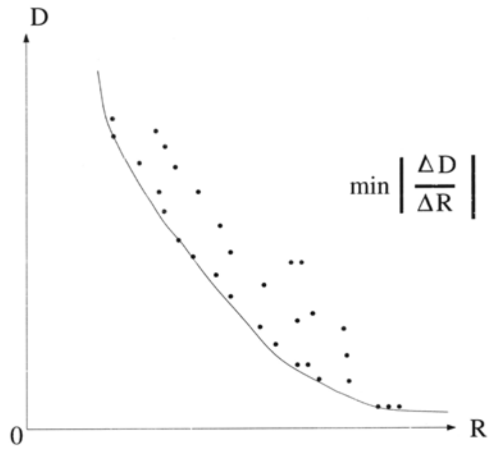

Figure 9.6–24. illustration of $D(R)$ in case of a discrete number of quantizer step sizes.

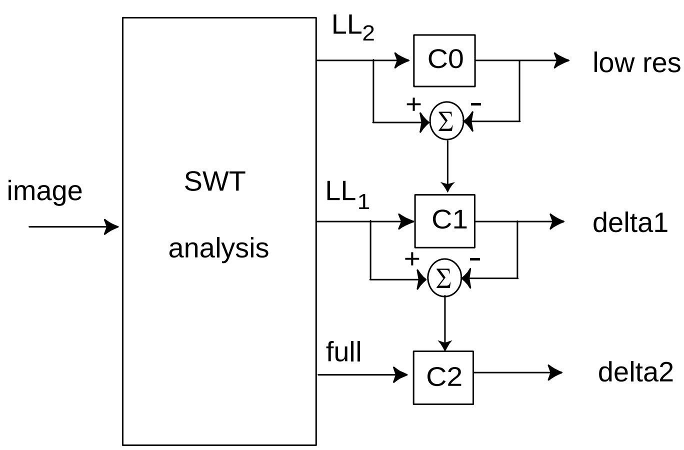

Figure 9.6–25. Multiresolution image coder with three decoded image resolutions (full, 1/2, and 1/4).

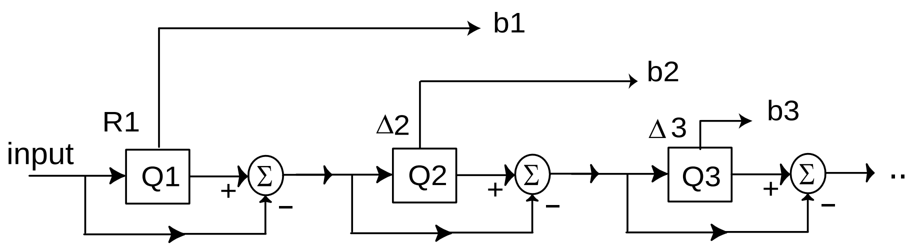

Figure 9.6–26. A cascade of three quantizers provides a quality scalable coding of input signal.

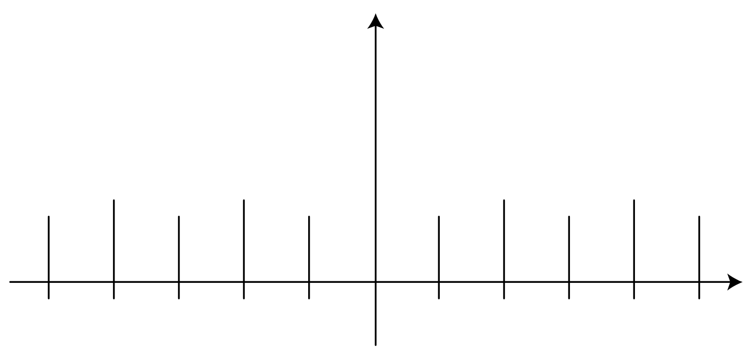

Figure 9.6–27. Illustration of scalar quantizer embedding. Solid lines are coarse quantizer decision levels. Dashed and solid lines together consttitute decision levels of the combined embedded quantizer.

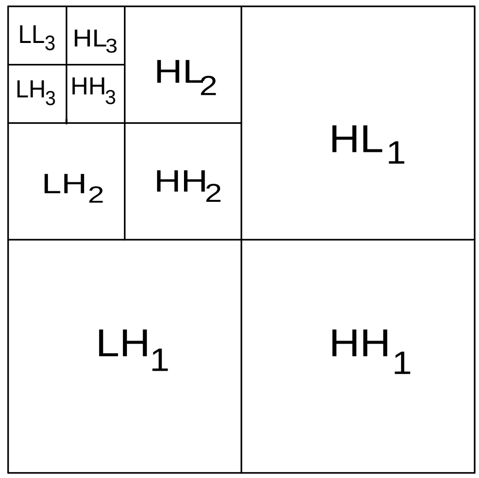

Figure 9.6–28. Illustration of subband/wavelet structure for the so-called dyadic (also called octave band or wavelet) decomposition, where the subbands XY_k are at the kth stage.

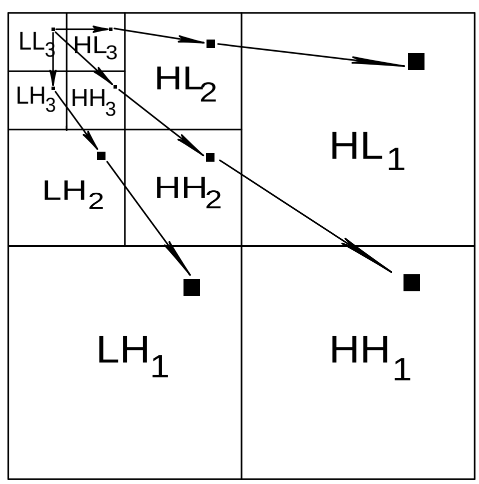

Figure 9.6–29. Illustration of parent-child relationship for trees of coefficients in EZW. Tree depth $N = 3$ levels.

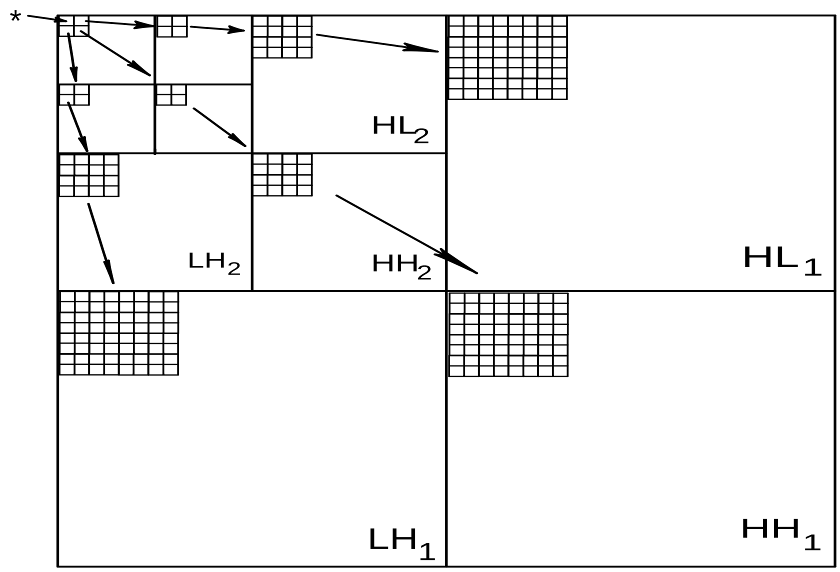

Figure 9.6–30. Illustration of SPIHT parent-child dependancies for 3-level tree.

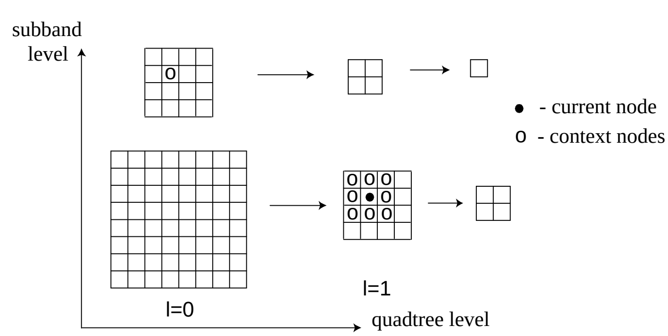

Figure 9.6–31. Illustration of context modeling for AC in EZBC.

9.7 JPEG 2000

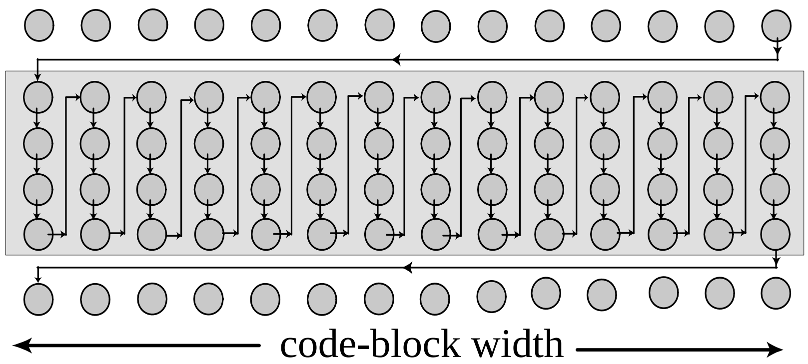

Figure 9.7–32. An illustration of how JPEG 2000 coder scans a 4-row stripe in a code block of wavelet coefficients (subband samples).

9.8 COLOR IMAGE CODING

9.9 DIRECTIONAL TRANSFORMS

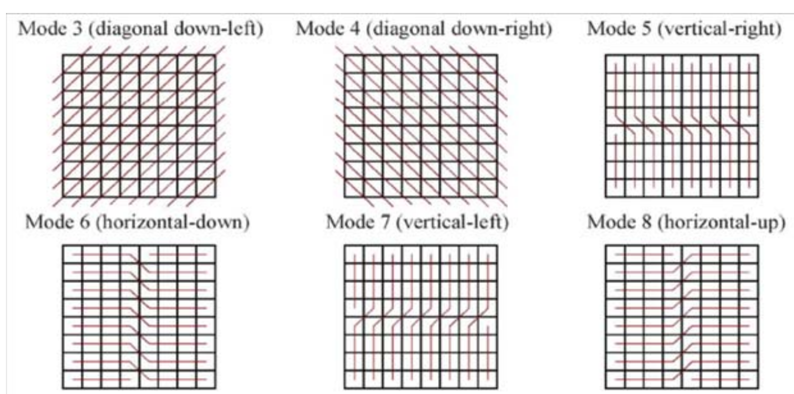

Figure 9.9–33. illustration of 6 new modes for directional DCT in [**??**] (© 2008 IEEE)

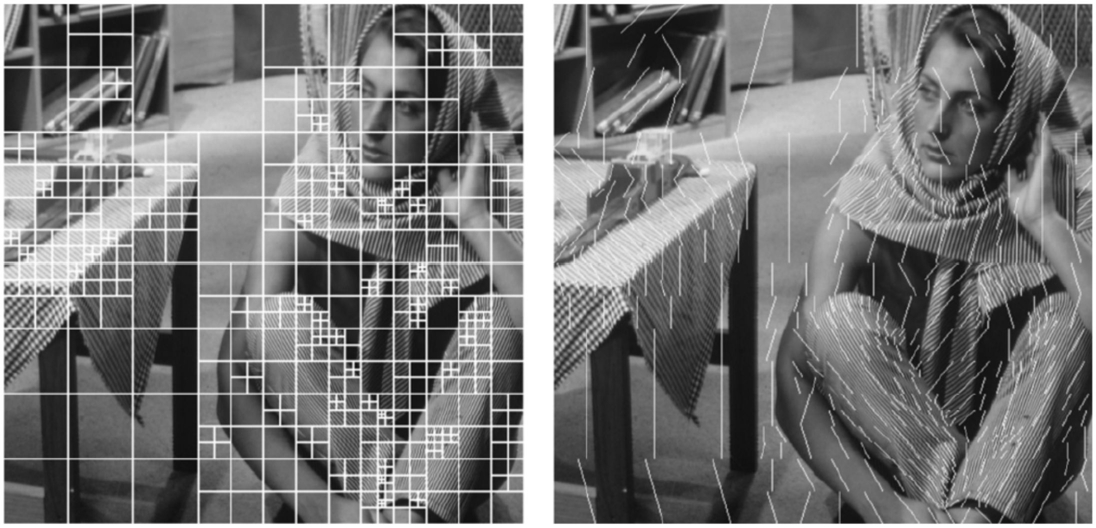

Figure 9.9–34. illustration of ADL quadtree and chosen directions overlayed on Barbara image. (from [Ding EtAl??] © 2007 IEEE)

Barbara JPEG 2000 coded with 5/3 SWT at 0.3 bpp (from [Ding2007??] © 2007 IEEE)

Barbara ADL coded with 5/3 SWT at 0.3 bpp (from [Ding2007??] © 2007 IEEE)

9.10 ROBUSTNESS CONSIDERATIONS

9.11 CONCLUSIONS

9.12 PROBLEMS

9.13 APPENDIX ON INFORMATION THEORY

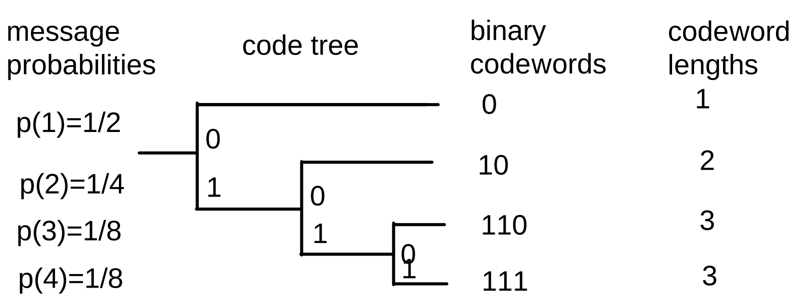

Figure 9.13–35. A convienent tree structure to calculate binary codewords given message probabilities.

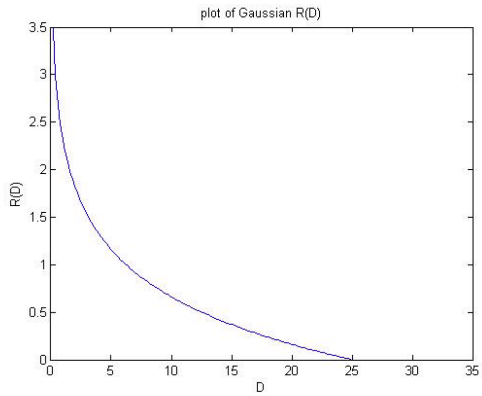

Figure 9.13–36. plot of Gaussian $R(D)$ function for $\sigma = 5$.

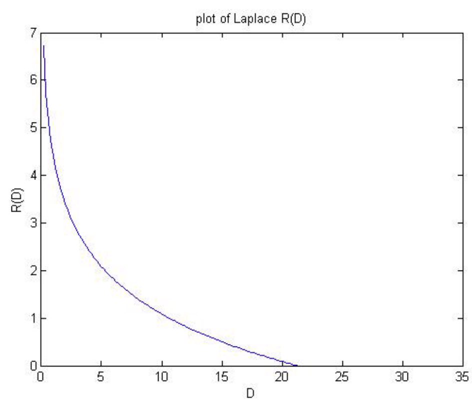

Figure 9.13–37.

Chapter 10

Three-Dimensional and Spatiotemporal Processing

10.1 3-D SIGNALS AND SYSTEMS

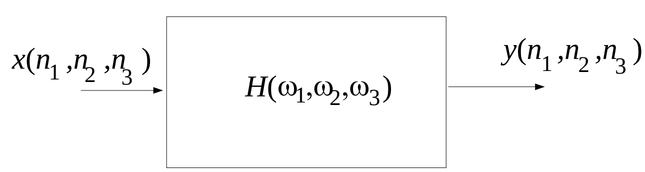

Figure 10.1–1. A 3-D system characterized by its frequency response.

10.2 3-D SAMPLING AND RECONSTRUCTION

10.3 SPATIOTEMPORAL SIGNAL PROCESSING

10.4 SPATIOTEMPORAL MARKOV MODELS

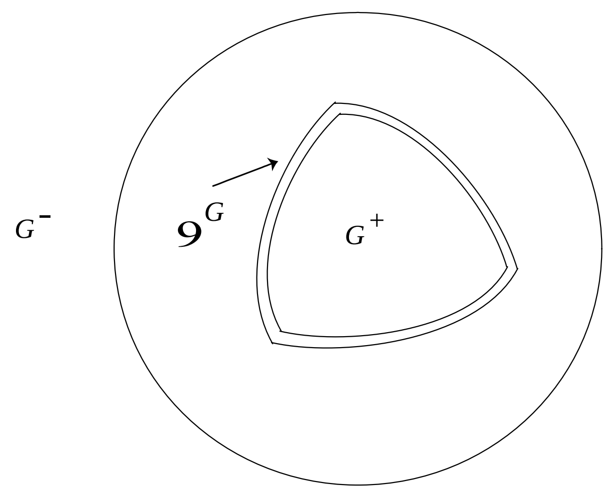

Figure 10.4–2. Illustration of noncausal Markov field regions.

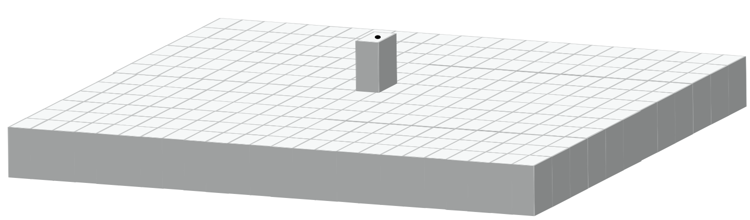

Figure 10.4–3. the dot · indicates the present and the plane below is the immediate past.

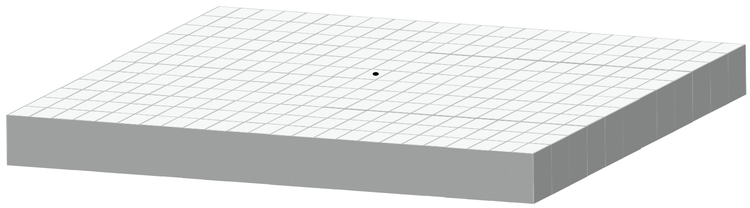

Figure 10.4–4. the dot · indicates the present and it is surounded by the immediate past.

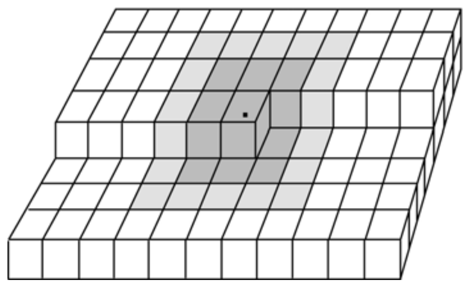

Figure 10.4–5. an illustration of 3-D Kalman reduced support regions

10.5 CONCLUSIONS

10.6 PROBLEMS

Chapter 11

Digital Video Processing

11.1 INTERFRAME PROCESSING

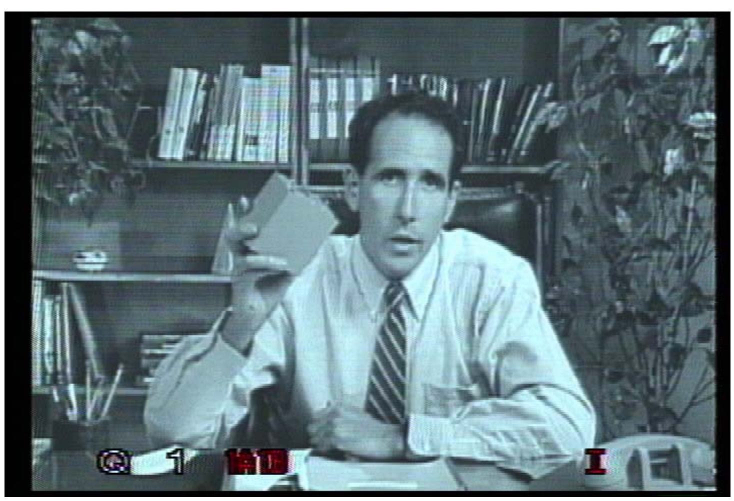

Figure 11.1–1. a frame from original CIF clip *salesman*

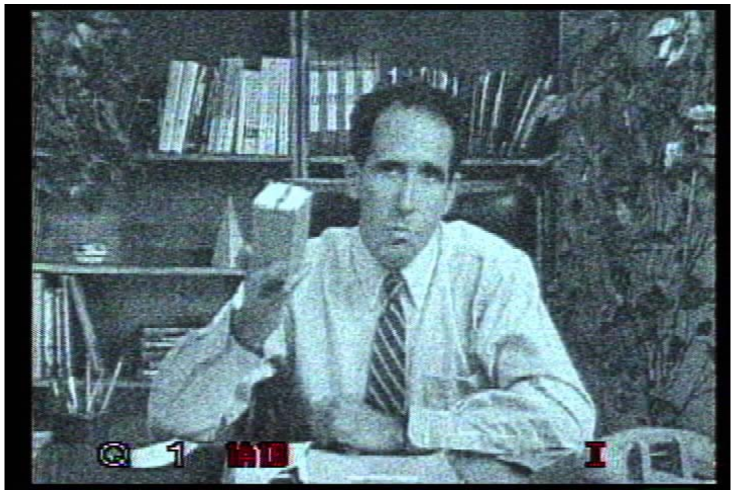

Figure 11.1–2. a frame from salesman with white noise added to achieve SNR= 10 dB

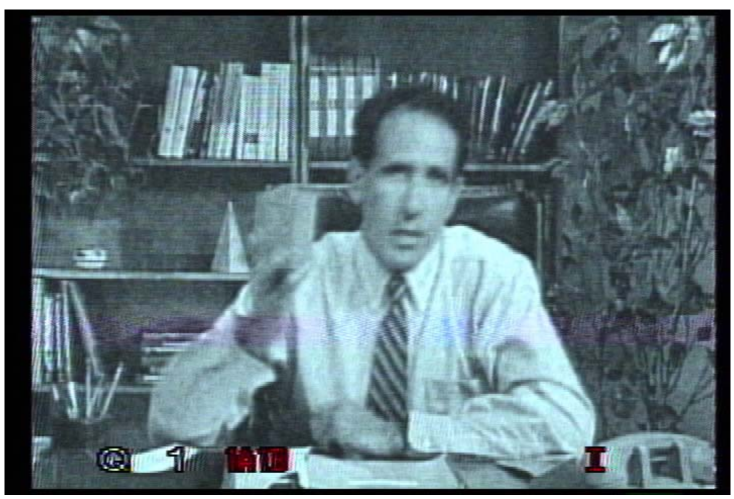

Figure 11.1–3. a frame from 3D-RUKF estimate.

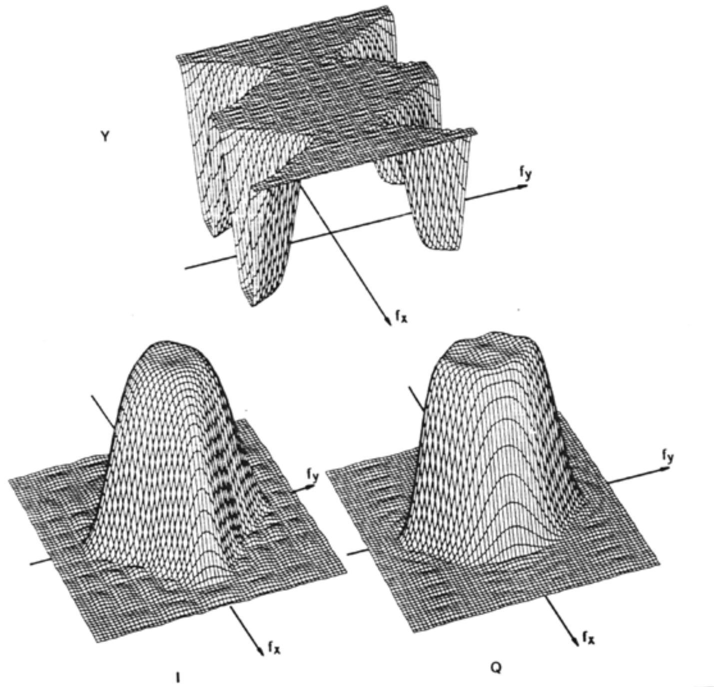

Figure 11.1–4. 2-D filter responses for generalized NTSC encoding of Y, I, and Q components [**??**] © 1988 SMPTE

Figure 11.1–5. (a) properly optimized or compensated lowpass filtering of test signal. [**??**] © 2000 John Wiley

Figure 11.1–6. (b) non-optimized showing over-smoothing. [**??**] © 2000 John Wiley

Figure 11.1–7. (c) over-optimized showing ringing. [**??**] © 2000 John Wiley

11.2 MOTION ESTIMATION AND MOTION COMPENSATION

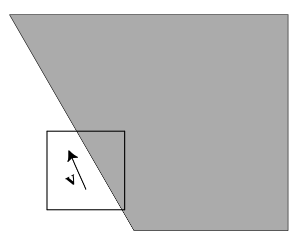

Figure 11.2–8. Illustration of the *aperture problem* with the square indicating the aperture size.

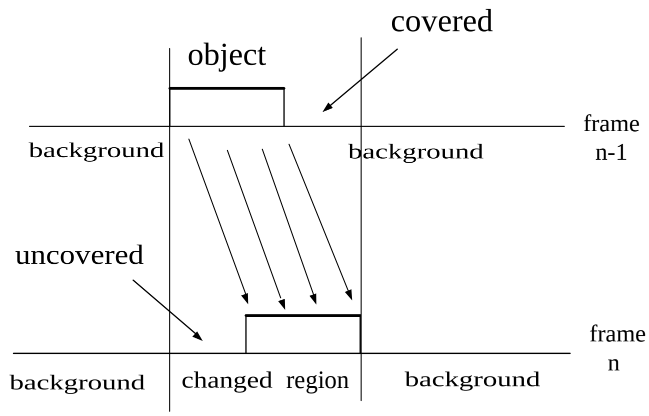

Figure 11.2–9. Illustration of covering and uncovering of background by object moving in the foreground.

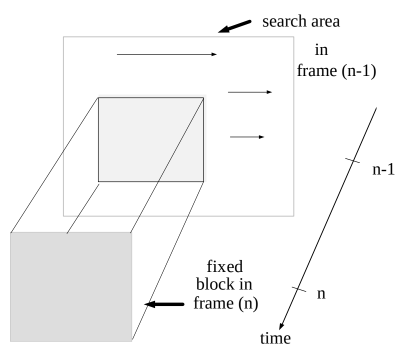

Figure 11.2–10. Illustration of simple block matching.

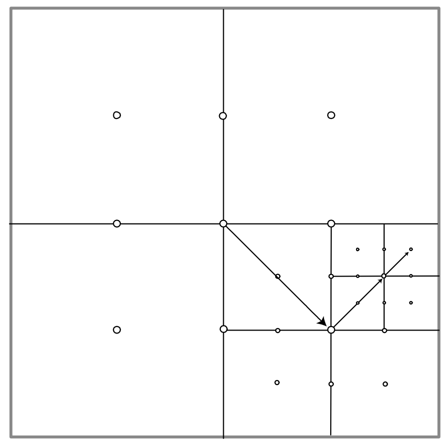

Figure 11.2–11. an illustration of 3-step block matching

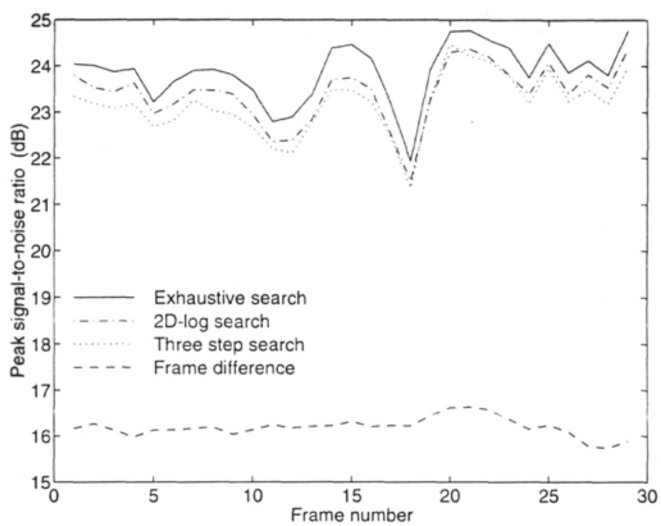

Figure 11.2–12. Illustration of PSNR performance of exhaustive, 2D log, 3-step search, and simple frame difference [??] © 1995 Academic Press

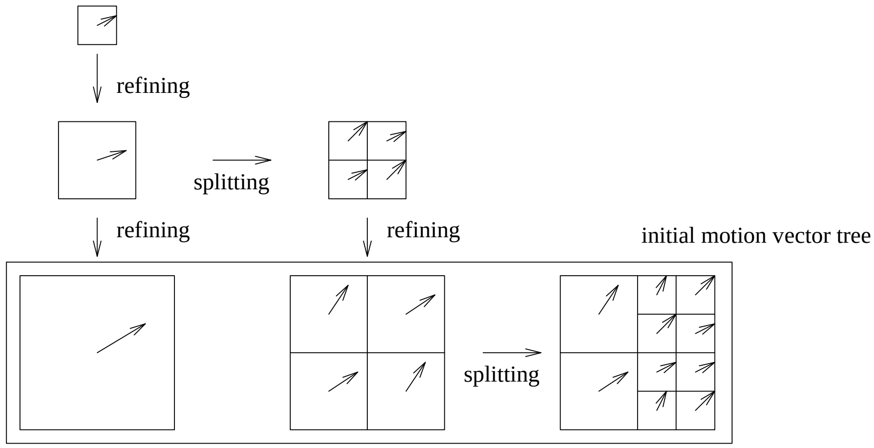

Figure 11.2–13. an illustration of the refining and spliting process in HVSBM

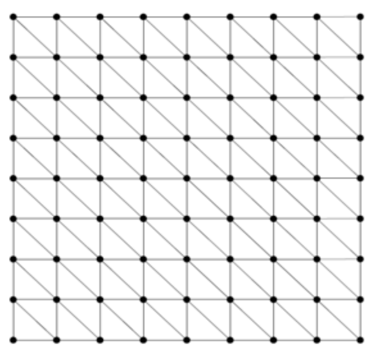

Figure 11.2–14. illustration of regular triangular mesh grid on target frame

Figure 11.2–15. frame 94 of Foreman with fixed-size triangular grid overlaid

Figure 11.2–16. frame 93 of Forman with warped grid overlaid

Figure 11.2–17. warped prediction of Foreman frame 94 from preceeding frame using triagular fixed-size mesh matching

Figure 11.2–18. fixed-size block matching prediction of frame 94 of Foreman from preceeding frame.

11.3 MOTION-COMPENSATED FILTERING

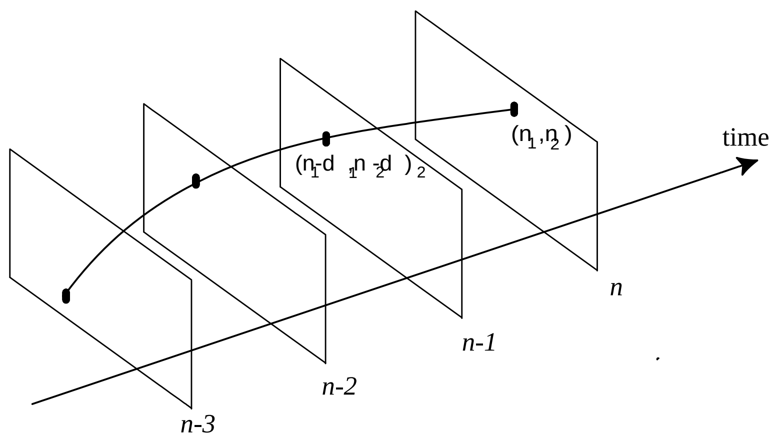

Figure 11.3–19. An illustration of motion compensated filtering along a motion path.

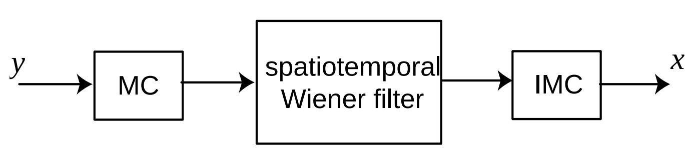

Figure 11.3–20. Illustration of MC warping followed by Wiener filter followed by inverse warping (IMC).

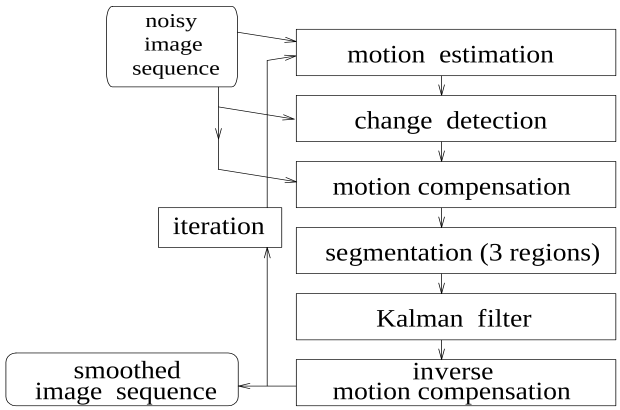

Figure 11.3–21. System diagram for motion compensated spatiotemporal Kalman filter

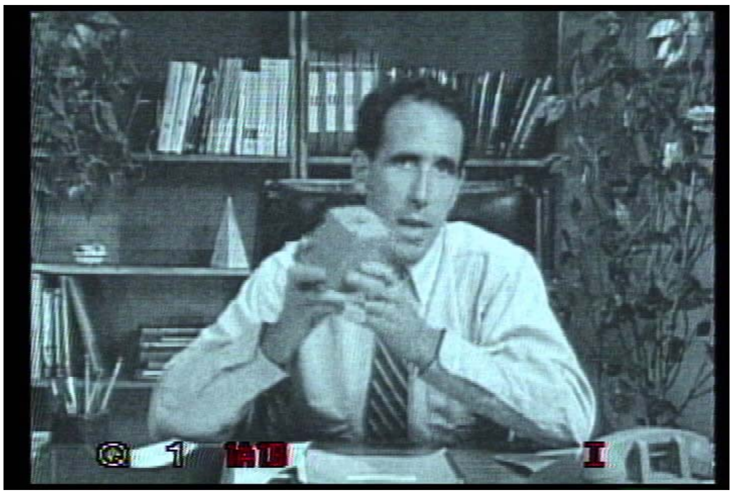

Figure 11.3–22. a frame from MC-RUKF

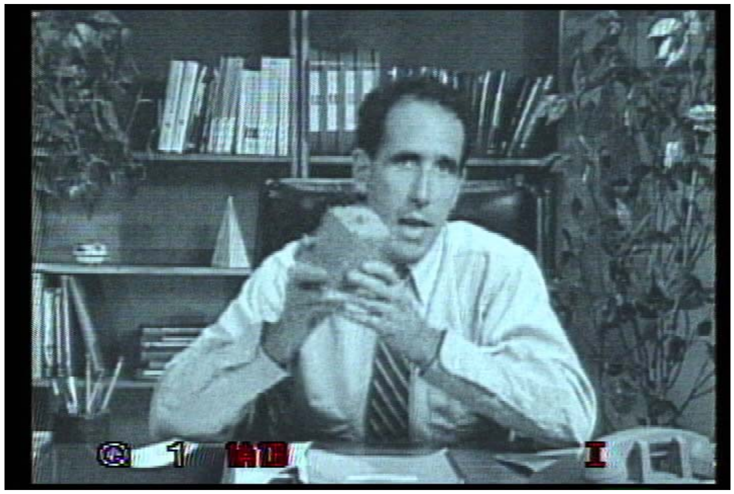

Figure 11.3–23. a frame from MM MC-RUKF

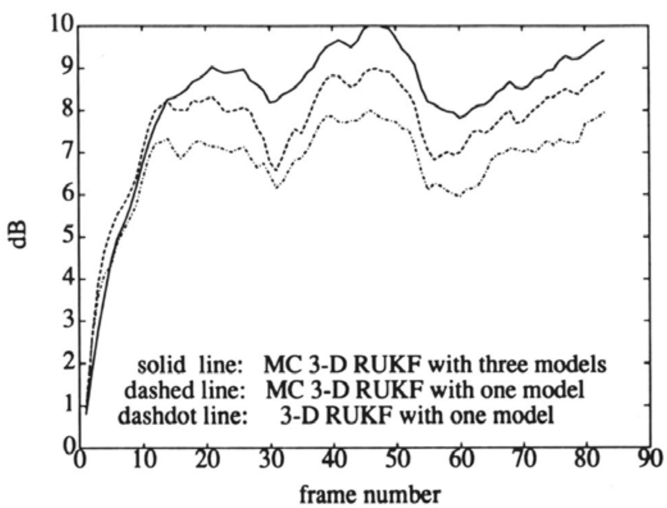

Figure 11.3–24. plot of SNR improvements versus frame number for MM-MC, MC-, and 3-D RUKF on noisy *Cameraman* clip.

Figure 11.3–25. a frame from a linearly interpolated temporal upconversion of *Miss America* from 5 to 30 fps

Figure 11.3–26. a frame from motion compensated temporal unconversion of *Miss America* from 5 to 30 fps.

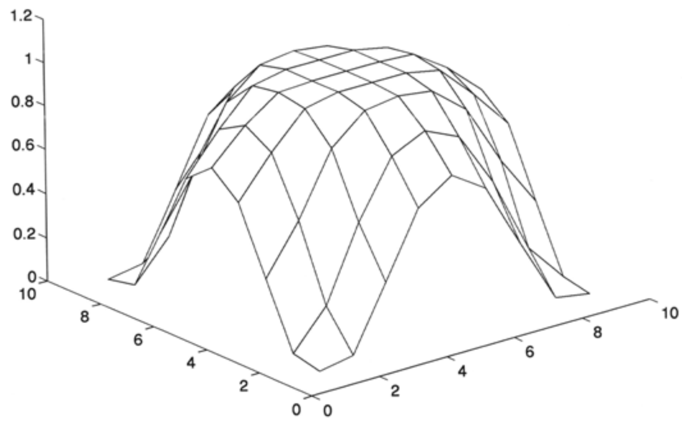

Figure 11.3–27. sketch of diamond filter response in vertical-temporal frequency domain

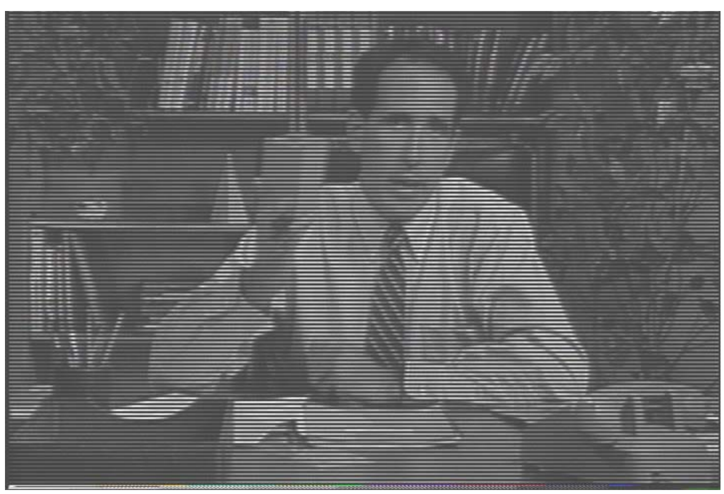

Figure 11.3–28. one field from the interlace version of *salesman*.

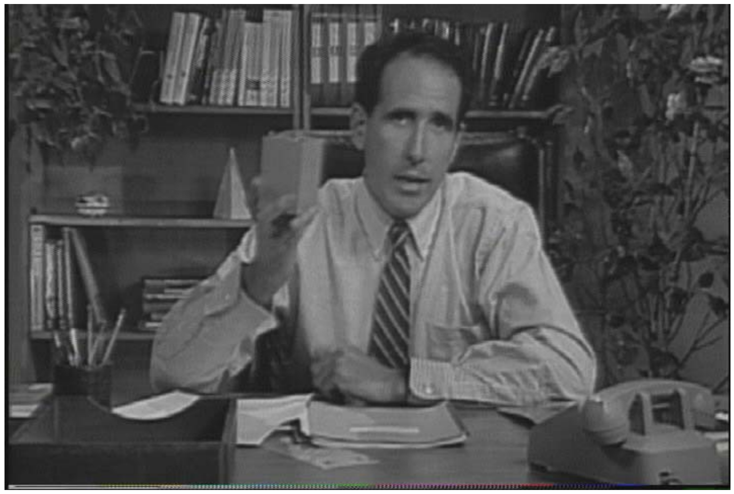

Figure 11.3–29. a progressive frame from the diamond filter ($v \times t$) output for an interlaced input.

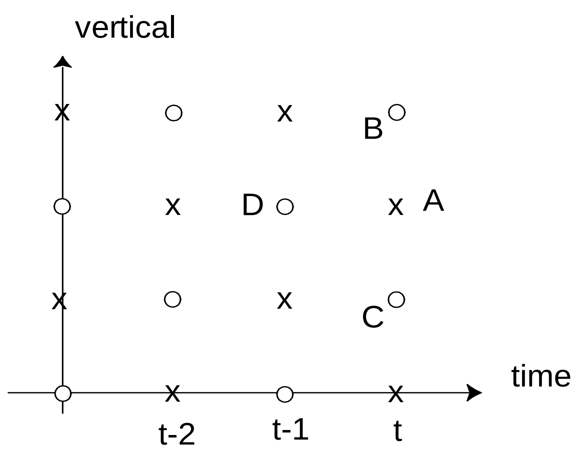

Figure 11.3–30. illustration of pixels input (B-D) to median filter deinterlacer

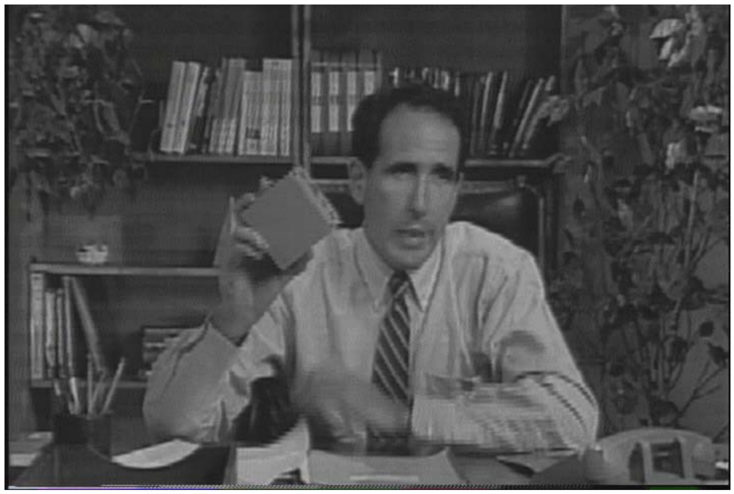

Figure 11.3–31. a de-interlaced frame of *Salesman* by the adaptive median filter.

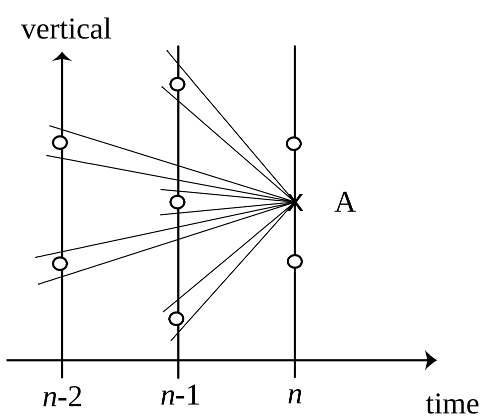

Figure 11.3–32. an illustration of cone approach to motion compensated de-interlacing.

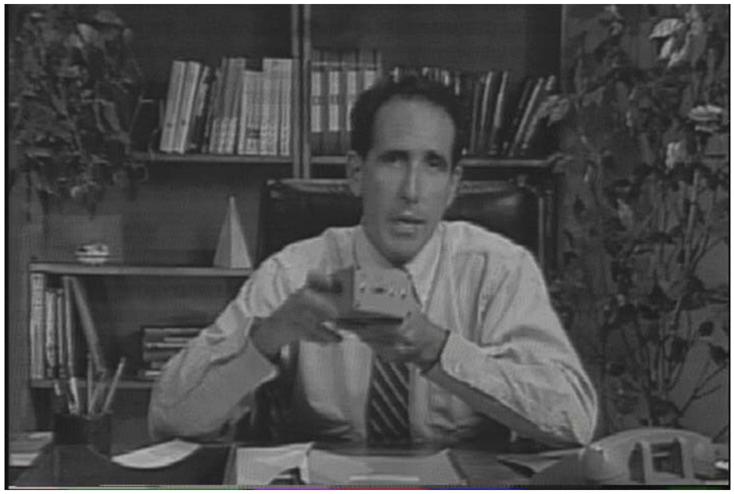

Figure 11.3–33. an MC de-interlaced *Salesman* frame.

11.4 BAYESIAN METHOD FOR ESTIMATING MOTION

Figure 11.4–34. predicted frame via block-based motion © 1999 IEEE

Figure 11.4–35. predicted frame via dense motion estimate © 1999 IEEE

Figure 11.4–36. predicted frame via region-based estimate © 1999 IEEE

Figure 11.4–37. prediction error frame for block-based motion © 1999 IEEE

Figure 11.4–38. prediction error frame for dense motion © 1999 IEEE

Figure 11.4–39. prediction error frame for region-based motion © 1999 IEEE

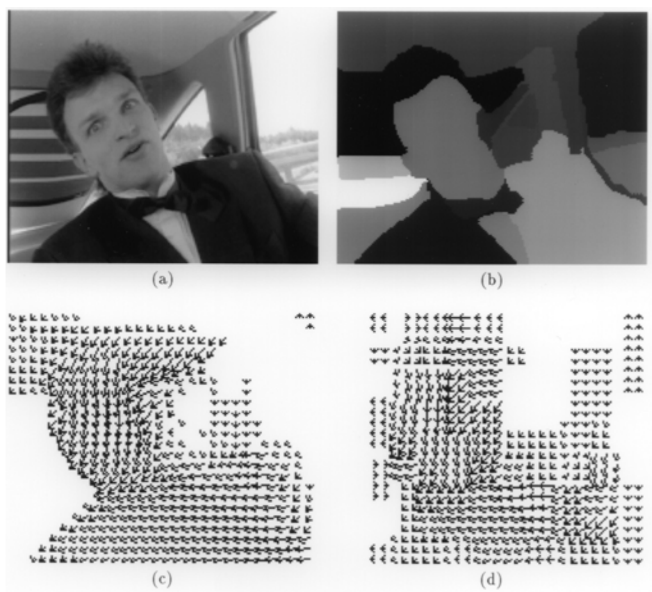

Figure 11.4–40. (a) original, (b) joint segmentation, (c) block-based motion, (d) joint motion

11.5 RESTORATION OF DEGRADED VIDEO AND FILM

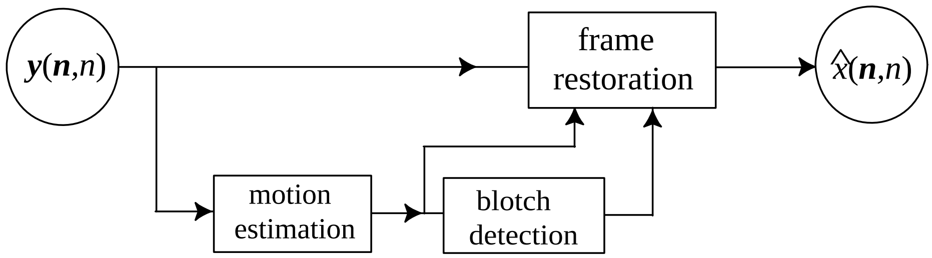

Figure 11.5–41. an illustration of video restoration in presence of blotch type artifacts.

11.6 SUPER-RESOLUTION OF VIDEO

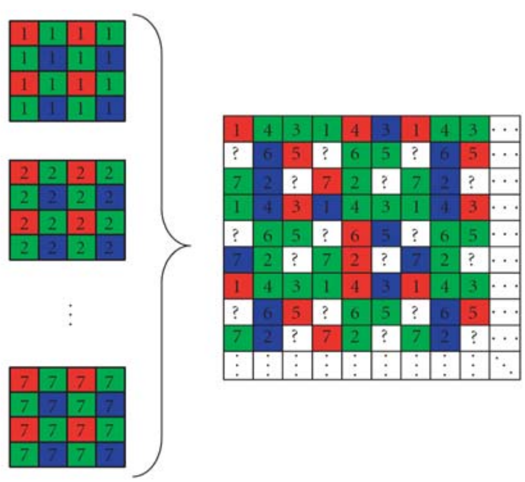

Figure 11.6–42. an illustration of color filter subsampling effect. (Fig. 3 from [**??**] with permission)

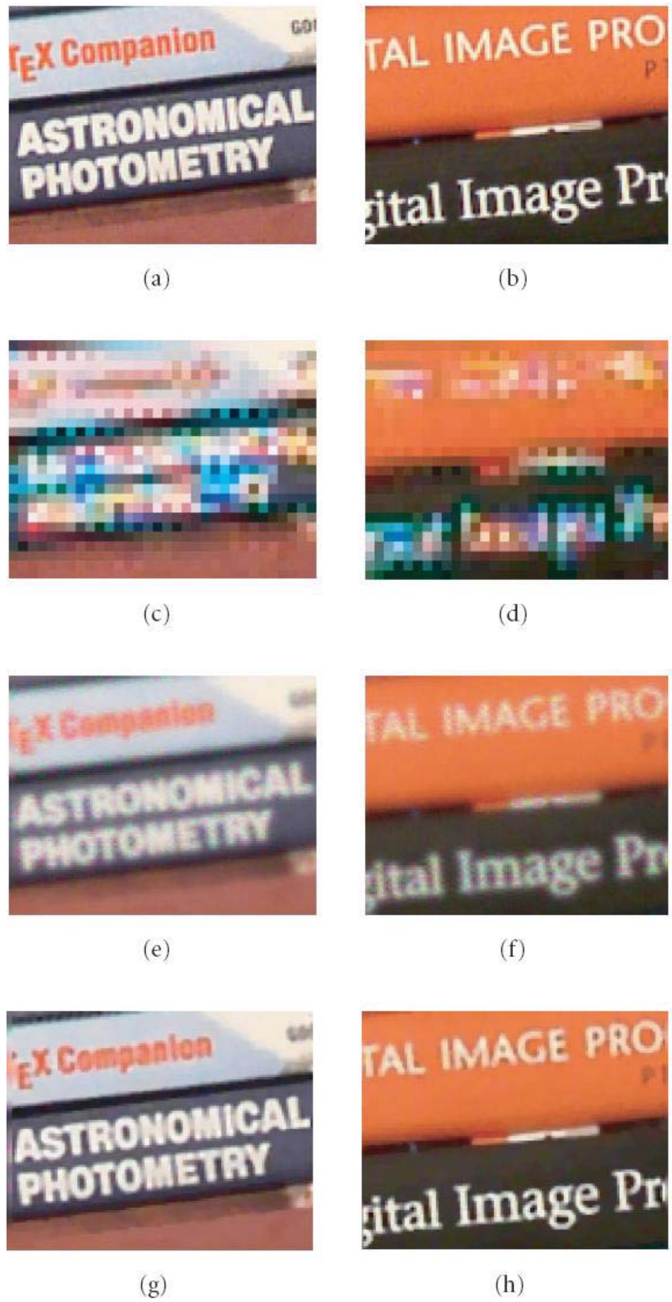

Figure 11.6–43. Fig. 5 from [**??**]

11.7 CONCLUSIONS

11.8 PROBLEMS

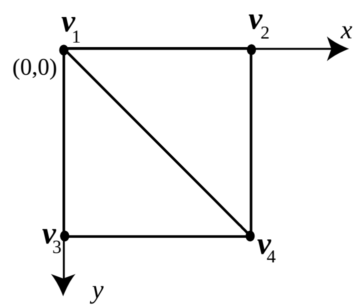

Figure 11.8–44. one cell of a triangular mesh with indicated velocities $\boldsymbol{v}_i, i = 1 - 4$, at the control points.

Chapter 12

Digital Video Compression

12.1 INTRAFRAME CODING

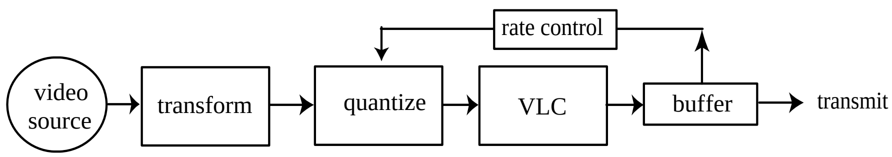

Figure 12.1–1. Illustration of intraframe video coding with rate control

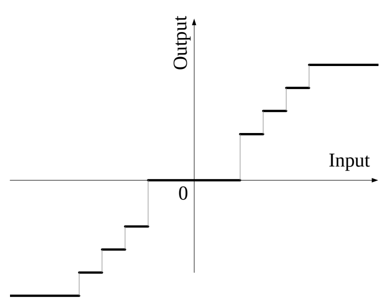

Figure 12.1–2. illustration of uniform threshold quantizer (UTQ), named for its deadzone at the origin.

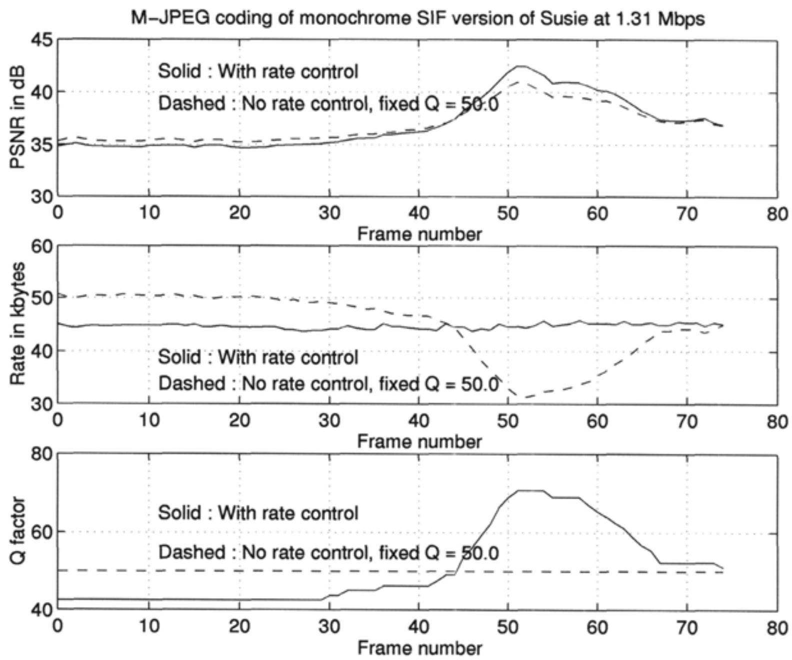

Figure 12.1–3. rate control of M-JPEG on *Susie* clip

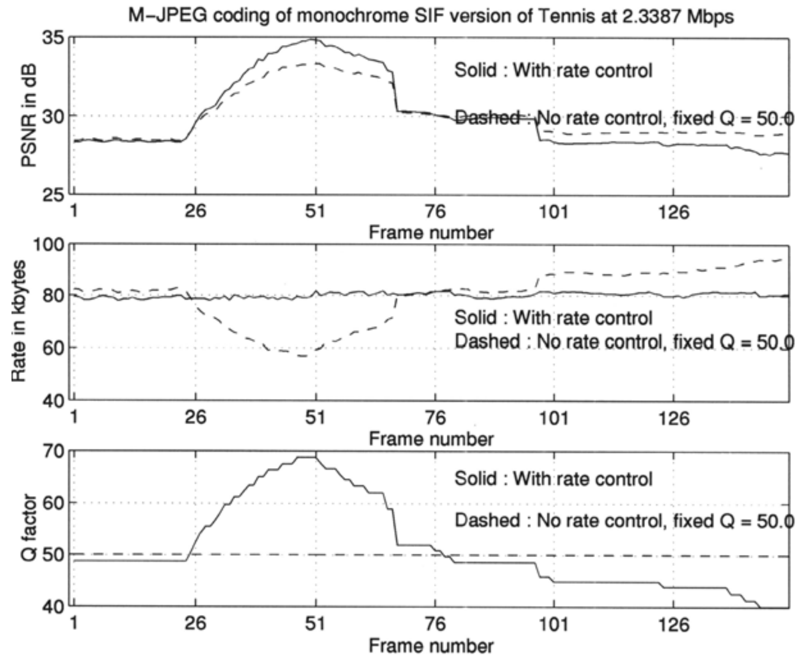

Figure 12.1–4. an illustration of rate control performance for M-JPEG coding of *Tennis* clip.

Figure 12.1–5. 4:1:1 color subsamling pattern of DV in the so-called 525/30 or NTSC system.

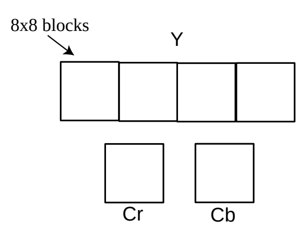

Figure 12.1–6. The DV macroblock (MB) for the NTSC (525/30) system.

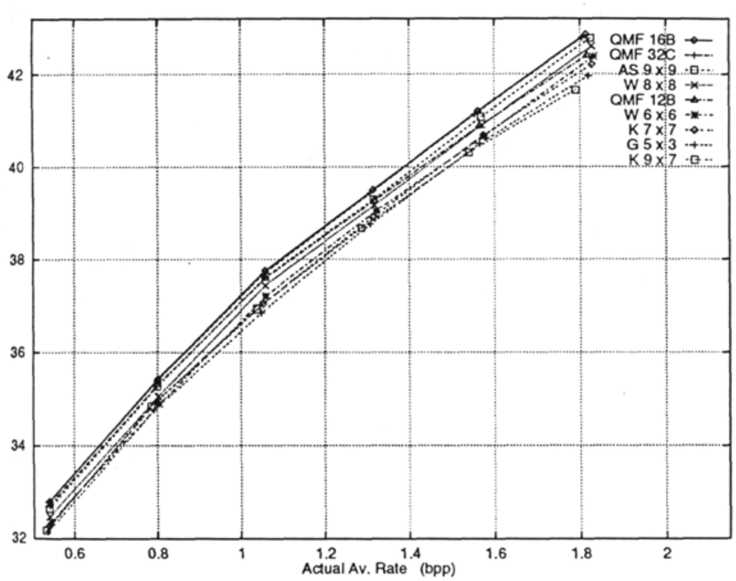

Figure 12.1–7. comparison of various SWT filters for intraframe video compression

12.2 INTERFRAME CODING

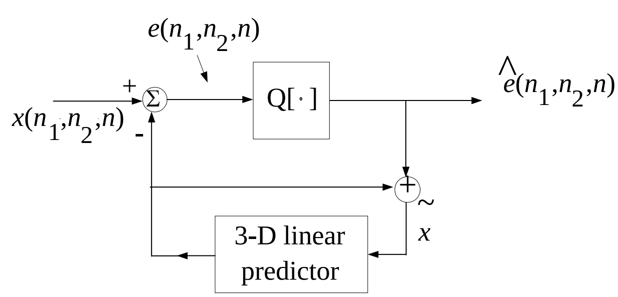

Figure 12.2–8. spatiotemporal generalization of DPCM with spatiotemporal predictor.

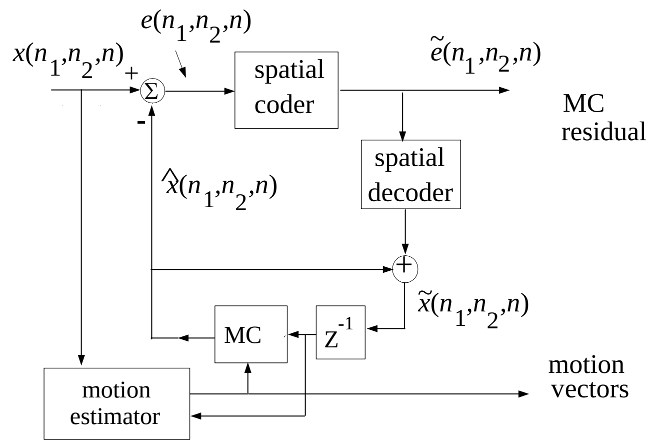

Figure 12.2–9. illustrative system diagram for motion compensated DPCM

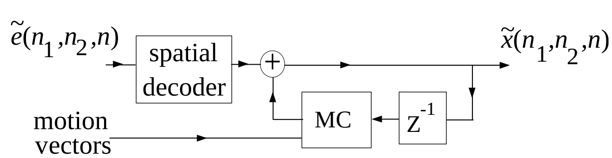

Figure 12.2–10. the hybrid decoder

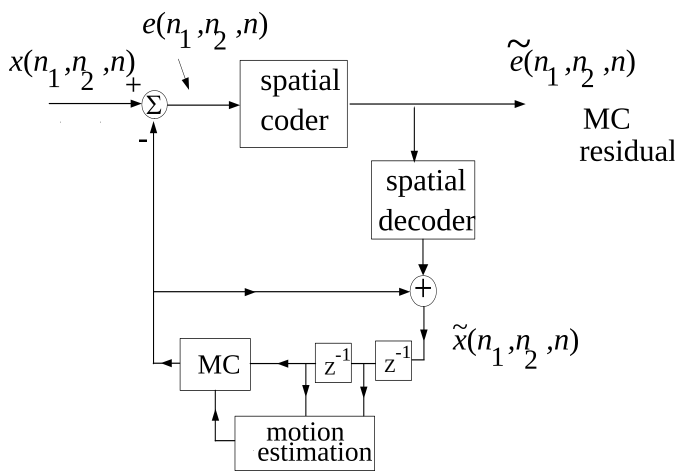

Figure 12.2–11. illustration of backward motion compensation

12.3 EARLY INTERFRAME CODING STANDARDS

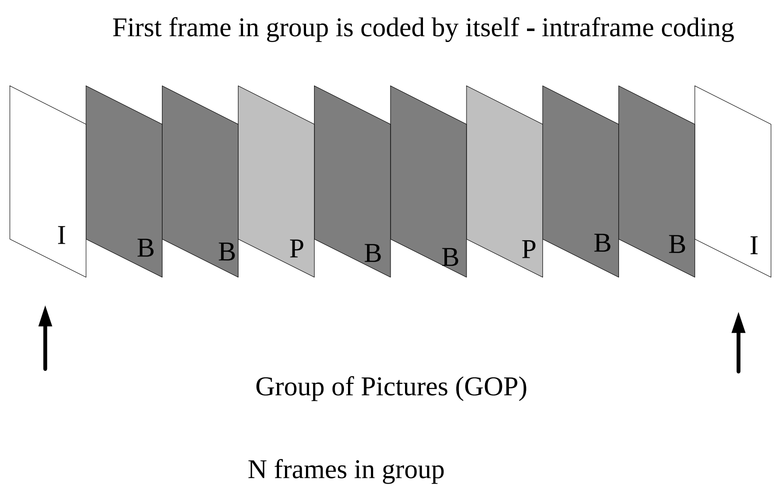

Figure 12.3–12. first code *I* frames.

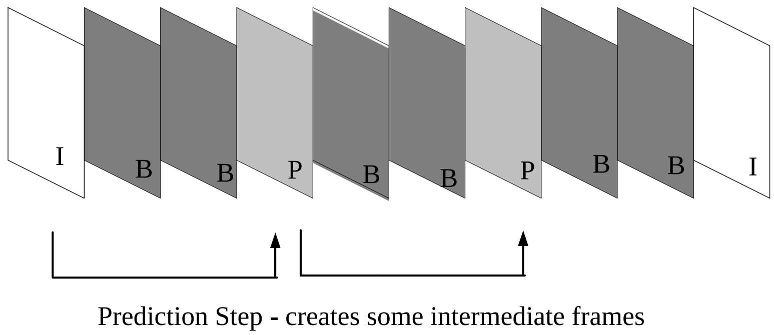

Figure 12.3–13. illustration of predictive coding of P frames in MPEG 1.

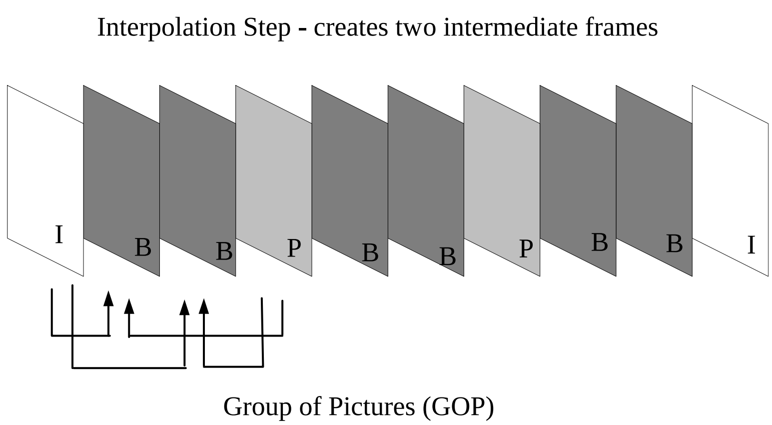

Figure 12.3–14. illustration of coding the B frames based on bi-directional references

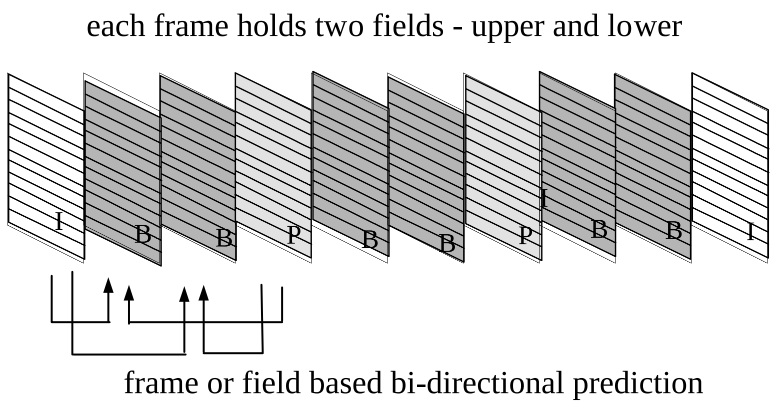

Figure 12.3–15. new in MPEG2 was the need to process interlaced frame data.

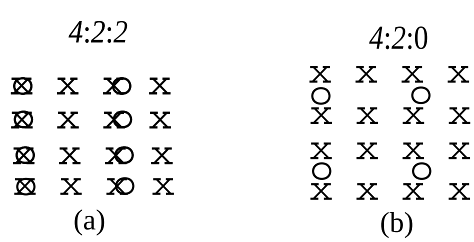

Figure 12.3–16. MPEG 2 4:2:2 and 4:2:0 luma and chroma subsampling sites.

12.4 INTERFRAME SWT CODERS

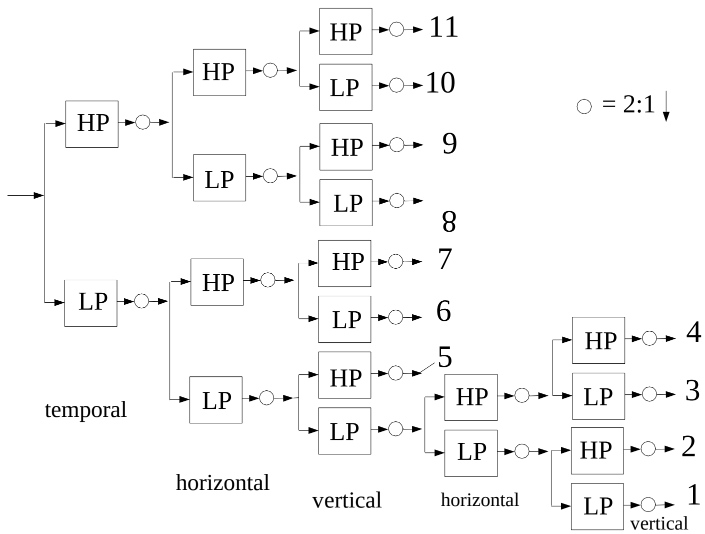

Figure 12.4–17. First 3-D subband filter due to Karlson

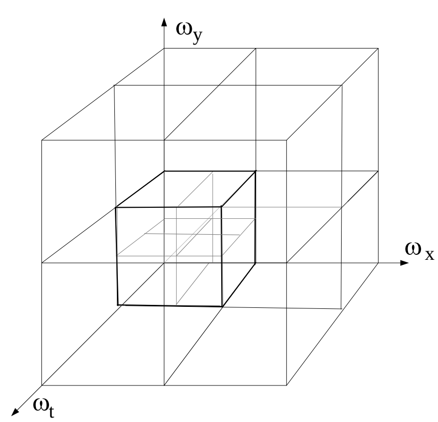

Figure 12.4–18. Frequency decomposition of Karlson's filter tree.

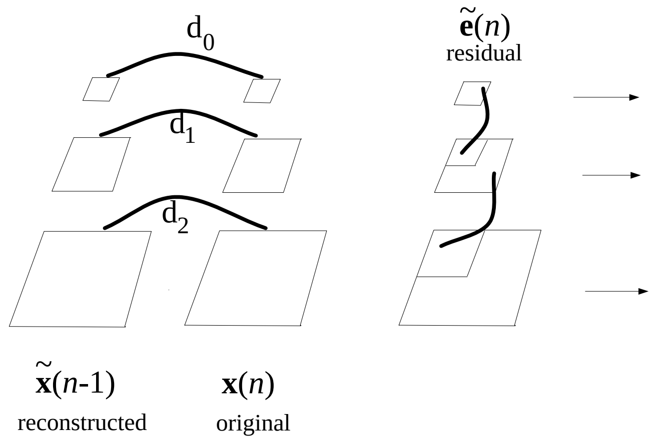

Figure 12.4–19. Illustration of Multiresolution coder

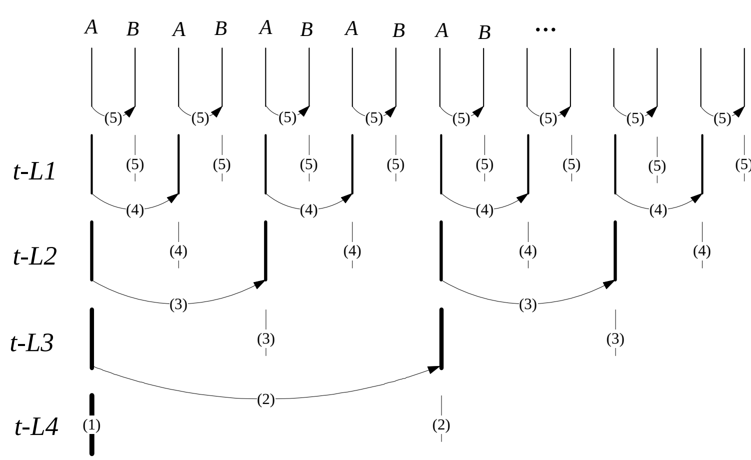

Figure 12.4–20. Illustration of four level Haar filter MCTF

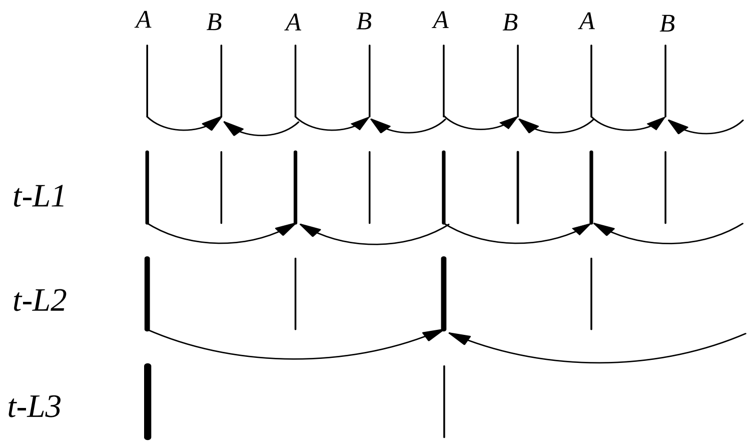

Figure 12.4–21. illustration of LGT 5/3 filter MCTF

12.5 SCALABLE VIDEO CODERS

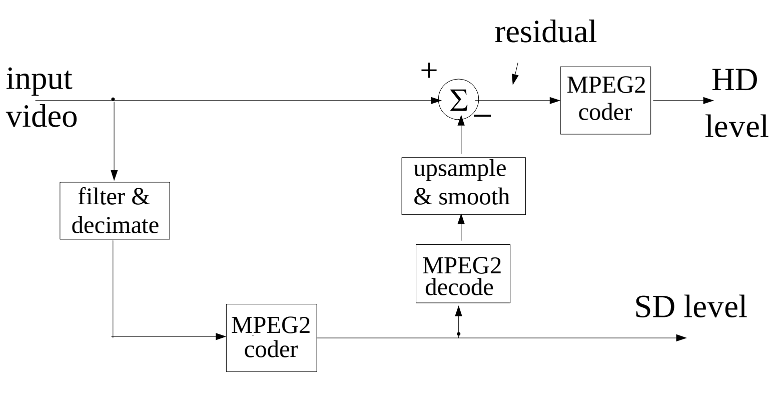

Figure 12.5–22. illustration of resolution scalability for SD and HD video using MPEG 2

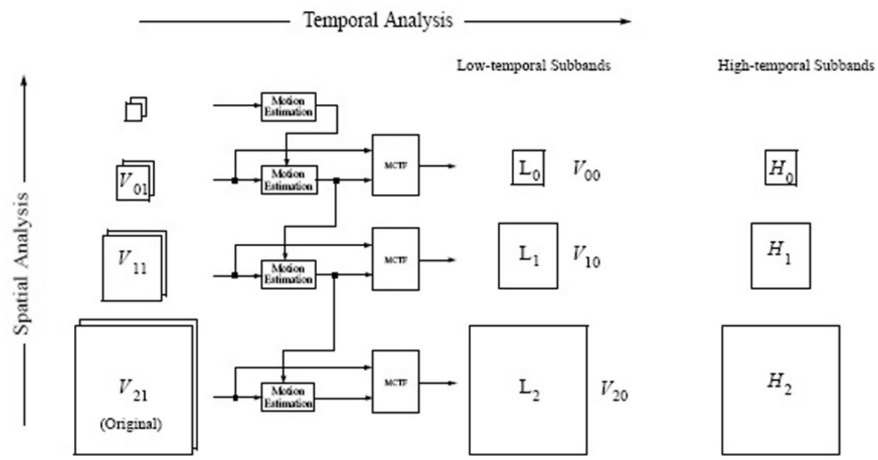

Figure 12.5–23. RSC demonstration software 3 resolutions, 2 frame rates © IEEE

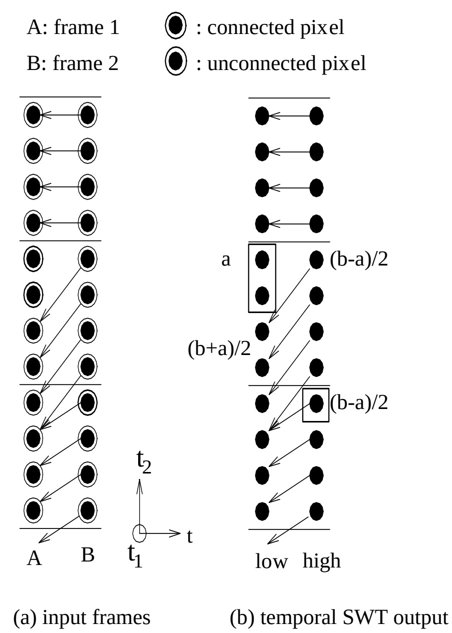

Figure 12.5–24. illustration of MCTF using Haar filters

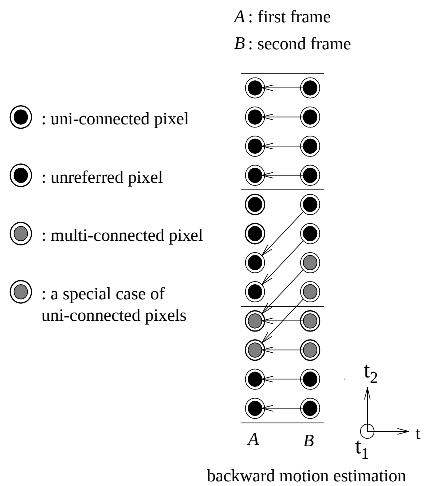

Figure 12.5–25.

Figure 12.5–26. Example of unconnected blocks detected in *FlowerGarden*.

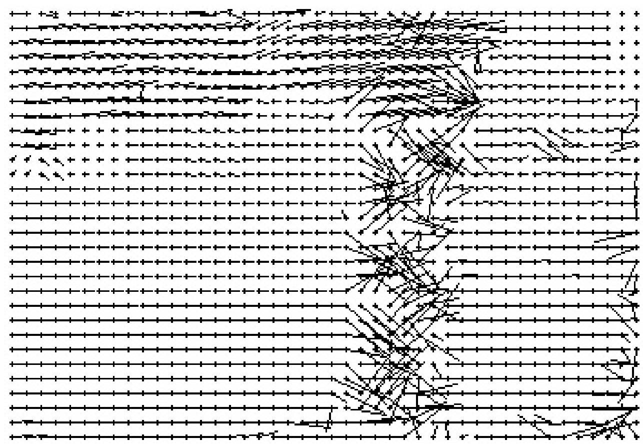

Figure 12.5–27. Example of motion field of unidirectional MCTF.

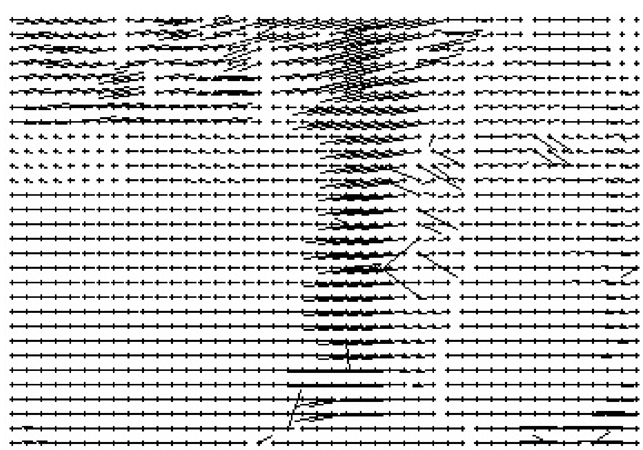

Figure 12.5–28. Example of motion field of bidirectional MCTF

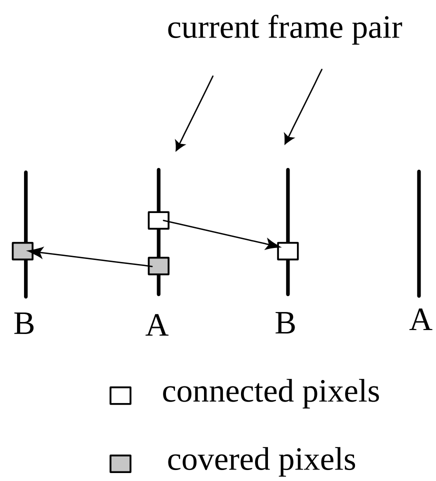

Figure 12.5–29. an illustration of bidirectional interpolation in the context of 2-tap Haar MCTF.

Figure 12.5–30. a frame output from unidirectional MCTF at four temporal levels down.

Figure 12.5–31. four temporal level down output of bidirectional MCTF.

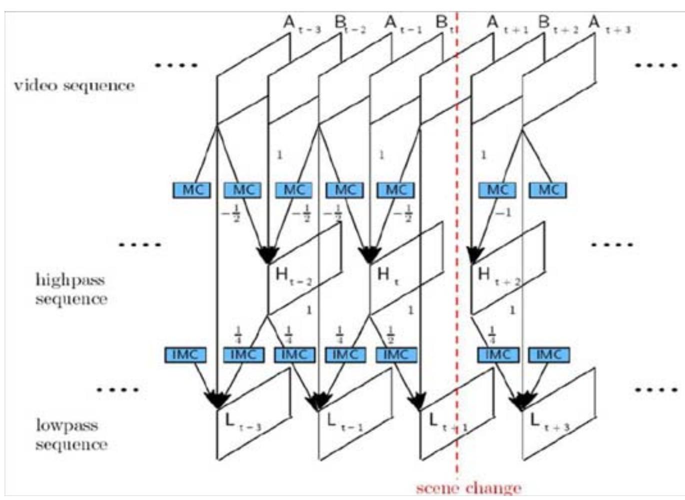

Figure 12.5–32. adaptive LGT/Haar MCTF (Fig. 1 from [**??**])

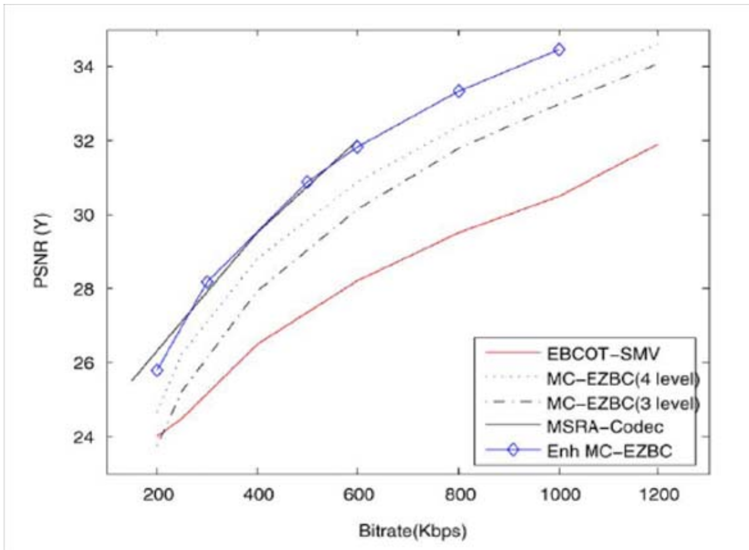

Figure 12.5–33. a coding comparison

12.6 CURRENT INTERFRAME CODING STANDARDS

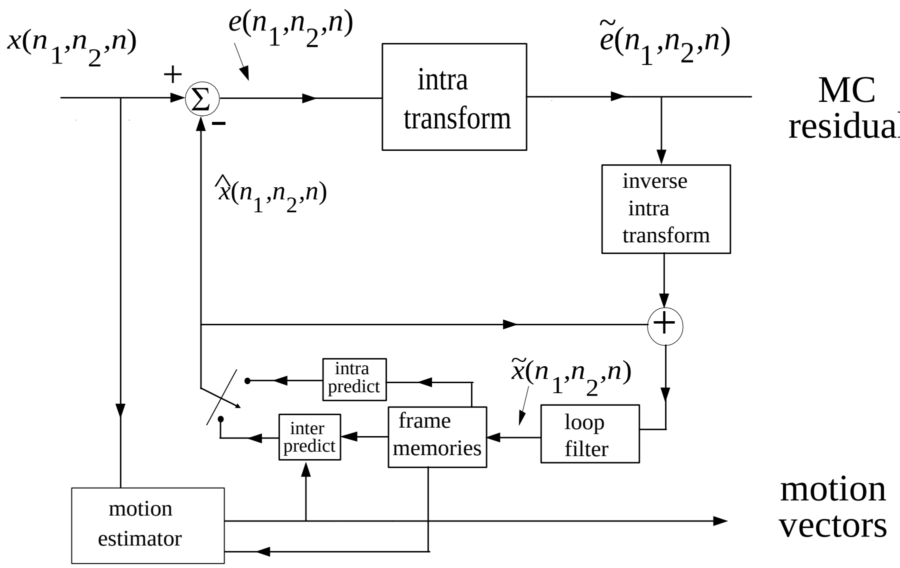

Figure 12.6–34. a system diagram of the H.264/AVC coder

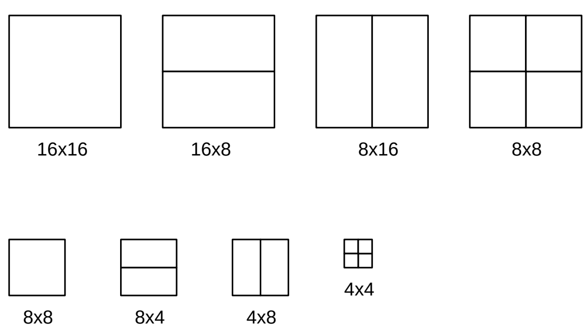

Figure 12.6–35. allowed MV block sizes in H.264/AVC.

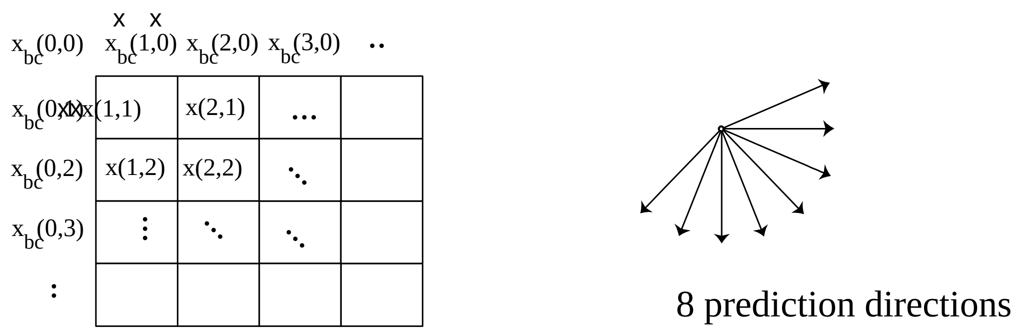

Figure 12.6–36. illustration of directional prediction modes of H.264/AVC in the case of 4 × 4 blocks.

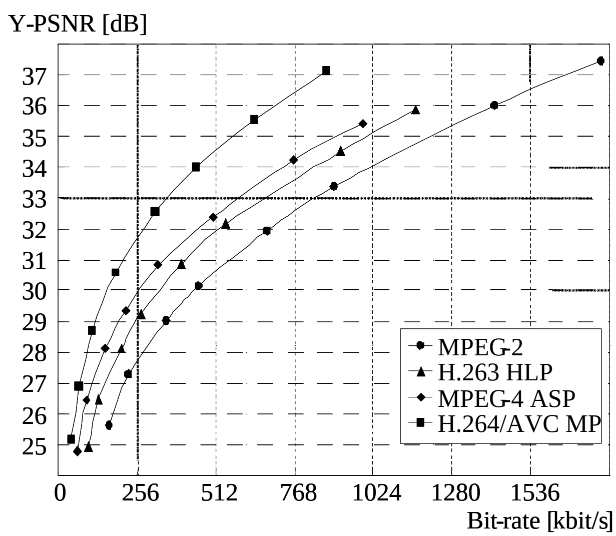

Figure 12.6–37. PSNR vs. bitrate for 15 fps CIF test clip *Tempete* (reprinted with permission) © IEEE

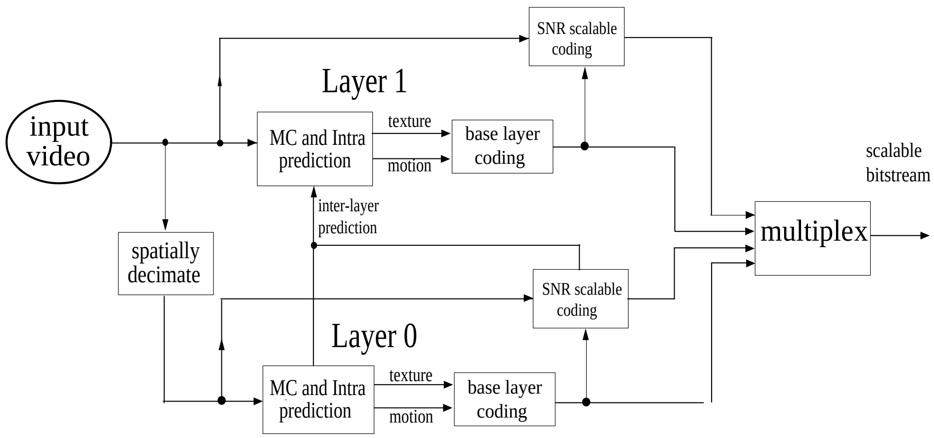

Figure 12.6–38. MPEG Scalable Video Coder

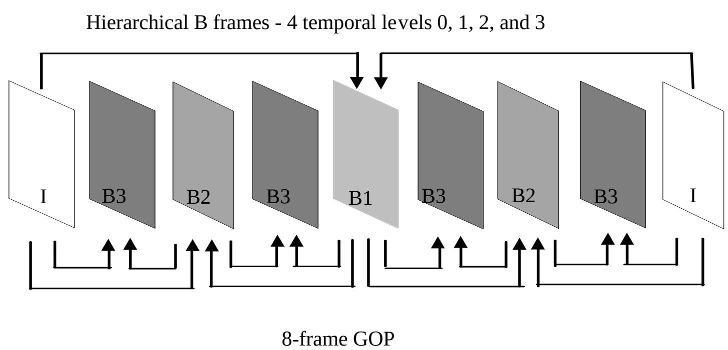

Figure 12.6–39. hierarchical B frame concept

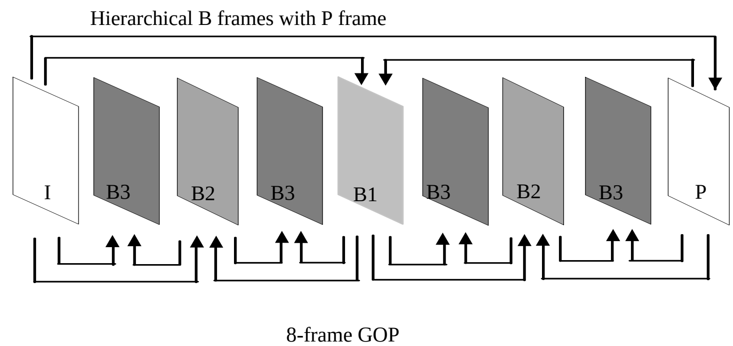

Figure 12.6–40. more efficient hierarchical B frame structure with GOP size 8

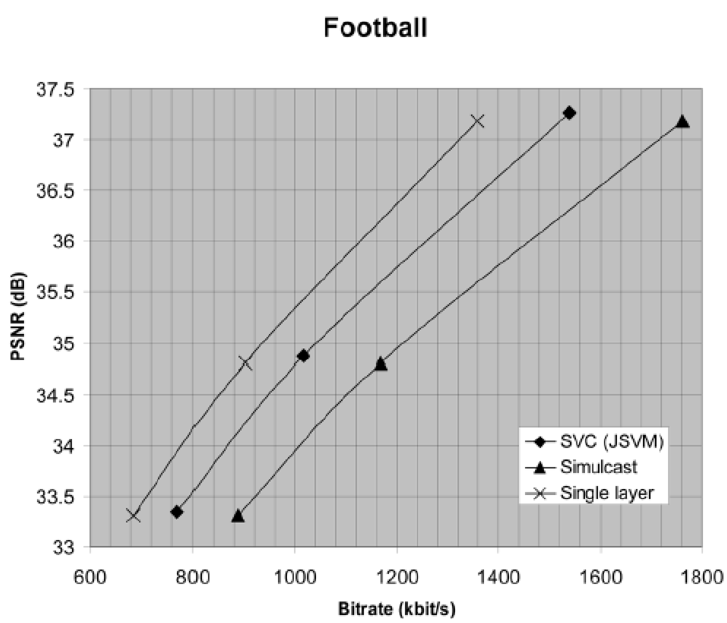

Figure 12.6–41. reproduced Fig. 6(b) from [**??**].

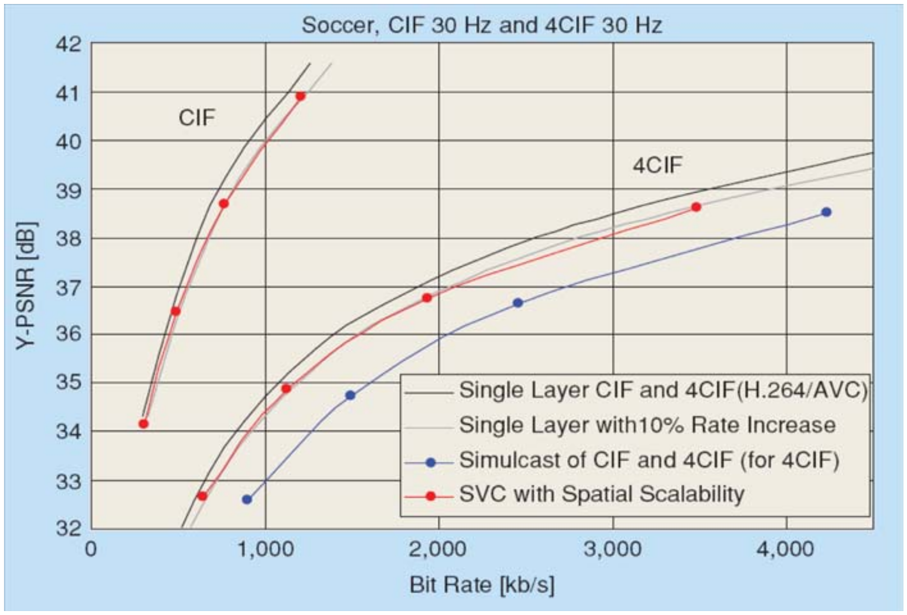

Figure 12.6–42. Illustration of H.264/SVC performance for spatiotemporal scalability - 4CIF@ 30 fps and CIF@15 fps. (from [**??**])

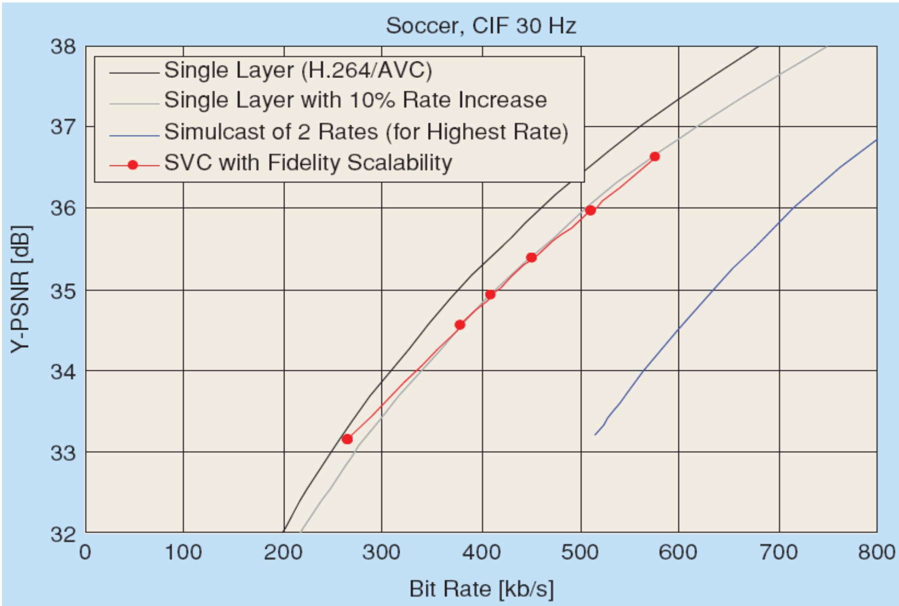

Figure 12.6–43. Illustration of quality scalability Soccer CIF@30 fps taken from [??]

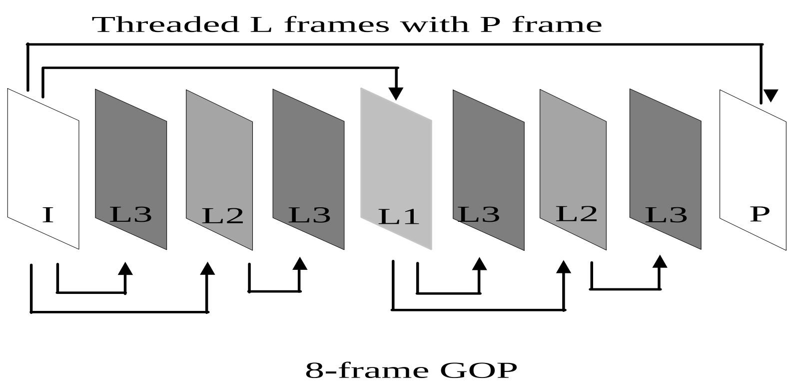

Figure 12.6–44. efficient threaded hierarchical structure without increased structural delay of B frames

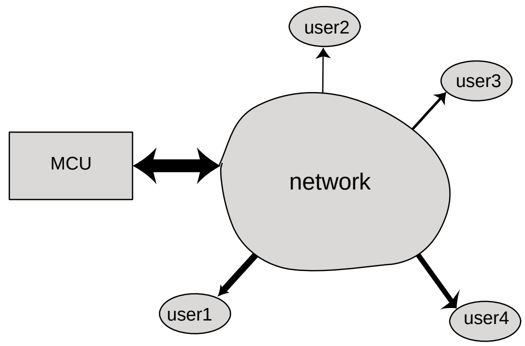

Figure 12.6–45. an illustration of conventional multipoint video conferencing architecture

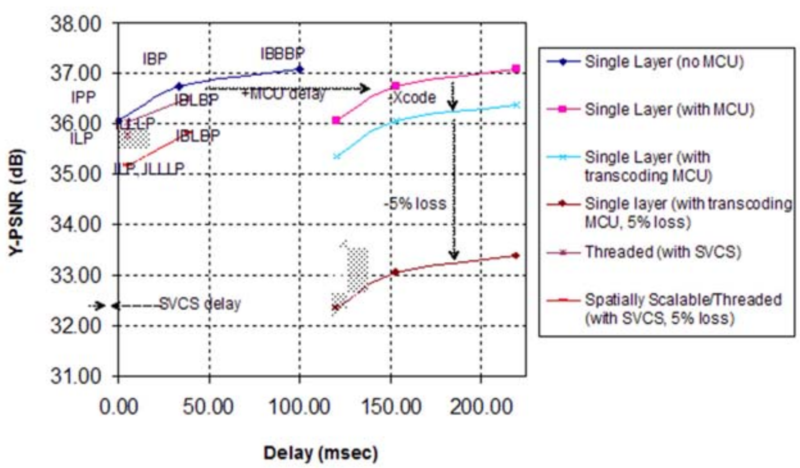

Figure 12.6–46. a simulated performance comparison of PSNR versus delay taken from [**??**] © JZUS A 2006

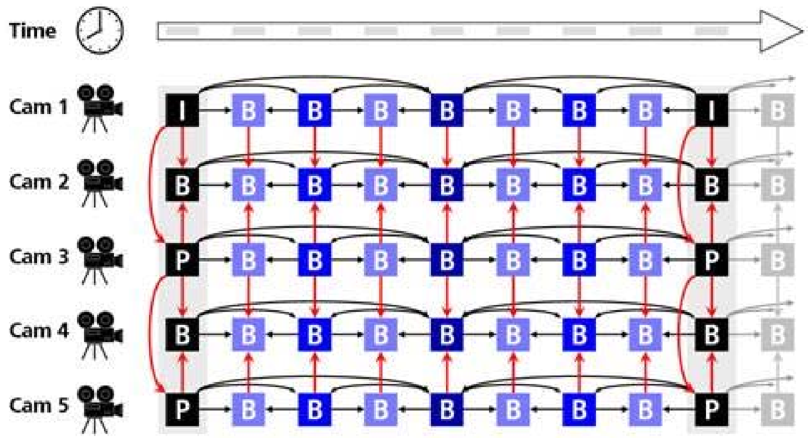

Figure 12.6–47. Illustration of H.264/MVC inter-view prediction hierarchy. (from public MPEG site [??])

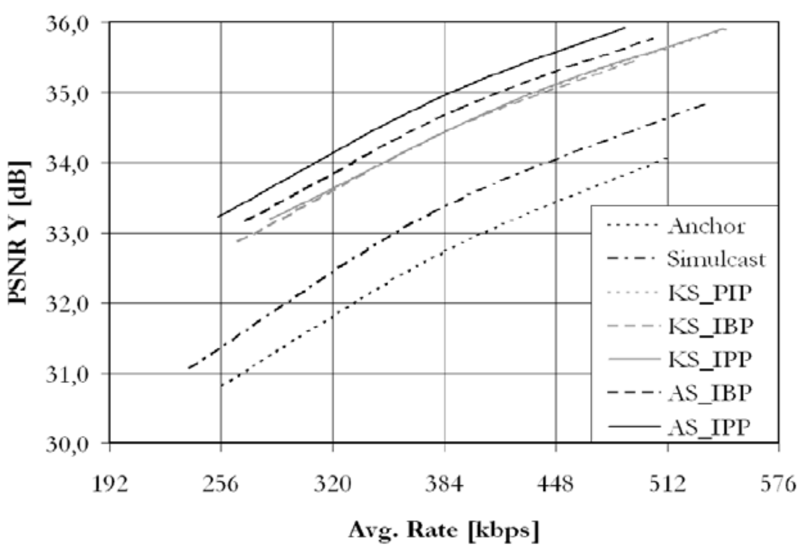

Figure 12.6–48. H.264/MVC result from Merkle et al 2007.

12.7 NONLOCAL INTRAPREDICTION

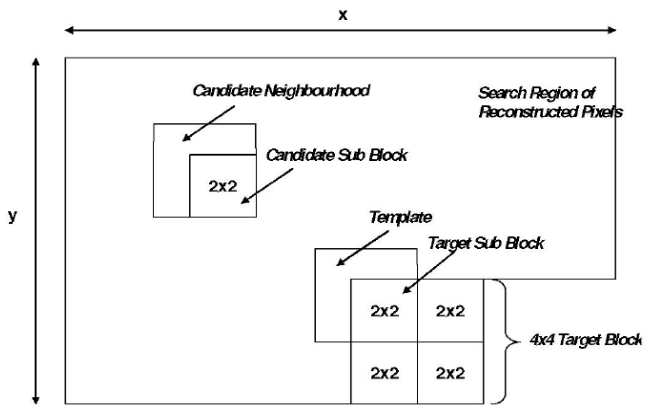

Figure 12.7–49. illustration of template matching for intra prediction from [TanBoonSuzuki]

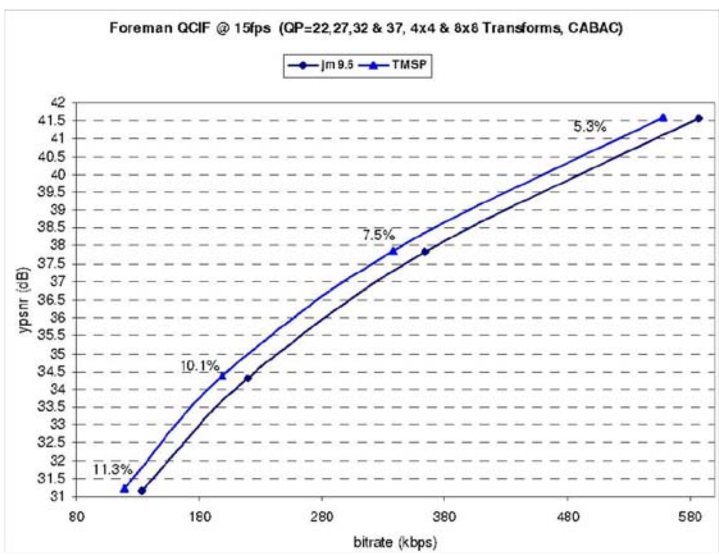

Figure 12.7–50. improvement in PSNR versus bitrate for Foreman QCIF @ 15 fps

12.8 OBJECT-BASED CODING

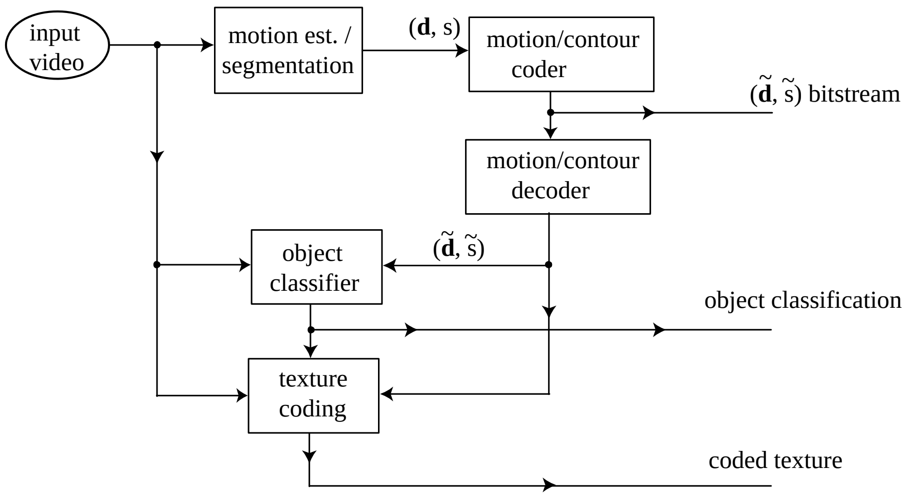

Figure 12.8–51. system diagram of the hybrid MCP object video coder in [**??**].

Figure 12.8–52. QCIF Carphone coded via object based SWT at 24 Kbps.

Figure 12.8–53. QCIF Carphone coded at 24 Kbps by H.263

12.9 COMMENTS ON THE SENSITIVITY OF COMPRESSED VIDEO

12.10 CONCLUSIONS

12.11 PROBLEMS

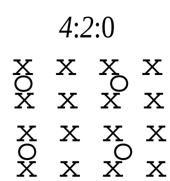

Figure 12.11–54. 4:2:0 color space structure of MPEG-2

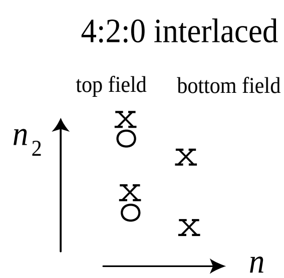

Figure 12.11–55. 4:2:0 chrominace samples are part of top field only.

Chapter 13

Video Transmission over Networks

13.1 VIDEO ON IP NETWORKS

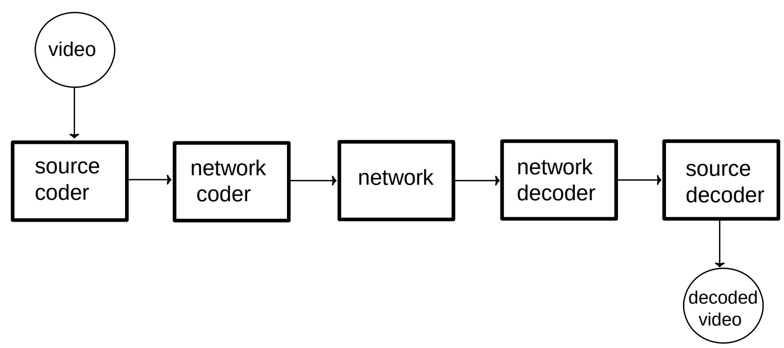

Figure 13.1–1. system diagram of networked video transmission

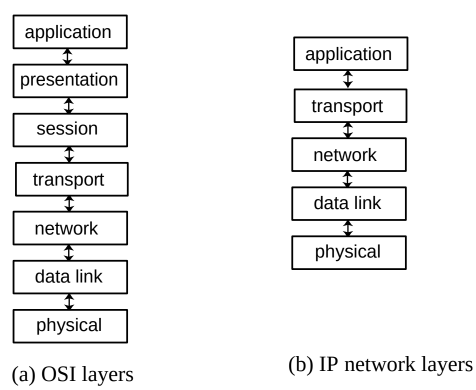

Figure 13.1–2. network reference models (stack)

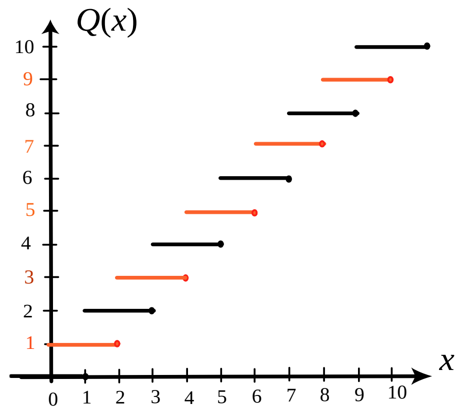

Figure 13.1–3. illustration of an MDC scalar quantizer.

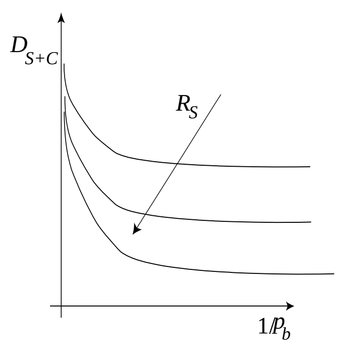

Figure 13.1–4. Total distortion plotted versus reciprocal of channel bit error probability, with source coding rate as a parameter.

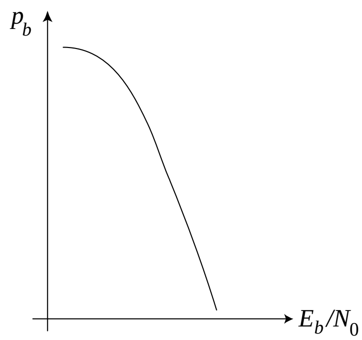

Figure 13.1–5. probability of bit error versus channel signal to noise ratio.

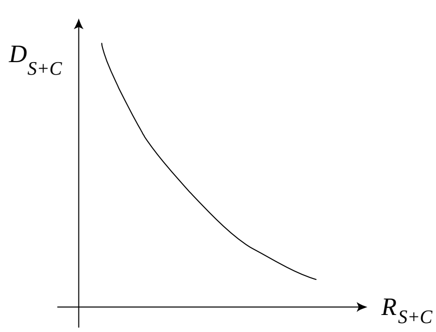

Figure 13.1–6. total distortion versus source bits per channel use

13.2 ROBUST SWT VIDEO CODING (Bajic)

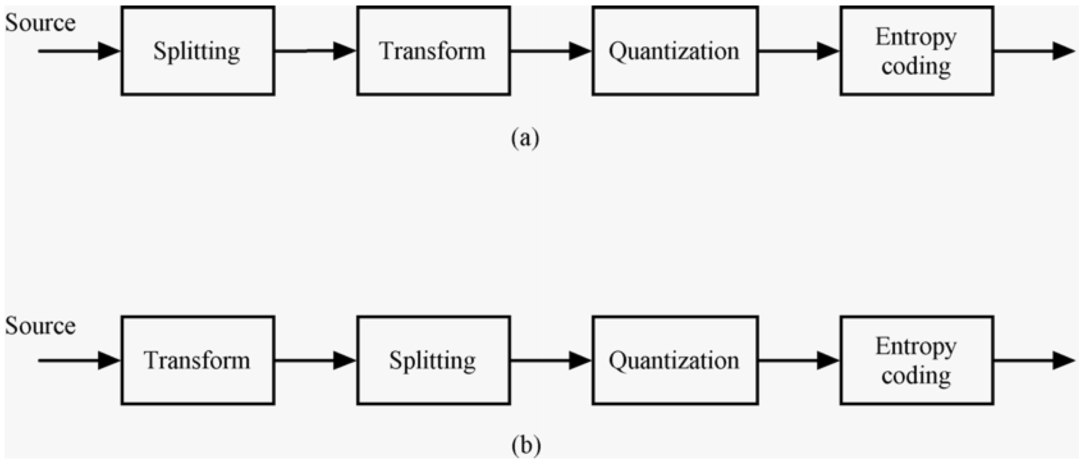

Figure 13.2–7. Splitting of source samples can be done (a) before the transform, or (b) after the transform.

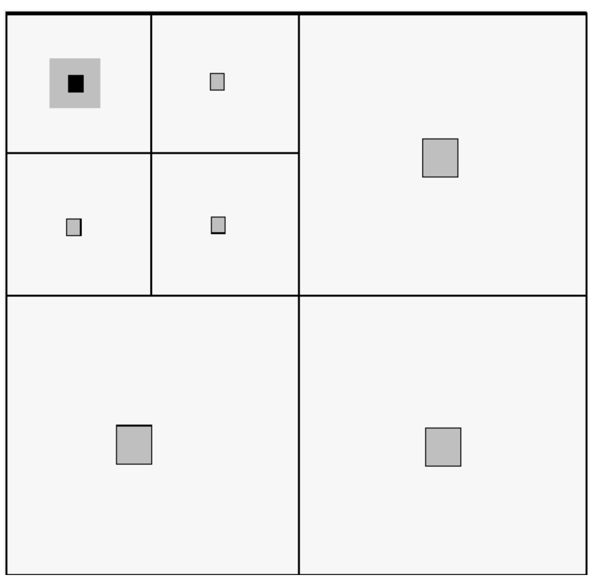

Figure 13.2–8. One low frequency SWT sample (black) and its space-frequency neighborhood (gray).

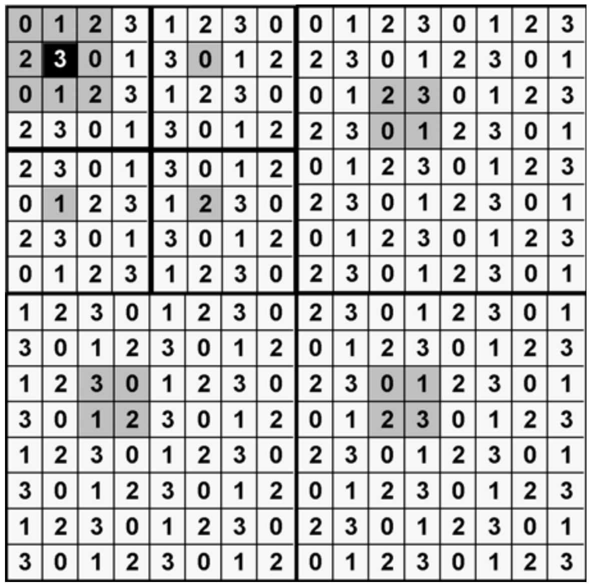

Figure 13.2–9. Example of a 16×16 image with two levels of SWT decomposition, packetized into 4 packets.

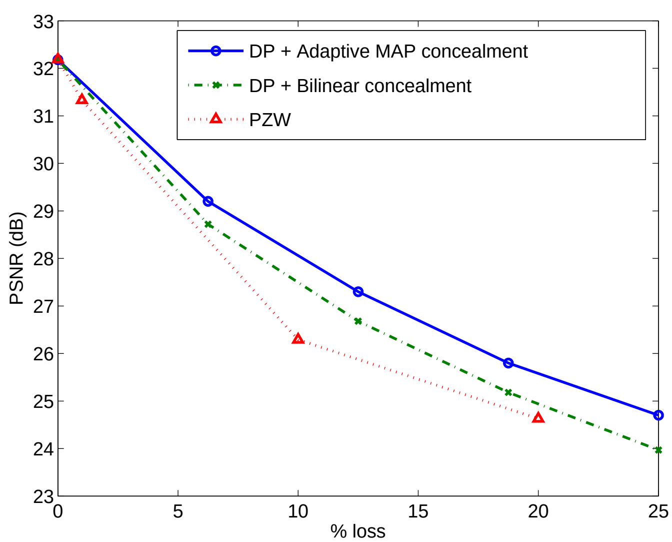

Figure 13.2–10. PSNR versus packet loss on *Lena*.

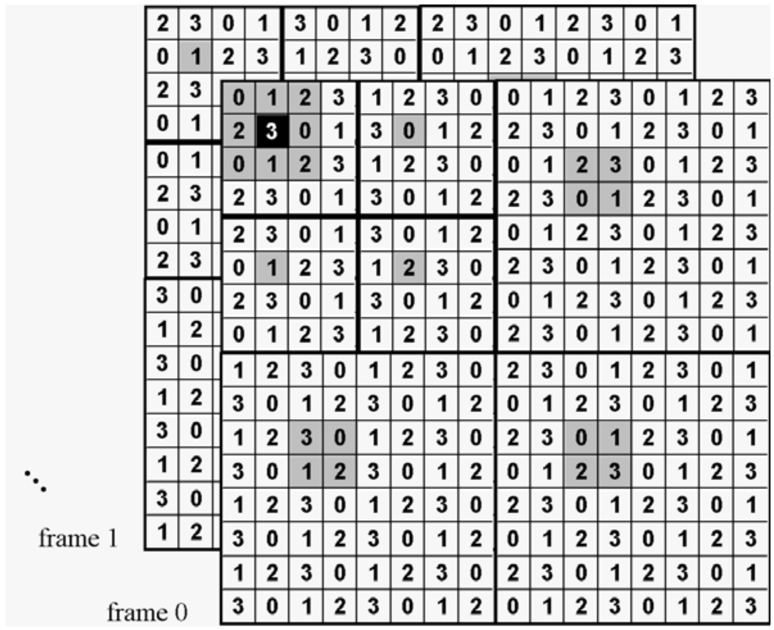

Figure 13.2–11. Extension of dispersive packetization to three dimensions.

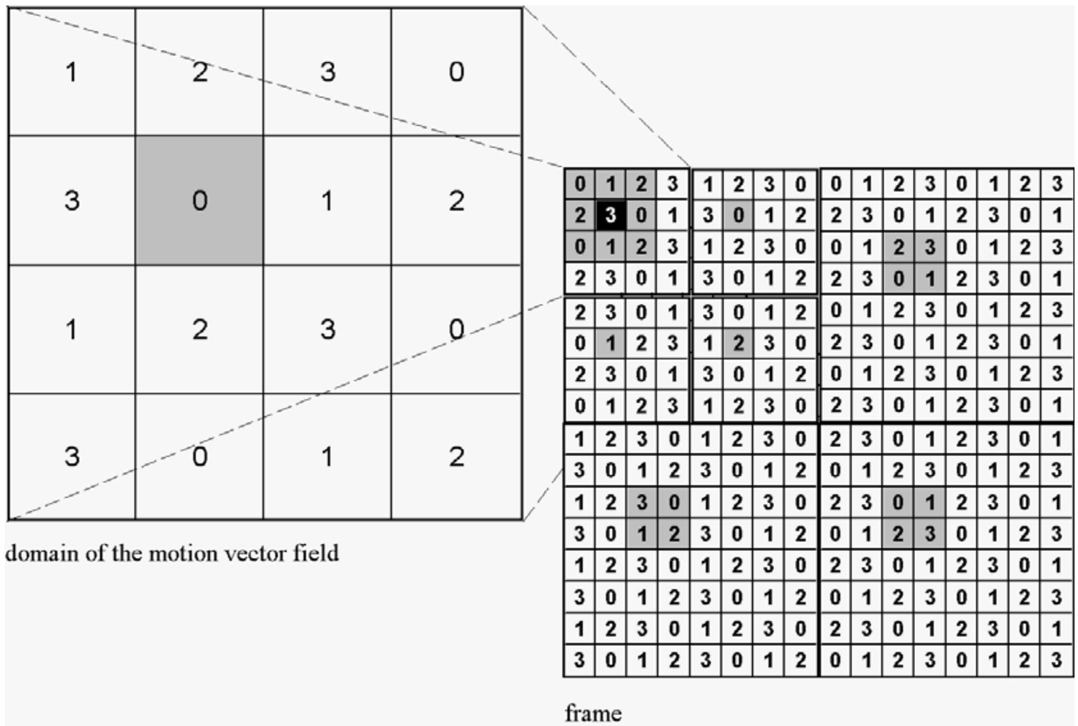

Figure 13.2–12. Dispersive packetization of motion-compensated SWT video.

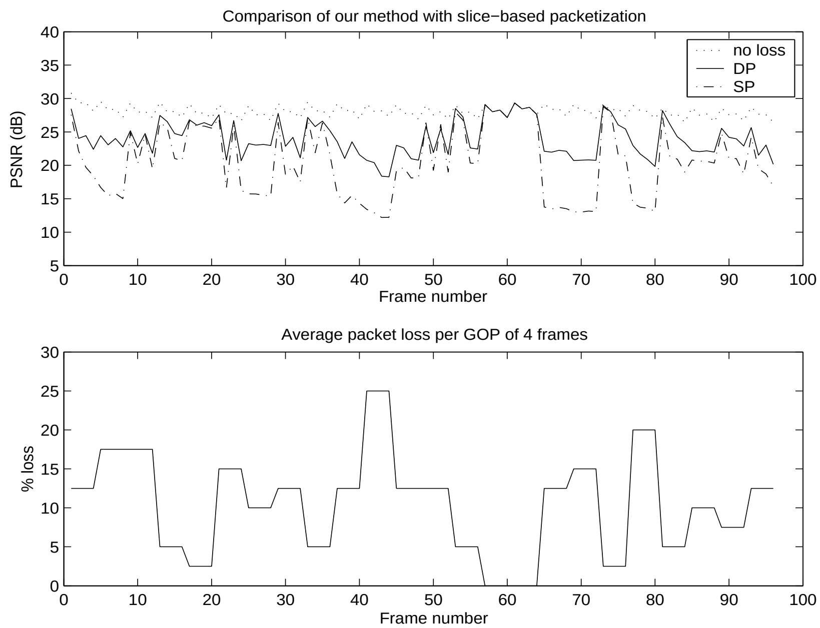

Figure 13.2–13. Comparitive performance of DP and SP schemes on *Football*.

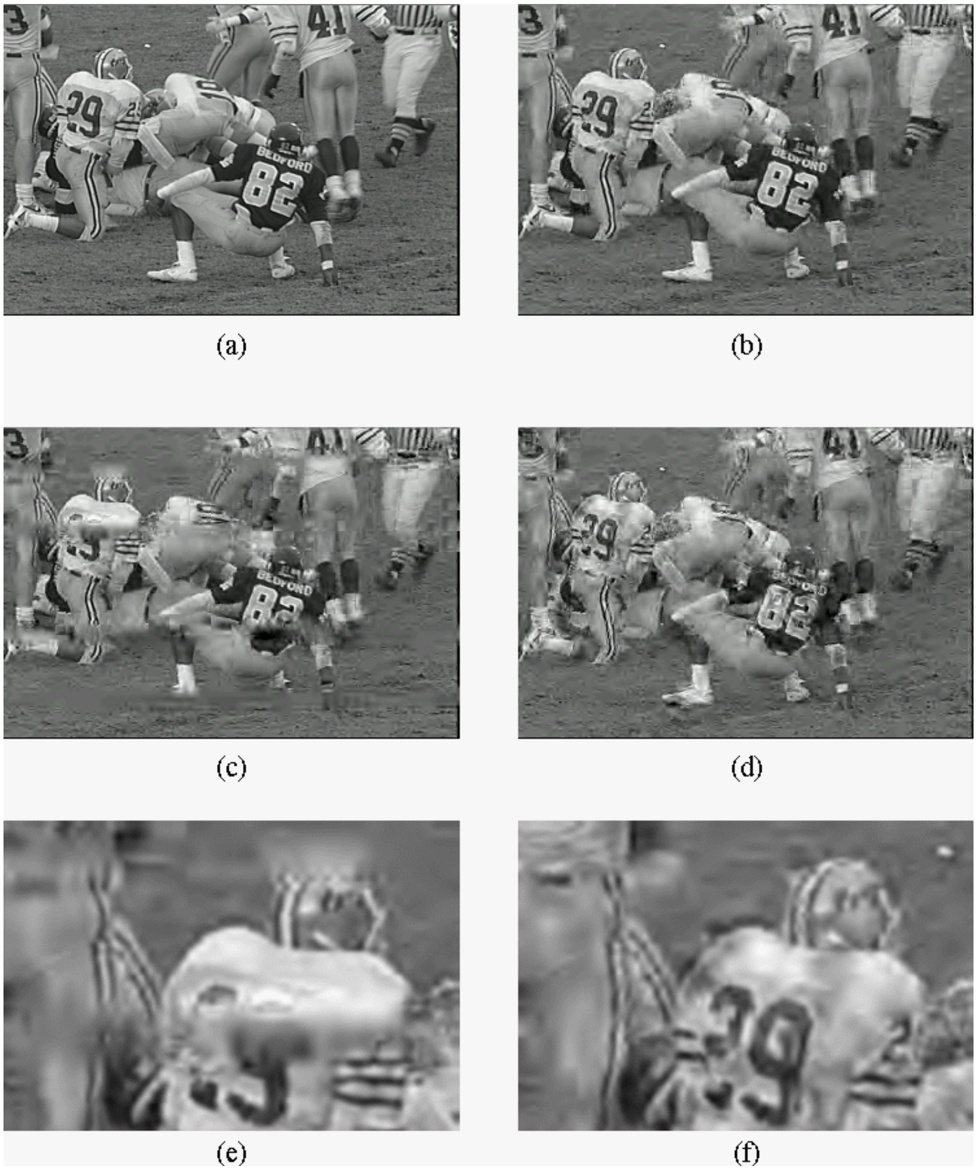

Figure 13.2–14. DP demonstration: frame 87 of the *Football* sequence, SIF at 1.34 Mbps.

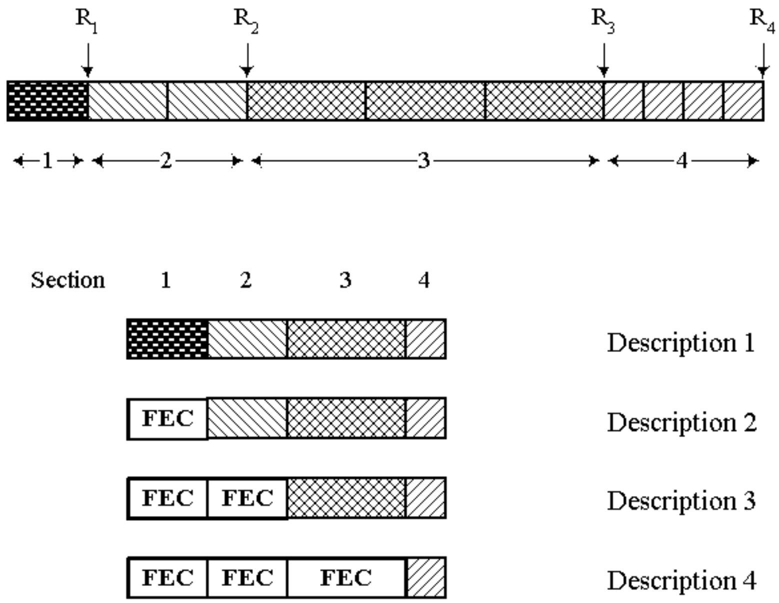

Figure 13.2–15. A simple illustration of MD-FEC.

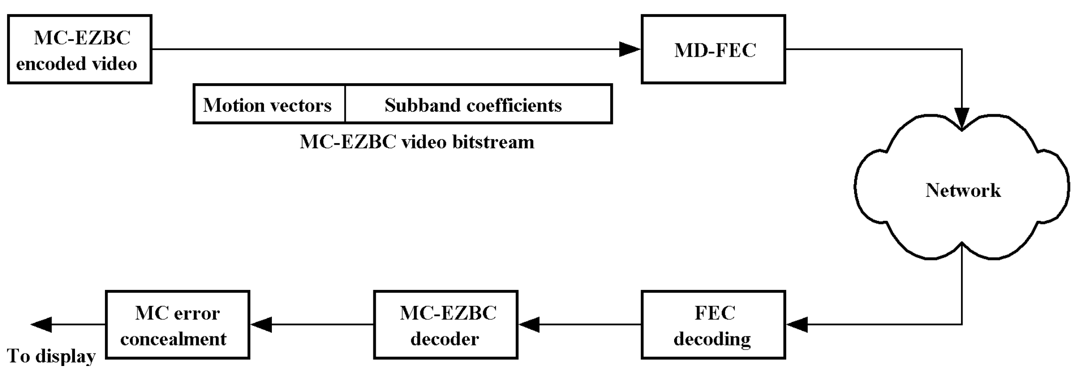

Figure 13.2–16. Video streaming system based on MC-EZBC.

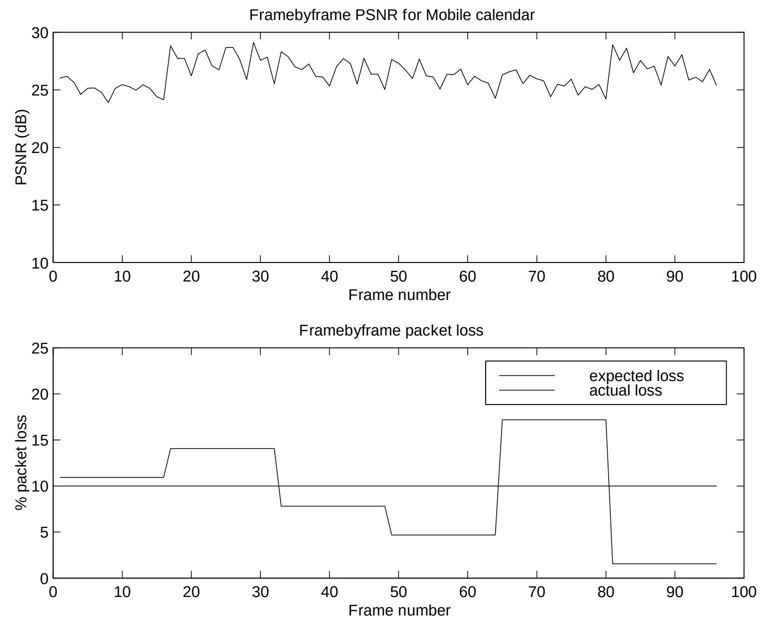

Figure 13.2–17. MD-FEC simulation result on *Mobile calendar* clip

13.3 ERROR-RESILIENCE FEATURES OF H.264/AVC

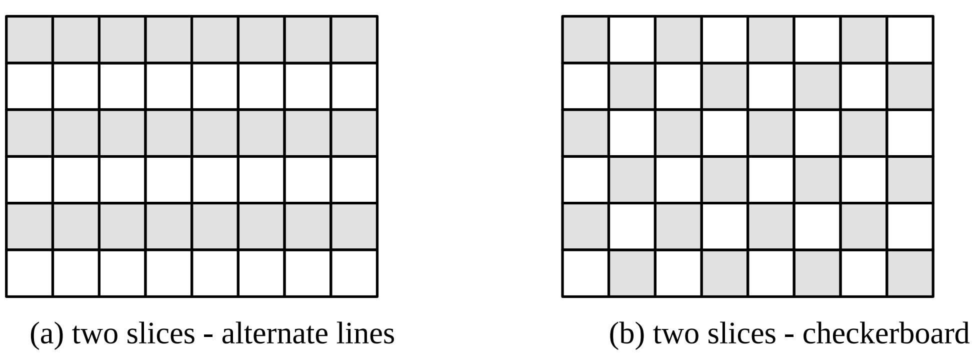

Figure 13.3–18. an interleaved and FMO mapping of macroblocks onto two slices: the gray and the white slice

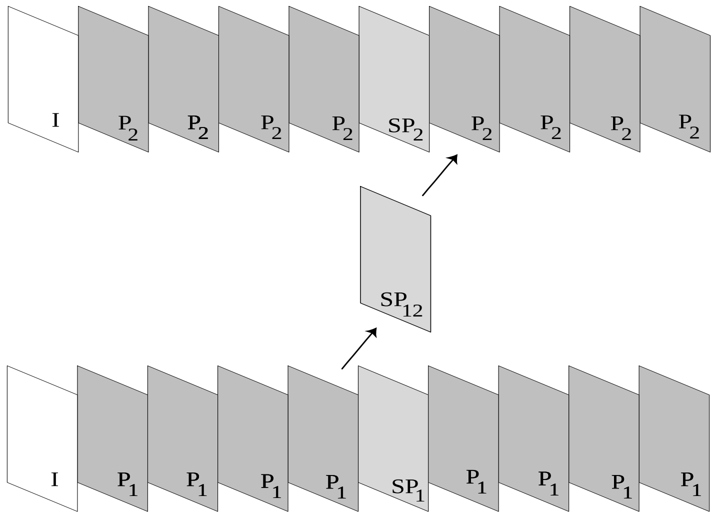

Figure 13.3–19. illustration of switching from bottom bitstream 1 to top bitstream 2 via switching frame SP_{12}.

Figure 13.3–20. a slice consists of one row of macroblocks

Figure 13.3–21. a slice consists of three contiguous rows of macroblocks.

13.4 JOINT SOURCE-NETWORK CODING

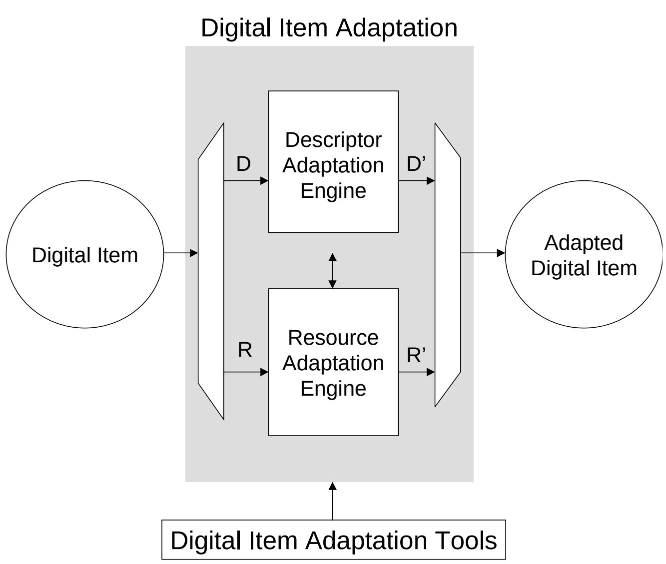

Figure 13.4–22. a concept DIA model from [**??**].

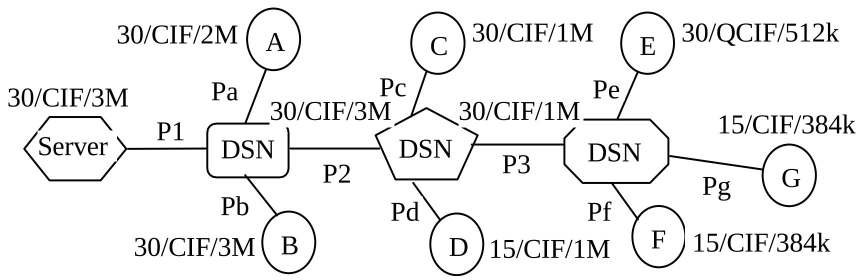

Figure 13.4–23. an example overlay network

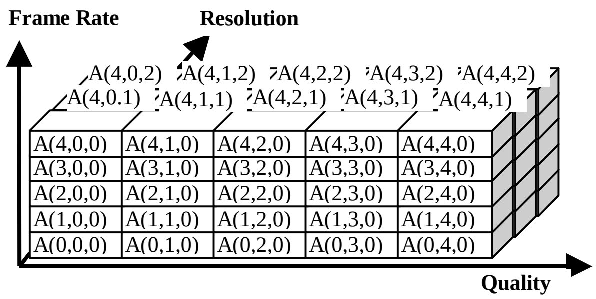

Figure 13.4–24. atom diagram of video scalability dimensions (from [**??**]).

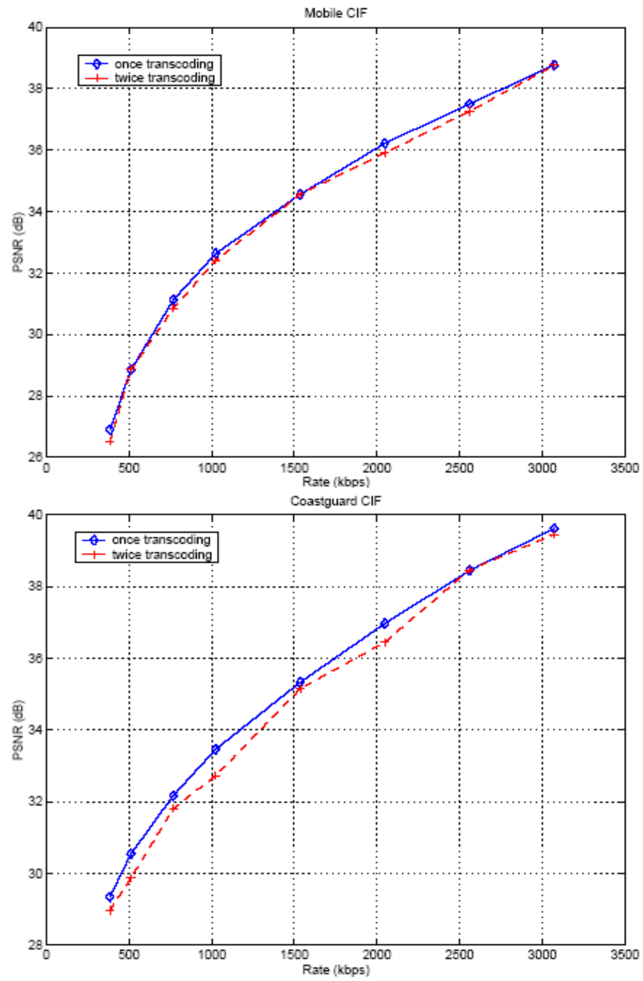

Figure 13.4–25. PSNR performance comparison (*Mobil* and *Coastguard* in CIF format) versus bitrate for DIA operation in network.

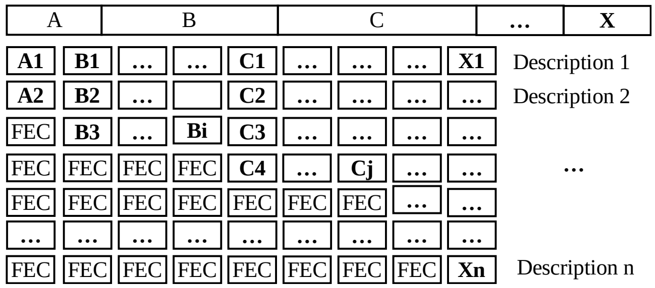

Figure 13.4–26. FGA-FEC coding scheme

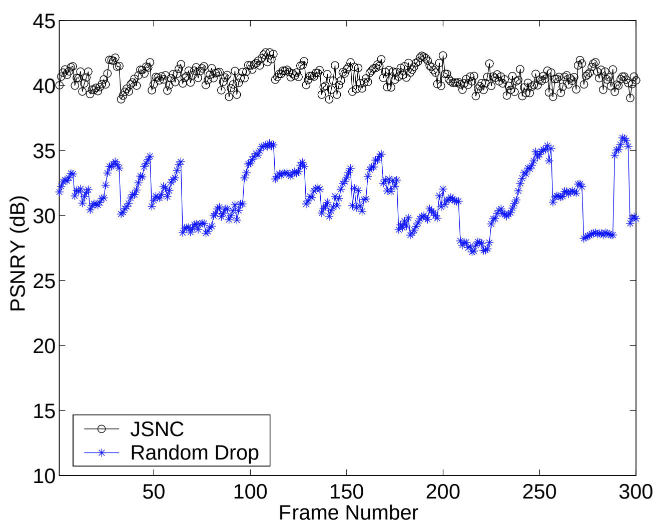

Figure 13.4–27. JSNC versus random packet drop.

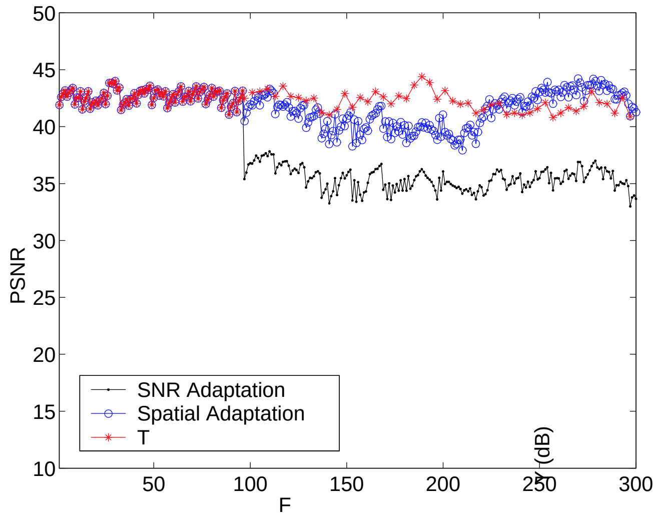

Figure 13.4–28. 3-D adaptation in frame rate, resolution, and SNR (bitrate)

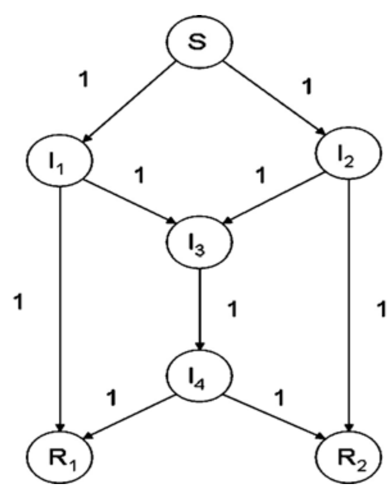

Figure 13.4–29. simple directed graph network *butterfly*

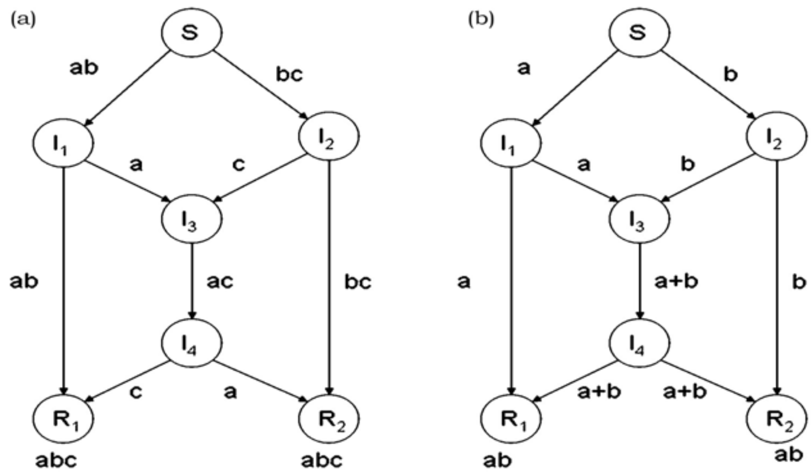

Figure 13.4–30. Butterfly net: (a) **routing** - showing two uses of each link and with replication, (b) **network coding** - showing one use of each link.

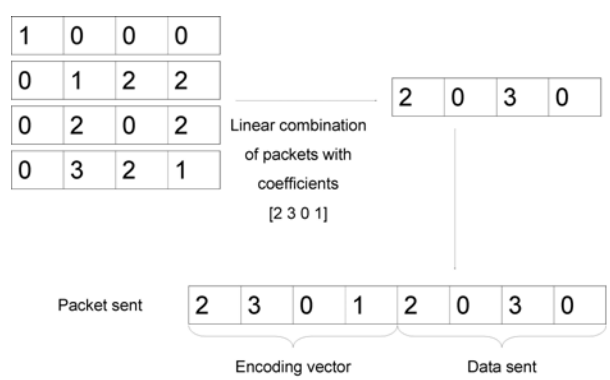

Figure 13.4–31. PNC computations at source

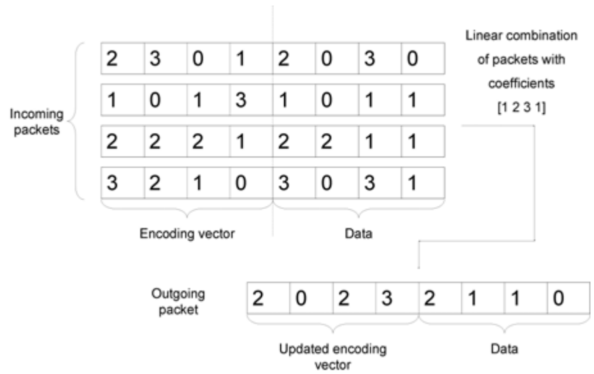

Figure 13.4–32. PNC computation at intermediate node.

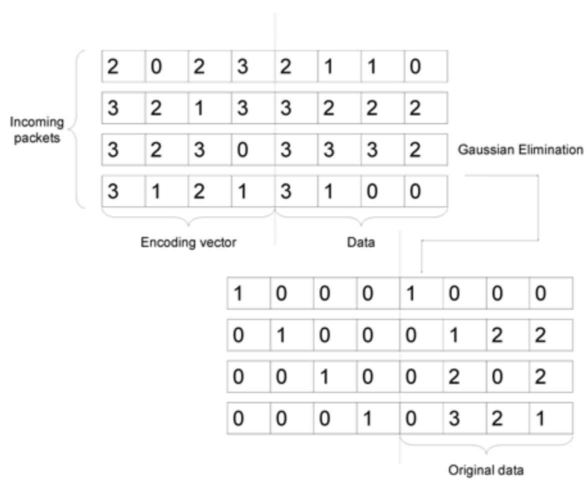

Figure 13.4–33. PND decoding at reciver using Gaussian elimination.

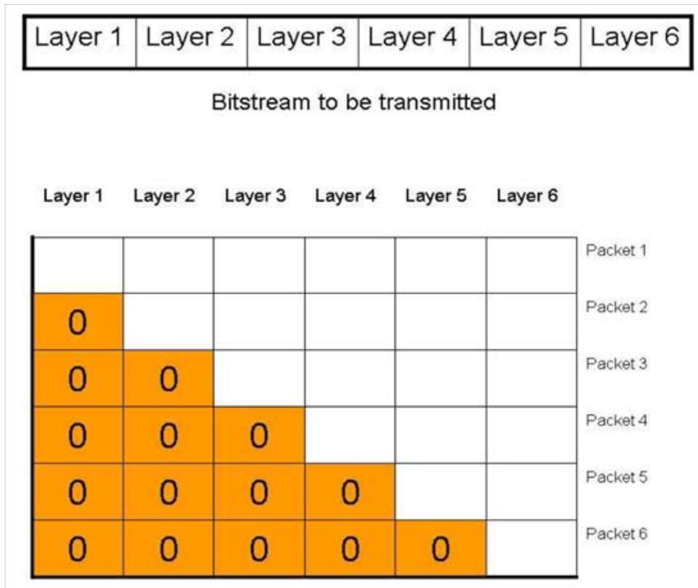

Figure 13.4–34. simple illustration of MD-PNC concept

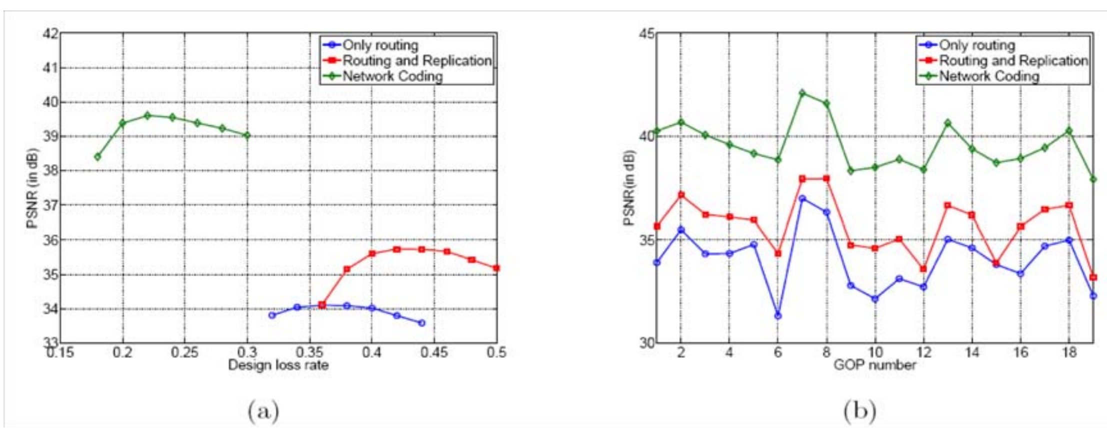

Figure 13.4–35. *Foreman* clip PSNRs with link-loss rate of 20%. (a) variation of PSNR versus design loss rate, (b) PSNR versus frame number at best design loss rate.

13.5 CONCLUSIONS

13.6 PROBLEMS

+	0	1	2	3
0	0	1	2	3
1	1	0	3	2
2	2	3	0	1
3	3	2	1	0

x	0	1	2	3
0	0	0	0	0
1	0	1	2	3
2	0	2	3	1
3	0	3	1	2

Galois Field arithmetic table.

Figure 13.6–36. arithmetic tables for $GF(2^2)$